On the interaction between wheels and rails in railway dynamics

Slivsgaard, Eva Charlotte

Publication date:
1995

Document Version
Publisher's PDF, also known as Version of record

ON THE INTERACTION BETWEEN WHEELS AND RAILS IN RAILWAY DYNAMICS

Eva Charlotte Slivsgaard

LYNGBY 1995
IMM-PHD 1995-20
ATV Erhvervsforskerprojekt EF 0461

IMM DSB

ISSN 0909-3192

Trykt af IMM - DTU
Bogbinder Hans Meyer

Preface

The present thesis is a part of the acquisition of my Ph.D-title. The work has been carried out in the period from first of February 1993 to the first of August 1995 as a co-operation between the consulting department in the Danish State Railways, DSB Consult and the Institut of Mathematical Modelling at the Technical University of Denmark. The work is supported by the Danish Academy of Technical Sciences.

I am indebted to Preben Olesen, Chief Engineer in DSB Consult, Helge Erlandsen, former Sector Chief in DSB Consult and Hans True at the Technical University of Denmark for making it possible to make this thesis.

A further thank to my supervisor Hans True for his support, interest and inspiration through out the years. It is also due to Hans that I today have many international contacts in the field of nonlinear dynamics and vehicle system dynamics.

A great thank to my research colleaque Jens Christian Jensen for valuable and interesting discussions. To be able to discuss problems and new ideas have been very fruitful.

I will like to thank the measuring group in DSB Consult, especially Jørgen Tornhøj Christensen for welcoming me in DSB. Tornhøj and his group, including my research colleagues Jacob Egede Andesen and Jens Christian Jensen has been the base for a fruitful technical enviroment. The measurements describe in this thesis are the work of the measuring group and I owe Tornhøj and his men another thank for valuable discussions in interprediction of the results from the measurements.

The last months I have been connected with the office Track Work in DSB Consult. I thank my colleagues here for a warm welcome.

From project new S-train I am grateful to Per Jung for being interested in my work. I have had many interesting discussions of the construction of the new S-train with Per. Further more I thank Per for indispensable help during the

measurements of the running behaviour of the test vehicle.

My project has been guided by a group consisting of: Preben Olesen, Niels Fisher-Nielsen, Jørgen Jessen, Finn Wedendahl, Jørgen Tornhøj Christensen, Hans True, Eilif Svensson, Rosemarie Boeck and Sten Melson. I thank all in this group for their support and involvement.

During my work I have stayed at foreign research departments. These stays have been of great inspiration. A special thank to Bridget Eickhoff and Graham Scott, BR Research, Jean Pierre Pascal, INRETS, and José Germán Giménez and Luis Manuel Martin Nieto, CAF for their time and explanations during my stays.

In connection with the thesis I thank Hugh Campbell for correcting my english.

Also a thank to all my collegues in DSB for making the work fun.

Finally I thank Claus Rindom for help, patience, support and understanding through out the years.

Copenhagen, August 1995

Eva Charlotte Slivsgaard

Eva Charlotte Slivsgaard

Summary

The present thesis is concerned with the mathematical modelling of a railway vehicle. The modelling does not only deal with the vehicle but also the track it runs on. Different models are described and investigated as to how they affect the dynamics of the vehicle.

The bulk of the investigations is focussed on the stability of the vehicle. For this we introduce two stability criteria: *the linear critical speed* and *the nonlinear critical speed.* The linear critical speed is the vehicle speed at which the vehicle becomes unstable in a linear analysis, while the nonlinear critical speed is such that no oscillating solutions occur below this vehicle speed. The difference between a linear and a nonlinear analysis is hereby pointed out.

The oscillating solutions found are analysed by applying methods from the nonlinear dynamics. By this periodic and chaotic solutions are described, for instance a scenario of a period adding sequence.

For the vehicle we use a two-car test vehicle with a prototype of a single-axle bogie (a so-called KERF bogie). The vehicle is from the Danish State Railways and runs on the Copenhagen network. What is special about this vehicle is that the single-axle bogie is steered by a mechanical steering system. Interest is focussed on the single-axle bogie.

For simplification a model of the single-axle bogie alone is analysed under different modelling conditions. The dynamics of a model of the whole vehicle are investigated on

- a straight track
- a curved track
- a track flexible in the vertical direction
- a track with irregularities

Among other things, the investigations lead to the understanding of the influence of the stiffness in the steering system. On the irregular track the

simulations are compared with corresponding measurements.

Furthermore two different models are developed for the track:

- A simple model of the whole track as one rigid body following each wheelset.

- An elastic model where the rails are modelled as Euler-Bernoulli beams discretely supported by rigid sleepers.

The simple model is used to find the influence of a flexible track on the dynamics of the single-axle bogie, while the elastic model is more useful to for example study the effect of changes in flexibility along the track.

Finally measurements of the flexibility of tracks are described.

Table of contents

Chapter 1

Introduction

In recent decades there has been a growing interest in new railway vehicle designs and consequently a desire for a better understanding of the dynamic behaviour of a railway vehicle. Especially the development of high speed trains has led to studies of railway vehicle dynamics throughout the world.

Among other things, the studies have dealt with the mathematical modelling of a railway vehicle and have resulted in the development of computer programs for the simulation of the dynamics of railway vehicles. As examples, we can mention VAMPIRE from BR Research in Derby, VOCODYM from INRETS in Paris, MEDYNA from DLR in Munich and SIDIVE from CAF in Spain. Also in Denmark, where Hans True has been the main initiator, focus on modelling railway vehicles has been engendered. This has led for instance to a Ph.D thesis by Jens Christian Jensen, [Jensen, 1995] as well as to the present thesis.

One of the main applications of mathematical modelling is to define the running behaviour of a vehicle. When designing and operating a railway vehicle some questions arise: When is the vehicle running stably? When is the running behaviour good? How does the vehicle and track interact, and which parameters influence the stability and the dynamics?. Mathematical modelling can help us to answer these questions.

In the analysis of the running behaviour of a vehicle it is not sufficient to consider only the vehicle; also the track must be taken into account. The problem to be solved is to determine the effects of the interaction between the running gear and the track, and both elements need to be considered when studying the performance. In this thesis we will analyse the flexibility of the track and its effect on the vehicle.

1.1 The conflict between straight track and curves

To illustrate the fundamental behaviour of a railway wheelset, let us consider a free wheelset with conical wheels. Futhermore let us assume that there are no friction forces between wheels and rails. On a straight track a lateral disturbance of the wheelset will have the result that the rolling radius and consequently the longitudinal velocity of one of the wheels are larger than for the other. Due to the rigid connection between the wheels the angular velocity of the wheels must be the same, so the wheelset will yaw and steer towards the track center line. The wheelset overshoots and is displaced to the opposite side. As illustrated on figure 1.1 the process is repetitive.

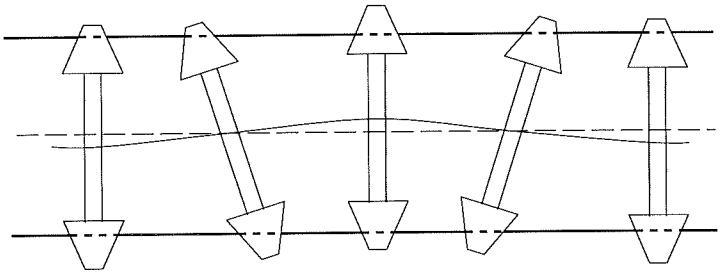

Figure 1.1: The Klingel motion of a free wheelset.

This motion of a free wheelset was already analysed by Klingel in 1883. The frequency of the motion is called the kinematic frequency or the Klingel frequency of the wheelset.

Inevitably the friction forces between wheels and rails damp the oscillating motion. As we shall see in chapter 3, the friction forces depend on the speed of the vehicle. Therefore, above a certain critical speed, a wheelset can oscillate laterally. The vehicle becomes unstable and the wheelset is said to hunt.

Hunting gives rise to large contact forces between wheels and rails and must be avoided when a railway vehicle is designed. It is the shape of the wheel and the rail profiles and the suspension elements in the car, that mainly affect the stability. Especially a restraining of the yaw of the wheelset relative to the bogie or car body counteracts hunting.

Let us return to the free wheelset and consider the wheelset running in a curve. The situation is shown in figure 1.2. The wheelset is displaced laterally in such a way that the difference in the rolling radius of the two wheels creates a yaw velocity of the wheelset which corresponds to the curve radius. Due to the conical profiles, a free wheelset is thus able to steer itself through a curve.

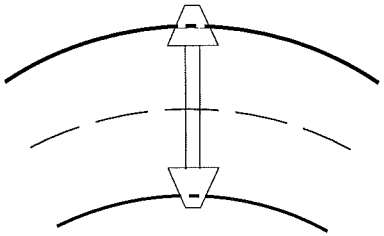

Figure 1.2: A free wheelset in a curve.

When the wheelset is connected to a car the suspension elements counteract the self-steering effect in curves. Especially a restraining of the yaw of the wheelset have a negative effect on the curving behaviour.

The railway vehicle designer is in a dilemma; on one hand he wants a stable vehicle for all operational speeds and on the other hand he wants a good performance on curves. Stability may be achieved by a long wheelbase, but good curving demands a short wheelbase. A compromise solution is to put a long car body on two bogies with a short wheelbase relative to the length of the car. This is one reason why most of the passenger cars in the world have two-axle bogies.

However, these bogie cars are heavy and today the aim is for low weight vehicles with low energy consumption. Besides using new low weight material the weight can be reduced by the use of single-axle bogies and taking the above conflict into consideration.

1.2 New S-train for Copenhagen

Danish State Railways, DSB, has ordered a new low weight vehicle to meet the demands for greater transport capacity in Copenhagen. A proposal for such a vehicle has led to the development of a mono-wheelset radially-steered vehicle designed and manufactured by Linke-Hofmann-Busch in Germany.

The vehicle is an articulated train, in which four car bodies are supported by five running gears. To obtain good running behaviour both on straight track and on curves the bogies are steered in curves. The bogie construction is based on a bogie developed by Frederich from RWTH in Aachen. An illustration of the vehicle is shown in figure 1.3. Compared with a usual vehicle the car bodies are wider but shorter. For an investigation of the new train we can refer to [Ahrens, 1994].

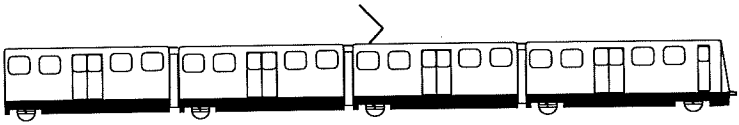

Figure 1.3: The new S-train for Copenhagen.

As a first step in the development, a test vehicle was equipped with a prototype bogie and put into regular service on the S-train network in Copenhagen. A picture of the vehicle is shown in figure 1.4. It consists of

two DSB S-train cars built in 1972, in which a bogie on the driving trailer has been replaced by a single-axle steered and motorized bogie.

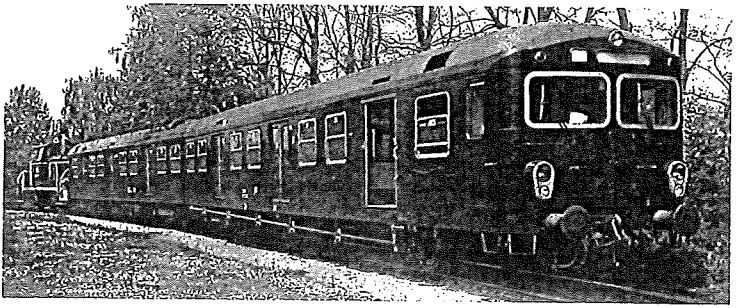

Figure 1.4: A picture of the test vehicle with a mechanical steering mechanism.

A suitable design for the steering was found to be a combination of the self-steering effect of the wheelset and a mechanical steering mechanism controlled by the yaw angles between the two cars. Due to the demand for low weight and the lack of space underneath the car bodies, further developments by Linke-Hofmann-Busch led to a hydraulic steering instead of a mechanical one. In addition the hydraulic system reduces the complexity and makes it possible to design a self-compensating system.

Other solutions for solving the conflict between curving and stable run for single-axle constructions can be found in [Wrang, 1995]. Wrang suggests that a nonlinear spring can be used as a yaw suspension instead of the steering. The spring should be stiff when running on straight track (small yaw angles) and soft when negotiating a curve (large yaw angles).

This thesis deals with the modelling and the running behavior of the first prototype of the new vehicle. The steering is treated as a mechanical system. The results presented here are not the only analysis of the vehicle, other studies by Linke-Hofmann-Busch and DSB have been made, see for instance [Rose, 1994]. In the analyses presented here we will point out the importance of nonlinear analysis.

Chapter 2

Modelling a railway vehicle

In this chapter we describe the mathematical modelling of the dynamic behaviour of a railway vehicle. We will concentrate only on the vehicle, while the modelling of the track will be discussed in a later chapter.

From a numerical point of view it is desirable to have a simple mathematical model. Therefore, when modelling a mechanical system the art is to make approximations, which do not spoil the dynamics of the system. The ideal situation is, when the model is as simple as possible and still can reproduce experimental data.

2.1 Degrees of freedom

In railway dynamics the bodies are often assumed to be rigid. This means that the elasticity of the bodies and shifting of their weight are neglected. A rigid body, which can move freely, has six degrees of freedom. These degrees of freedom are illustrated in a Cartesian coordinate system in figure 2.1.

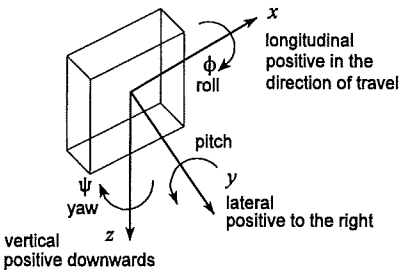

Figure 2.1: The degrees of freedom for a rigid body.

There are three degrees of freedom (longitudinal x, lateral y and vertical z) to define the position of the center of gravity from an inertial system and three degrees of freedom (roll ϕ, pitch and yaw ψ) to define the rotation of the body about the longitudinal, lateral and vertical axes.

Consequently, a mechanical system consisting of N rigid bodies can generally be described by equations of motion consisting of $6N$ second order differential equations. Constrains of rigid bodies will reduce the independent degrees of freedom. The system may be simplified by neglect of certain degrees of freedom. We must decide, which degrees of freedom it is important to include in the model.

To describe the running behaviour of the vehicle we include the lateral and vertical dynamics, while the longitudinal component of the velocity of the mass center of the bodies is assumed to be constant and is called the rolling velocity V. V is a parameter which is very important for the dynamic behaviour of the vehicle. We use V as a constant to be able to study the solutions to the system for a certain V. With a constant rolling velocity, the bodies will have no longitudinal dynamics and the degrees of freedom of the longitudinal motions can be left out.

Also the pitch motions are ignored. Except for wheelsets, where a degree of freedom for the angular velocity around the lateral main axis, ϑ is included to ensure, that the wheelset moves at a constant speed, V. This degree of freedom ensures that the sum of the longitudinal friction forces is zero. ϑ is a perturbation of the angular velocity $\Omega_0 = - V/r_0$, where r_0 is the rolling radius when the wheelset is placed in its central position. The rotation of the wheelset about its lateral main axis then becomes

$$\Omega = \Omega_0 + \vartheta = -V/r_0 + \vartheta \ . \tag{2.1}$$

The wheel axle is assumed to move freely and forces from motors, brakes, wind etc are not taken into account. Because we are interested in low frequency dynamics, we consider all bodies as totally rigid. However, as we shall see in chapter 3, the elasticity between wheel and rail is included in the

calculation of the contact forces between wheel and rail.

The degrees of freedom for each body are given in table 2.1.

Table 2.1: Degrees of freedom for a body.

Degree of freedom	Description
y	Lateral displacement of body.
ψ	Yaw rotation of body about the vertical axis.
z	Vertical displacement of body.
ϕ	Roll rotation of body about the longitudinal axis.
ϑ	The angular velocity of a wheelset about the lateral axis (only wheelsets).

2.2 Coordinate systems and transformation matrices

Let us first consider a vehicle running on a straight track. Here, the displacements of a body are calculated relative to an inertial coordinate system. The inertial system has its origin on the track center line and moves with a constant forward velocity, V with respect to a fixed reference frame. The system is positioned at the center of gravity of the body, when the body is placed in a central position with a respect to the track.

We use Newton's method to set up the equations of motion for the vehicle. The equations of motion are derived by projecting forces and rotations onto the three axes in an inertial coordinate system. To transfer forces and moments to an inertial system we have to define the various coordinate systems and the necessary transformation matrices.

In the transformation matrices we assume the displacements of the bodies in the inertial system to be so small, that the trigonometric functions of the rotations can be replaced by the linear terms in their Taylor series.

To describe the motion of the bodies we use three sets of Cartesian coordinate systems:

- (x_i, y_i, z_i) an inertial system, which has origin at the center of gravity of a body in its central position and moves with a constant forward velocity, V with respect to a fixed inertial reference frame.
- (x_B, y_B, z_B) a body coordinate system, which follows the motion of the body and has its origin at the mass center of the body.
- $(x_{con,r}, y_{con,r}, z_{con,r})$ and $(x_{con,l}, y_{con,l}, z_{con,l})$ two coordinate systems, which are attached to the right and left contact points, respectively.

The coordinate systems are shown in figure 2.2 and 2.3.

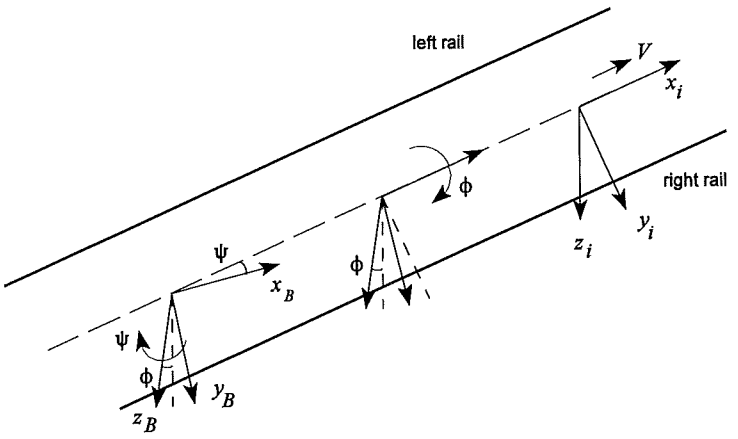

Figure 2.2: Coordinate systems to describe the motion of a body.

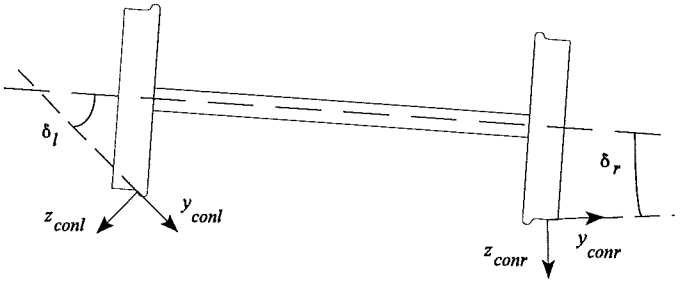

Figure 2.3: The coordinate systems attached to the contact points.

To move from the inertial system to the body coordinate system, the body is first rotated through an angle ϕ about the longitudinal inertial axis and then rotated an angle ψ about the new vertical axis. This order of rotations can be seen in figure 2.2. The transformation matrix from an inertial system to a body system, A_{Bi} becomes (see figure 2.2 or for an elaboration for example [Garg, 1986]):

$$\begin{bmatrix} x_B \\ y_B \\ z_B \end{bmatrix} = \begin{bmatrix} 1 & \psi & 0 \\ -\psi & 1 & 0 \\ 0 & 0 & 1 \end{bmatrix} \begin{bmatrix} 1 & 0 & 0 \\ 0 & 1 & \phi \\ 0 & -\phi & 1 \end{bmatrix} \begin{bmatrix} x_i \\ y_i \\ z_i \end{bmatrix}$$
$$= \begin{bmatrix} 1 & \psi & 0 \\ -\psi & 1 & \phi \\ 0 & -\phi & 1 \end{bmatrix} \begin{bmatrix} x_i \\ y_i \\ z_i \end{bmatrix} = A_{Bi} \begin{bmatrix} x_i \\ y_i \\ z_i \end{bmatrix}. \tag{2.2}$$

The transformation matrix from right contact coordinate system to the wheelset system is obtained by a rotation of the wheelset system through an angle $+\delta_r$ about the $x_{wheelset}$-axis, while the transformation matrix from left contact coordinate system to the wheelset system is obtained by a rotation of the wheelset system through an angle $-\delta_l$ about the $x_{wheelset}$-axis. δ is called the

contact angle between wheel and rail, see figure 2.3. We obtain

$$\begin{bmatrix} x_{wheelset} \\ y_{wheelset} \\ z_{wheelset} \end{bmatrix} = \begin{bmatrix} 1 & 0 & 0 \\ 0 & \cos\delta_r & \sin\delta_r \\ 0 & -\sin\delta_r & \cos\delta_r \end{bmatrix} \begin{bmatrix} x_{con,r} \\ y_{con,r} \\ z_{con,r} \end{bmatrix},$$

$$\begin{bmatrix} x_{wheelset} \\ y_{wheelset} \\ z_{wheelset} \end{bmatrix} = \begin{bmatrix} 1 & 0 & 0 \\ 0 & \cos\delta_l & -\sin\delta_l \\ 0 & \sin\delta_l & \cos\delta_l \end{bmatrix} \begin{bmatrix} x_{con,l} \\ y_{con,l} \\ z_{con,l} \end{bmatrix}. \qquad (2.3)$$

All the transformation matrices are orthogonal, so the inverse transformations are obtained by transposition of the matrices, for example $A_{iB} = A^{-1}{}_{Bi} = A^{T}{}_{Bi}$.

2.3 The equations of motion

In principle there are two philosophies in simulating the contact between wheel and rail in a railway vehicle. One can treat the wheel-rail contact as a kinematic constraint, or one can treat the wheel-rail contact as locally elastic allowing a penetration of the wheel into the rail. Using the first method the equations of motion will consist of differential equations coupled with a set of algebraic equations determining the kinematic constrains of the normal forces. Using the elastic approach we obtain instead a set of ordinary differential equations.

Here we use the more realistic method, which includes the elasticity of the steel wheel and the steel rail. We can refer to [Garg, 1986] for a description of the method applied to formulate the equations of motion using the constraint method.

The equations of motion for each body in the railway vehicle are given by

$$M\ddot{v} = F_{external} - F_{gyro}, \qquad (2.4)$$

where M is a diagonal matrix containing mass and moments of inertia of the body, $M = \mathrm{diag}(m, m, I_x, I_z)$. Index x means around the longitudinal axis and z around the vertical axis. v is a vector representing the degrees of freedom for the body, $v = (y, z, \phi, \psi)$. $F_{external}$ consists of forces and moments from suspension elements between the bodies, $F_{suspension}$ and for a wheelset the contact forces between wheel and rail, $F_{contact}$. In the equation of the vertical motion of the wheelset the gravity force due to the axle load is included in $F_{external}$. F_{gyro} is the gyroscopic moments. They are zero in the equations of motion of the displacements.

In addition the perturbation of the angular velocity of each wheelset can be found by

$$I_y \dot{\omega} = F_{contact} \text{ (moment around lateral axis)} , \tag{2.5}$$

where I_y is the moment of inertia with respect to the lateral axis of the wheelset.

2.4 Forces from suspension elements

The bodies in a railway vehicle are connected through a primary suspension between wheelset and bogie, and a secondary suspension between bogie and car body. There is of cource also a coupling between the cars.

Generally, the force from each element in a suspension is given by

$$F_{suspension} = c\,\Delta r + k\,\Delta \dot{r} , \tag{2.6}$$

where c is the stiffness matrix of the element and k the damping matrix of the element (the elements in the matrices can be nonlinear). Δr is the relative displacement between the points of attack of the suspension, and $\Delta \dot{r}$ is the relative velocity between the points of attack of the suspension.

Therefore to determine the suspension forces we need to calculate the relative displacement between the bodies to which the suspension is attached.

2.4.1 Relative displacements

The relative displacement Δr for a point on a rigid body is illustrated in figure 2.4. As the body is rotated through the transformation matrix A_{iB} relative to an inertial system, we get the following expression:

$$\Delta r = \Delta r_c + A_{iB} r_p - r_p \,, \tag{2.7}$$

where Δr_c is the displacement of the mass center of the body, and r_p is the position of the point of attack of the suspension with respect to the mass center.

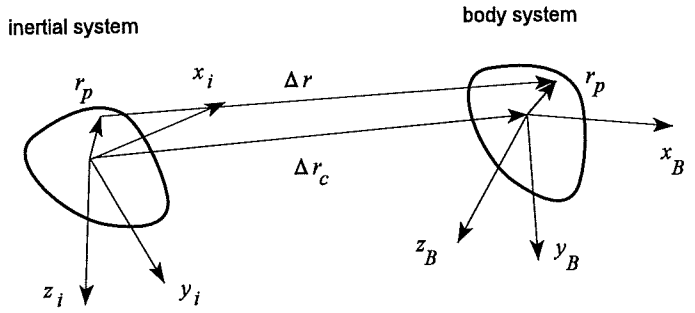

Figure 2.4: A relative displacement of a point of a body which is displaced from an inertial system.

The relation 2.7 is valid for all bodies in a multi-body system. This means that for a point on a body 1, which is rotated A_{iB1} relative to an inertial system, and a point on a body 2, which is rotated A_{iB2} relative to an inertial system, the two inertial systems being parallel, the relative displacement between the points can be calculated as

$$\Delta r_{12} = \Delta r_1 - \Delta r_2 = \Delta r_{c1} - \Delta r_{c2} + A_{iB1} r_{p1} - A_{iB2} r_{p2} - (r_{p1} - r_{p2}) \,, \tag{2.8}$$

where r_{p1} and r_{p2} can be the points of attack for a primary or secondary suspension.

2.4.2 Suspension elements

The construction parameters for the investigated vehicle have been received from Linke-Hoffmann-Busch, the manufacturer and designer of the new S-train for the Copenhagen network. The number of suspension components in the vehicle can be found in the chapters dealing with the individual models. All suspension elements are assumed to be homogeneous and linear. Generally in a railway vehicle the secondary suspension has a nonlinear characteristic, so the assumption of linearity will be valid only for small displacements of the elements.

Most of the elements are simple springs or dampers acting in one direction. In appendix A a general description is given for calculating the forces from a linear simple spring connecting two bodies.

Some elements are shear springs, which act in several directions. This means that a displacement or force from the spring in one direction can affect the behaviour in other directions. In our modelling we neglect this effect and model a shear spring as springs acting independently in each direction. A detailed discussion of shear springs and the accuracy of our approach can be found in [Eickhoff, 1993].

2.4.2.1 Damper with series stiffness

Real viscous dampers have some end stiffness in series with them. This may be due to the flexibility of the damper mountings, or the oil column in a hydraulic damper. The series stiffness will cause the effective damping to be reduced at high frequencies. At low frequencies the influence of the series stiffness is small and it is the damping coefficient, which dominates the behaviour of the damper.

Whether it is necessary to include the series stiffness in the modelling depends on the frequencies we are interested in. The frequency at which the series stiffness is dominant, is according to [Eickhoff, 1993] proportional to

the ratio between the damping and the stiffness:

$$f = \frac{1}{2\pi}\frac{c}{k}, \tag{2.9}$$

where c is the series stiffness and k is the damping coefficient.

In our vehicle there will be dampers, where this ratio is so small that the series stiffness must be included. For each of these dampers we have to include an extra degree of freedom describing the displacement between the damper and the spring, w. The damper is illustrated in figure 2.5.

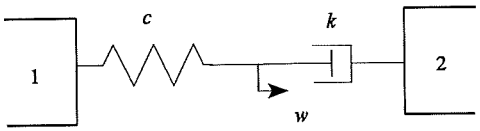

Figure 2.5: A damper with series stiffness.

Given such a damper combining two bodies, body 1 and 2, we obtain the following differential equation to determine the motion of w

$$\dot{w} = \frac{c}{k}(\Delta r_1 - w) + \Delta \dot{r}_2, \tag{2.10}$$

where Δr_1 is the relative displacement of the point of attack of the damper on body 1 and $\Delta \dot{r}_2$ is the relative velocity of the point of attack of the damper on body 2. Δr_1 and $\Delta \dot{r}_2$ are computed in the direction in which the damper acts.

The force from the damper on the two bodies, 1 and 2, is then given by

$$F_1 = c(w - \Delta r_1) \quad , \quad F_2 = k(\dot{w} - \Delta \dot{r}_2), \tag{2.11}$$

where $F_1 = -F_2$.

2.4.2.2 Links

In the vehicle considered there is a single-axle bogie, which is steered in curves by a mechanical steering system. In the construction of this steering system we find bodies connected by links. For a description of the steering system we refer to chapter 8.

When two bodies are connected by a link which acts in the three directions of displacement the points to which the link are attached on the bodies will have the same coordinates in space. Consequently the points on the bodies must have the same accelerations and the degrees of freedom of the bodies will be constrained. We assume that the bodies can rotate freely around the link. In figure 2.6 a link between two bodies is illustrated.

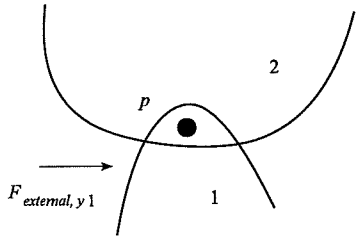

Figure 2.6: A link element combining two bodies.

The link will transfer forces between the bodies. If body 1 is disturbed by a lateral force, $F_{external,y1}$ this force will be transmitted to body 2. The lateral transferring force on body 2 is given by

$$F_{link,\,y2} = F_{external,\,y1} - m_1 \ddot{p}_{y1} \,, \tag{2.12}$$

where $\ddot{p}_{y1} = \ddot{p}_{y2}$ is the lateral acceleration at the point of attack of the link on the two bodies. m_1 is the mass of body 1. Similar in the longitudinal and vertical case.

2.5 Running in curves

A railway vehicle runs not only on straight track, but also in curves. Therefore we want to define the equations of motion for a vehicle running through a curve.

When a vehicle is negotiating a curve the difference in rolling radius caused by the profiles of the wheels will help the wheelset and hereby the whole vehicle to be steered through the curve. If the lateral main axis through the mass center of each body in the vehicle remains in line with the radius of the curve, the vehicle is steered perfectly in the curve. Because of the suspensions, the bodies in a railway car are unable to rotate freely relative to each other. The suspensions can hereby counteract the self-steering effect.

It is usually the primary suspension, which is stiff and thereby prevents the wheelsets from being steered perfectly in a curve. This results in the wheelset having an angle of attack with respect to the radial line. An illustration of the angle of attack of a wheelset, α is given in figure 2.7.

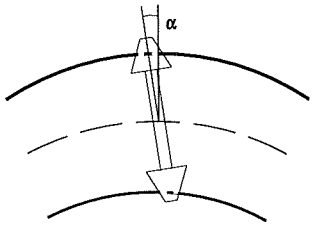

Figure 2.7: The angle of attack in a curve.

In our investigations a single-axle bogie is considered. In this case we have the angle of attack α for a rigid suspension is given by

$$\alpha = \frac{b}{R} + \psi_c \,, \tag{2.13}$$

where b is the longitudinal distance from the mass center of the car body to the mass center of the wheelset calculated with sign, and R is the radius of the curve. R is positive in a right hand curve. ψ_c is the yaw of the car body. 2.13 describes that the angle of attack increases for a decreasing radius or an increasing b.

For a two-axle bogie, where the primary suspension is assumed to be totally rigid and the secondary suspension to be soft, the angles of attack of the wheelsets depend on the semi-wheelbase and not on the longitudinal distance between the mass center of the car body and the wheelsets.

In order to prevent wear of wheels and rails there is a need for small angle of attacks. In our case the single-axle bogie obtains small angles of attack thanks to the steering mechanism, which helps the wheelset on the bogie to be kept radially on the track.

2.5.1 Cant

When running in a curve there is a centrifugal force acting on the bodies in the vehicle. For the vehicle to stay on the track this force must be balanced by an equal and opposite force on the rails. By a superelevation of the track, in such a way that the outer rail in the curve is raised compared with the inner rail, the lateral component of the contact forces can be reduced. The vertical distance between the rails is called cant, h and is illustrated in figure 2.8. The cant is positive when the left rail in the direction of travel is raised compared to the right rail (a right hand curve).

The angle between the levels of the rails and the horizontal plane is $\beta = h/1.5$. For a given β the lateral force, $F_{curve,\,y}$ in the plane of the rails in terms of centrifugal and gravity forces becomes

$$F_{curve,\,y} = -m\frac{V^2}{R} + mg\sin\beta \ , \qquad (2.14)$$

where m is the mass of the body and g is gravity. The vehicle is said to be balanced when $F_{curve,\,y}$ is zero.

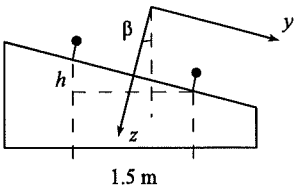

Figure 2.8: The cant in a curve.

This force must be added to the equation of motion of each body in the lateral direction. So equation 2.4 for the lateral degree of freedom will be modified to

$$m\ddot{y} = F_{external,\,y} - F_{curve,\,y} \,. \tag{2.15}$$

Because of β the gravity force in the vertical direction changes. This effect is so small however that it is negligible.

2.5.2 Coordinate systems and transformations

In order to calculate the contact forces and the suspension forces between wheelsets, bogies and car bodies in a curve we need to define different coordinate systems. There are several possibilities.

The most direct way is to place a coordinate system at the mass center of each body in its central position radial to the track. However then the coordinate systems are rotated relative to each other and it becomes more complicated to calculate the relative displacement and consequently the forces given by a suspension element.

Another way is to have parallel coordinate systems for the bodies in each car or in each bogie. This influences the calculation of contact forces. An example of using parallel coordinate systems in a bogie can be found in [Jensen, 1995]. If a whole vehicle is modelled and only the coordinate systems for the bodies in a bogie are parallel then additional transformations

are needed to calculate the forces from the secondary suspension.

We choose to use:

- $(x_{bcar}, y_{bcar}, z_{bcar})$ a basic car system, which has origin at the center of gravity of each car in its central position radial to the track. It moves with a constant velocity, V along the track center line.

- $(x_{bwheelset}, y_{bwheelset}, z_{bwheelset})$ a basic wheelset system, which has origin at the center of gravity of each wheelset in its central position radial to the track. It moves with a constant velocity, V.

The coordinate systems are illustrated in figure 2.9.

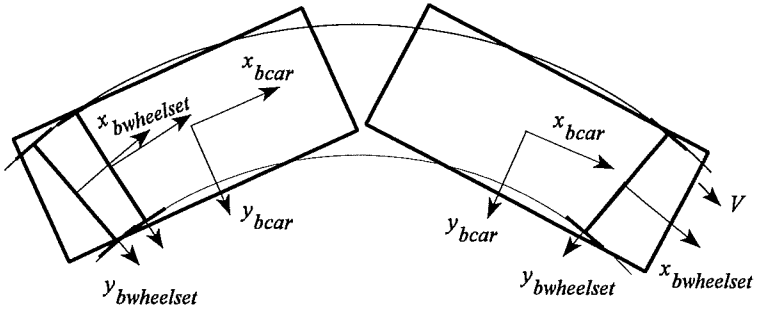

Figure 2.9: The basic coordinate system in a curve. Only a few wheelset systems are illustrated.

The reason for this choice is that we in this way can use the same calculation of contact forces for a single-axle bogie and a two-axle bogie. However we need additional transformations to calculate forces from the primary suspension and couplings between the cars.

The displacements of a wheelset are calculated in the basic wheelset system, while the displacements of all other bodies in the car (car body, bogies etc.) are calculated in the basic car system.

To determine the suspension forces in the curve we need to calculate the relative displacements. The relative displacements of a suspension element combining two bodies in the same basic system are found by the calculations described in paragraph 2.2, while other transformation matrices must be found when the suspension element combines two bodies in different basic systems.

Let us calculate the transformation from a basic wheelset system to a basic car system. A top view of the two systems are shown in figure 2.10. From the basic car system, the basic wheelset system is first rotated through an angle ζ around the longitudinal axis and then an angle α around the new vertical axis. Making the inverse rotations we obtain a rotated system parallel to the basic car system. This system is moved b in the longitudinal direction, c in the lateral direction and d in the vertical direction:

$$\begin{bmatrix} x_{bcar} \\ y_{bcar} \\ z_{bcar} \end{bmatrix} = \begin{bmatrix} 1 & 0 & 0 \\ 0 & 1 & -\zeta \\ 0 & \zeta & 1 \end{bmatrix} \begin{bmatrix} 1 & -\alpha & 0 \\ \alpha & 1 & 0 \\ 0 & 0 & 1 \end{bmatrix} \begin{bmatrix} x_{bwheelset} \\ y_{bwheelset} \\ z_{bwheelset} \end{bmatrix} + \begin{bmatrix} b \\ c \\ d \end{bmatrix}$$

$$= \begin{bmatrix} 1 & -\alpha & 0 \\ \alpha & 1 & -\zeta \\ 0 & \zeta & 1 \end{bmatrix} \begin{bmatrix} x_{bwheelset} \\ y_{bwheelset} \\ z_{bwheelset} \end{bmatrix} + \begin{bmatrix} b \\ c \\ d \end{bmatrix} = A_{curve,cw} \begin{bmatrix} x_{bwheelset} \\ y_{bwheelset} \\ z_{bwheelset} \end{bmatrix} + r_{curve} . \tag{2.16}$$

Here we have neglected the second order terms and replaced the trigonometric functions of ζ and α by the linear terms in their Taylor series.

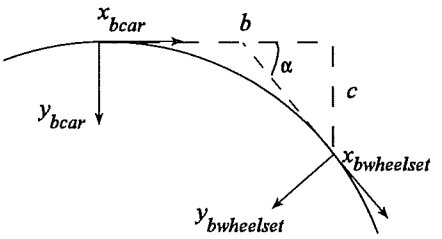

Figure 2.10: The relation between a basic wheelset system and a basic car system for a vehicle in a curve.

The transformation from the basic car system to the basic wheelset system is obtained by the inverse transformation:

$$\begin{bmatrix} x_{bwheelset} \\ y_{bwheelset} \\ z_{bwheelset} \end{bmatrix} = \begin{bmatrix} 1 & \alpha & 0 \\ -\alpha & 1 & \zeta \\ 0 & -\zeta & 1 \end{bmatrix} \left(\begin{bmatrix} x_{bcar} \\ y_{bcar} \\ z_{bcar} \end{bmatrix} - \begin{bmatrix} b \\ c \\ d \end{bmatrix} \right)$$
$$= A_{curve,wc} \left(\begin{bmatrix} x_{bcar} \\ y_{bcar} \\ z_{bcar} \end{bmatrix} - r_{curve} \right) . \qquad (2.17)$$

The longitudinal distance between the systems, b is the distance from the center of gravity of the car to the center of gravity of the wheelset, measured with appropriate sign. The other parameters are dependent on whether both coordinate systems are in the curve or not. Let us assume that the wheelset is in the front of the car. We then obtain the values listed in table 2.2. In the table, $b_{wheelset}$ is the distance the wheelset has run in the curve or out of the curve, and $h_{wheelset}$ and h_{car} is the absolute cant at the center of gravity of the wheelset and the car respectively. The case, where the wheelset has left the curve and the mass center of the car body is in the curve, is shown in figure 2.11.

Table 2.2: The parameters when negotiating a curve.

Parameter	Wheelset in curve	Both in curve	Wheelset out of curve
The longitudinal distance in the curve	$b_{wheelset}$	b	$b - b_{wheelset}$
α	$b_{wheelset}/R$	b/R	$(b - b_{wheelset})/R$
c	$(1 - \cos\alpha)R^*$	$(1 - \cos\alpha)R$	$\alpha b_{wheelset} + (1 - \cos\alpha)R^*$
ζ	$h_{wheelset}/1.5$	0	$-h_{car}/1.5$
d	$-h_{wheelset}/2$	0	$h_{car}/2$

*Only if no transition curve, otherwise c can be determined by assuming the transition curve to be a third order parabola.

If the wheelset is placed behind the mass center of the car body, the columns for the wheelset in the curve and the wheelset out of the curve are interchanged.

When calculating the relative displacements in the basic car system for a primary suspension we then use

$$\Delta r = \Delta r_{bogie} + A_{ibogie} r_{pbogie} - (A_{curve,cw}(\Delta r_{wheelset} + A_{iwheelset} r_{pwheelset}) + r_{curve}) , \quad (2.18)$$

where Δr_{bogie} and $\Delta r_{wheelset}$ are the displacements of the mass center of a bogie and a wheelset. Here we have to include the longitudinal position of the bogie in the basic car system. A_{ibogie} and $A_{iwheelset}$ are the transformation matrices from the bogie and wheelset system to the basic car and basic wheelset system (see paragraph 2.2). r_{pbogie} and $r_{pwheelset}$ are the positions of the point of attack of the suspension relative to the center of gravity of the bogie and the wheelset respectively.

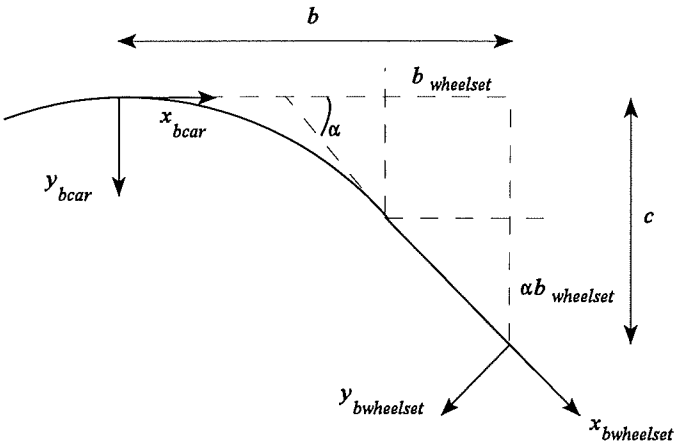

Figure 2.11: The relation between the basic coordinate system of the wheelset and the car when the wheelset is out of the curve and the car is in the curve.

Similar transformations and calculations must be made when the relative displacement in a suspension element combining two cars is to be found.

Chapter 3

The interaction between wheel and rail

In the previous chapter we have described the equations of motion for a railway vehicle and with this the calculation of suspension forces. To determine the dynamic behaviour of a railway vehicle we now need to find the contact forces between wheel and rail. The contact forces are important for both the dynamics of the whole vehicle and the track it runs on.

To find the contact forces we need to understand what occurs in the contact region between wheel and rail. To do this we refer to the degrees of freedom for a wheelset as described in chapter 2 and assume the motion of each rail to be purely translational with a lateral component, y_{rail} and a vertical component, z_{rail}. The torsion of the rails is neglected.

The contact region between wheel and rail is of the size of a finger nail. In this region large forces are created. The normal forces steem from the weight of the vehicle, and the friction forces - the so-called creep forces - develop as the result of the relative motion between wheel and rail in rolling contact. For the magnitude of both forces the geometry between wheel and rail turns out to be decisive.

It is the wheel and rail profiles, the distance between the wheels, the wheel diameter, the track gauge and the rail inclination which define the wheel-rail geometry. Knowing these properties it is possible to calculate the contact area between wheel and rail and the parameters determined by the position of contact. We refer to these parameters as the geometrical parameters.

3.1 The geometrical parameters

The geometrical parameters we use in describing the contact forces between wheel and rail, are listed in table 3.1.

Table 3.1: The geometrical parameters.

Parameter	Description
r_r and r_l	Rolling radius of right and left wheel.
δ_r and δ_l	Contact angle between the wheel-axle and the right and left contact plane.
z_r and z_l	The vertical coordinate of right and left contact point in a coordinate system at the rails.
a_r and a_l	The absolute distance from the center of gravity of the wheelset to the right and left contact point.
$a_{rail,r}$ and $a_{rail,l}$	The absolute distance from the track center line to the right and left contact point.
$R_{wheel,r}$ and $R_{wheel,l}$	Radius of curvature of the wheel profile at the right and left point of contact (positive with a center inside the wheel).
$R_{rail,r}$ and $R_{rail,l}$	Radius of curvature of the rail profile at the right and left point of contact (positive with a center inside the rail).

To locate the contact point between wheel and rail we assume both the wheel and rail to be rigid. In this way, four of the degrees of freedom for a wheelset will be dependent. We have the lateral motions of the wheelset

- the lateral displacement, y_w
- the yaw rotation, ψ_w

and the vertical motions

- the vertical displacement, z_w
- the roll rotation, ϕ_w

Given two of these degrees of freedom the other two follow. In determining the contact we choose the lateral motions as the independent degrees of freedom and the vertical motions as the dependent degrees of freedom. The reason is that the changes in the vertical coordinates are smaller than in the lateral coordinates for small displacements of a wheelset. When a wheelset has flange contact the contrary is the case and it gets more complicated to use the lateral motions as the independent degrees of freedom.

Two criteria must be fulfilled at the contact point:

- The contact point on the wheel must have the same coordinates in an inertial system as the contact point on the rail.

- The wheel and rail profiles must be tangential at the contact point.

For real wheel and rail profiles these criteria are impossible to calculate analytically. Because an analytical expression is preferable, we often find assumptions regarding the wheel and rail profiles when the dynamics of a railway vehicle is analysed.

The most frequent and simplest way to treat the profiles is to assume the wheel to be conical and the rail to be a knife-edge or an arc of a circle, see figure 3.1. With these assumptions the contact angle δ will be the same as the cone angle of the wheel λ, and the difference between the rolling radius on the left and the right wheel will be a linear function of the lateral displacement of the wheelset, y_w:

$$r_r - r_l = 2\lambda y_w \,. \tag{3.1}$$

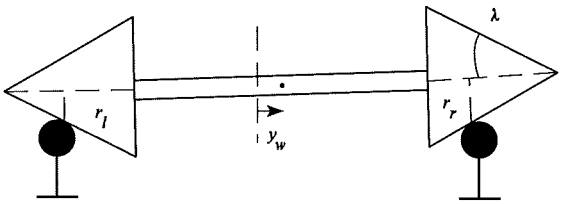

Figure 3.1: The wheels as a cone and the rails as an arc of a circle.

Giving a non-conical wheel profile we can define a so-called equivalent conicity, λ_e, which is a linearisation of the tread of the profile

$$\lambda_e = \frac{1}{2}\frac{\partial(r_r - r_l)}{\partial y_w}\Big|_{y_w = 0} . \tag{3.2}$$

A big gradient of the change in the difference in the rolling radius will give a large equivalent conicity.

The equivalent conicity is often used to make linear calculations of the stability of a railway vehicle. Using a Root Locus analysis Wickens in 1965 found an approximate relation between the linear critical speed (the speed when the vehicle becomes unstable from a linear consideration, see chapter 4) and the equivalent conicity, [Wickens, 1965a]:

$$V_{linear} \propto \frac{1}{\sqrt{\lambda_e}} . \tag{3.3}$$

The pattern is that an increasing conicity will lower the linear critical speed. [Slivsgaard, 1992] made an analytical calculation of the linear critical speed of a single wheelset and the result agrees with 3.3.

When we investigate the nonlinear dynamics of a vehicle we need to consider wheels and rails with realistic profiles. Realistic wheel and rail profiles are often defined by segments of arcs of circles and cones. In that case it is possible to find the geometrical parameters only by a numerical method.

In our determination of the contact point we use a program developed by W. Kik. The program is called RSGEO, [Kik]. The profiles of the wheel and rail are defined in the program by B-splines approximations. These approximations must be done very carefully, especially if a profile is given by measured data.

An iterative procedure is used to fullfil the two criteria for the contact point described above. For each lateral motion the wheelset is exposed to the corresponding vertical motions that ensure the wheels keep in contact with the rails. The result of the calculation is the position of the contact point and consequently the geometrical parameters.

When we want to simulate the dynamic behaviour of a vehicle we need to know the contact point for each position of the wheelsets. Instead of calling RSGEO online in the simulations we make a table of the geometrical parameters as functions of the lateral displacement of a wheelset. In the simulations we then make a linear interpolation between the data in this table. The table is made for each wheel and rail configuration with an interval of ±10 mm in the lateral displacement with a step of 0.05 mm.

If the wheelset is running parallel to the track the longitudinal position of the contact point will be in line with the lateral main axis through the center of gravity of the wheelset. A yaw motion of the wheelset will move the contact point in a longitudinal direction and give rise to changes in the geometrical parameters. The longitudinal motion of the contact point is illustrated in figure 3.2.

Assuming the wheels to be conical a linearised expression for the longitudinal motion of the contact point at right and left wheel can be found

$$\Delta x_r = r_r \psi_w \tan \delta_r \quad , \quad \Delta x_l = -r_l \psi_w \tan \delta_l \, . \tag{3.4}$$

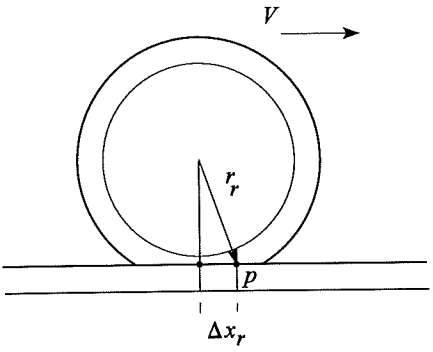

Figure 3.2: The longitudinal position of the contact point under yaw. p is the point of contact.

So Δx_r (see figure 3.2) grows with the yaw of the wheelset.

Generally, the yaw angle of a wheelset is so small that the longitudinal displacement Δx_r can be neglected. However for a vehicle running in very narrow curves, large yaw angles can occur and result in large longitudinal displacements. According to Scott from BR Research the radius of a curve should be less than 200 m before the longitudinal position of the contact point will be significant, [Jensen, 1995]. This is of course dependent on the construction of the vehicle and consequently the stiffness of the suspensions which affect the yaw motion.

Beside the effect on the geometrical parameters, the main effect of the longitudinal displacement of the contact point is that a component of the contact forces gives rise to a moment, which prevents the wheelset from yawing.

In our investigations we neglect the influence of the longitudinal displacement of the contact point.

3.1.1 The geometry of the nominal profiles in DSB

The analysed vehicle has the DSB82-1 wheel profile and runs on a track with UIC60 or DSB45 rail profiles. The dimensions of these profiles are given in appendix E.

The DSB82-1 wheel profile is the most common wheel profile used in DSB. It is a so-called wear profile, which means that its shape and consequently the equivalent conicity changes only a little as the wheels get worn. The change in the inverse radii of curvature of the profile as a function of the lateral displacement of the wheelset is given in figure 3.3.

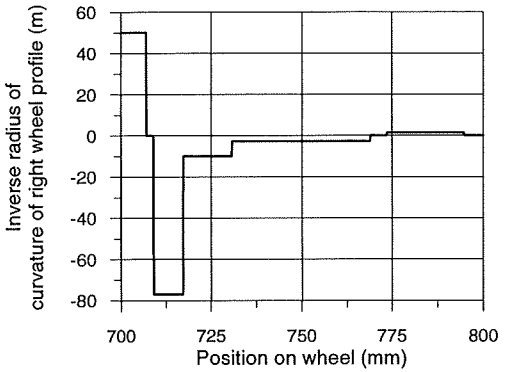

Figure 3.3: The inverse radius of curvature of right wheel for a DSB82-1 wheel profile.

The UIC60 rails are used on almost all main lines bearing a lot of traffic, while the DSB45 rails are used on side lines with less intense traffic and on some of the Copenhagen S-train lines. Comparing the two rails the main difference is the weight: UIC60 is a 60 kg/m rail and DSB45 is a 45 kg/m rail. The UIC60 rails are the most common rails in Europe.

There are two important terms beside the rail profiles when a track is defined: The inclination of the rail web to the vertical axis and the track gauge. The track is shown in figure 3.4. The gauge is defined as the distance between the

rails measured from a point 14 mm below the crown of the rails. The most common track gauge is 1435 mm, but a nominal gauge of 1432 mm can also be found on the infrastructure of DSB. During the last six years DSB has fastened the rails on the sleepers with an inclination of 1/40. Before that time the inclination was 1/20.

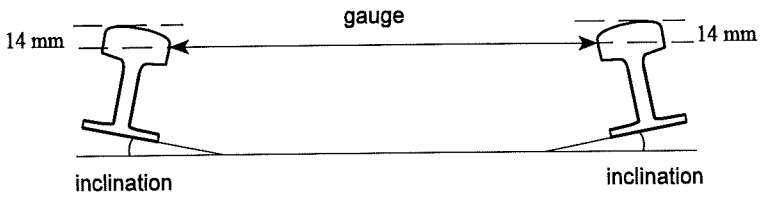

Figure 3.4: An illustration of the track gauge and the inclination of the rails.

In the investigations here we limit ourselves to consider only one value of gauge. Some analysis of the effect of different gauges can be found in [Jensen, 1995]. We have chosen to calculate the position of the contact point and the geometrical parameters for the following track configurations

- UIC60 rails with a gauge of 1435 mm and an inclination of 1/20 or 1/40.
- DSB45 rails with a gauge of 1435 mm and an inclination of 1/20 or 1/40.

Figure 3.5 shows the position of the contact point on the right wheel and right rail as a function of the lateral displacement of a wheelset. The vertical lines indicate the position of the contact points, when the wheelset is placed in its central position. This position is moved towards the flange for the 1/40 inclination. Notice there will be areas on the profiles where no contact point exists.

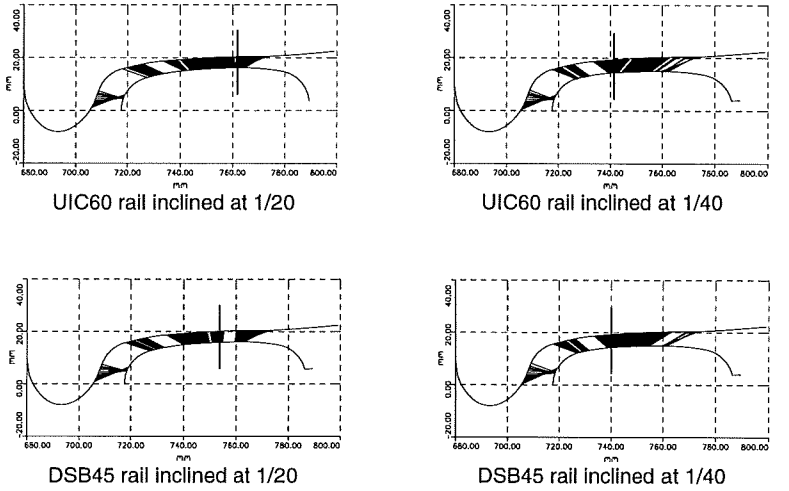

Figure 3.5: The position of contact of right wheel and right rail for different lateral displacement of the wheelset. The vertical line is when the wheelset is placed in its central position. The four track configurations are shown.

The variation of the rolling radius is given in figure 3.6 and 3.7. Figure 3.6 is for UIC60 rails and figure 3.7 is for DSB45 rails. The figures illustrate a nonlinear dependency between the rolling radius and the lateral displacement of the wheelset.

Around the central position the slope of the curves in the figures will be greater for a DSB45 rail inclined at 1/20 as for the others. This indicates that the equivalent conicity is bigger for a DSB45 rail inclined at 1/20 than for the other track configurations. The equivalent conicities are computed to

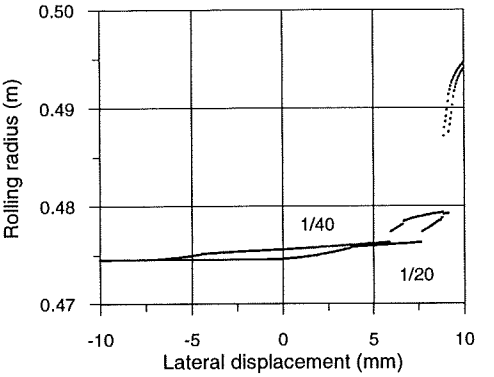

Figure 3.6: The rolling radius of right wheel when the rails are UIC60 rails inclined 1/20 or 1/40.

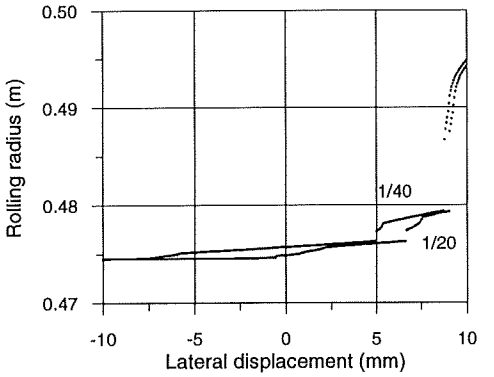

Figure 3.7: The rolling radius of right wheel when the rails are DSB45 rails inclined 1/20 or 1/40.

- $\lambda_e = 0{,}109$ for UIC60 inclined at 1/20
- $\lambda_e = 0{,}102$ for UIC60 inclined at 1/40
- $\lambda_e = 0{,}270$ for DSB45 inclined at 1/20
- $\lambda_e = 0{,}108$ for DSB45 inclined at 1/40

where a Δy_w of 2 mm is used.

In the figures of the rolling radii we see some jumps in the rolling radius as the wheelset reaches the flange. Considering the other geometrical parameters we also find jumps. The explanation for these jumps is that for lateral displacements near the jumps, there is a two point contact. In the calculation of the contact points the wheels and rails are assumed to be rigid, and we neglect the possibility of two point contact. However as we shall see in paragraph 3.2, when we calculate the contact forces we search for two point contact around the jumps. The lateral displacement of the wheelset at the two main jumps is given in table 3.2.

Table 3.2: The two main jumps in the geometrical parameters.

Track configuration	Lateral displacement (mm)	
	jump 1	jump 2
UIC60 inclined at 1/20	7,70	9.15
UIC60 inclined at 1/40	5.95	8,90
DSB45 inclined at 1/20	6.65	9.05
DSB45 inclined at 1/40	4.95	8.75

3.1.2 Non ideal configurations

Wheel and rail profiles will change due to wear as the vehicle continues running on the track. It is possible to measure these worn profiles. DSB uses a measuring instrument, developed by Greenwood engineering, [Esveld, 1992]. A measured profile can be approximated by B-splines with care and used in RSGEO. Because the wheel profiles do not change along the track, calculations with worn wheel profiles are fairly straightforward. In [Jensen, 1995] simulations of the dynamics of the Danish IC3 train with worn profiles have been made. On the other hand, the shape of the rails change along the track. To include these changes, it is necessary to make a table of the geometry for each profile. In our investigations we use only nominal wheel and rail profiles.

Also the position and consequently the gauge of the track will vary. The position of the track is in DSB measured by the track recording car, Matissa MVP8. To describe the position of a track a transfer function of the measured data has to be made. A detailed description of the track recording car and the analysis of data can be found in [Måleteknik, M007/94]. We will use such analysed data, when we simulate the dynamic behaviour of a vehicle running on a track with irregularities in chapter 9.

When the gauge varies the geometrical parameters do not only depend on the lateral displacement of the wheelset, but also on the gauge. Therefore we need a two-dimensional table of the geometry. Figure 3.8 shows the rolling radius in dependence on the lateral displacement of the wheelset for three different gauges. The figure indicates that a change in the gauge will result in a parallel shifting of the geometrical parameters.

Instead of a two-dimensional table, the geometry for different gauges can therefore be approximated by a shift. Defining two functions describing the geometrical parameters for right and left wheel, $geometry_r(g, y_w)$ and $geometry_l(g, y_w)$ as a function of the gauge g and the lateral displacement of the wheelset we get

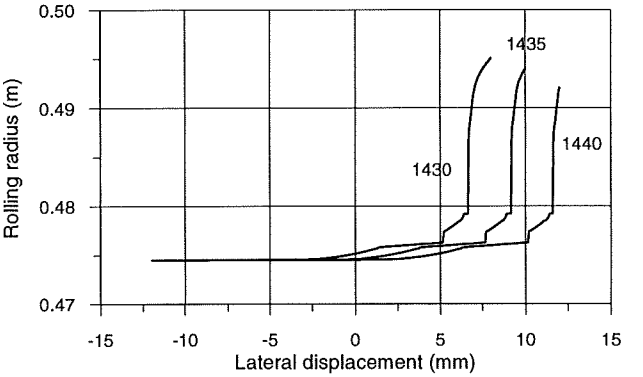

Figure 3.8: The rolling radius of right wheel for three different gauges: 1430 mm, 1435 mm, and 1440 mm. The rails are UIC60 rails inclined 1/20.

$$\begin{aligned} geometry_{\,r}(g = g_0 \,,\, y_w = y_{w0}) &\approx geometry_{\,r}(g = g_0 - \Delta \,,\, y_w = y_{w0} - \frac{\Delta}{2}) \,, \\ geometry_{\,l}(g = g_0 \,,\, y_w = y_{w0}) &\approx geometry_{\,l}(g = g_0 - \Delta \,,\, y_w = y_{w0} + \frac{\Delta}{2}) \,. \end{aligned} \tag{3.5}$$

The equations describe that the geometry for a given gauge g_0 and a given lateral displacement y_{w0} is approximately the same as the geometry for a different gauge $g_0 - \Delta$ and a lateral displacement of right wheel of $y_{w0} - \Delta/2$ and of left wheel of $y_{w0} + \Delta/2$. For small Δ, equation 3.5 is fairly correct. A further discussion of the approximation can be found in [Jensen, 1995].

Assuming that equation 3.5 is valid, we can calculate the coordinates of the contact points to be used in the tables of the geometrical parameters

$$\begin{aligned} y_{contact,r} &= y_w - y_{rail,r} - y_{irr,r} \,, \\ y_{contact,l} &= y_w - y_{rail,l} - y_{irr,l} \,, \end{aligned} \tag{3.6}$$

where $y_{irr,r}$ and $y_{irr,\,l}$ are the given deviations from the nominal situation for right and left rail respectively. In our case we use a nominal gauge of 1435 mm. We call $y_{irr,r}$ and $y_{irr,l}$ the irregularities of right and left rail. They can for

example be described by the measured data. 3.6 expresses that the coordinate to be used in the table of the geometrical parameters is given by the lateral displacement of the wheelset and the lateral position of the rail.

3.2 The normal contact problem

Let us now concentrate on two bodies pressed against each other in a rolling contact. To determine the contact patch between wheel and rail we apply Hertz' theory from 1895.

For two elastic bodies in a rolling contact Hertz assumed that the surfaces of the bodies near the contact patch can be described by a second order polynomial, the curvatures of the bodies are constant through the contact patch, and the dimensions of the contact patch are small compared with characteristic diameters of the bodies. Under these assumptions Hertz found the contact region to be elliptical and the ratio of the semiaxes (a/b) to be calculated from a knowledge of the principal radius of curvature of the bodies. A drawing of this contact patch is shown in figure 3.9.

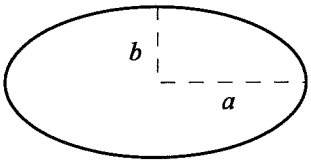

Figure 3.9: The contact ellipse according to Hertz.

Because contact between the two bodies occurs in a plane Hertz' theory yields that the normal pressure distribution is independent of the tangential force. A detailed description of Hertz' theory can be found in [Kalker, 1990]. Here we use only the results.

3.2.1 Determination of the contact ellipse

Let N be the force with which the wheel and rail are pressed against each other. The longitudinal semiaxis, a and the lateral semiaxis, b of the contact ellipse can then be calculated as

$$a = m\sqrt[3]{\frac{3N}{4(A+B)}2\frac{1-\sigma^2}{E}},$$
$$b = n\sqrt[3]{\frac{3N}{4(A+B)}2\frac{1-\sigma^2}{E}}, \tag{3.7}$$

where m and n is a function of θ given by

$$\theta = \cos^{-1}\frac{A-B}{A+B} \tag{3.8}$$

and

$$A+B = \frac{1}{2}\left(\frac{1}{r}+\frac{1}{R_{wheel}}+\frac{1}{R_{rail}}\right),$$
$$A-B = -\frac{1}{2}\left(\frac{1}{r}-\frac{1}{R_{wheel}}-\frac{1}{R_{rail}}\right). \tag{3.9}$$

The modulus of elasticity, E is assumed to be the same for the steel wheel and steel rail, $E = 2.1 \cdot 10^{11}$ N/m^2. For Poissons ratio,σ we use $\sigma = 0.25$. A tabulation of m and n as a function of θ can be found in [Garg, 1986].

We notice that the contact ellipse varies along the profiles and consequently depends on the position of the contact.

3.2.2 Normal forces

When we calculate the normal forces the wheel and rail can be considered as either rigid or elastic. A rigid model has been used widely in railway simulations. A problem with this method is that it can give unrealistic changes in the normal forces around flange contact. These changes occur

smoother in an elastic model, because an elastic model can take account of situations such as multi point contact and wheel lifting.

During the last few years great attention has been given to development of elastic models. Especially Pieotrowski, Kik, Pascal and Sauvage have dealt with the modelling of elastic multi-contact problems. As an example we can refer to [Pascal, 1991]. A comparison between using an elastic method and a rigid method in the simulations of the dynamics of a railway bogie can be found in [Jensen, 1994].

When we calculate the contact forces we use an elastic approach. The method is inspired by [Sauvage, 1990] and described by [Jensen, 1995]. It is based on the theory of Hertz. We refer to [Jensen, 1995] for a description of the method. The main result is that there is a relation between the penetration of the wheel into the rail and the normal force, N.

For a wheel load of N, the wheel and rail penetrate each other over a distance q(N). The penetration is illustrated in figure 3.10.

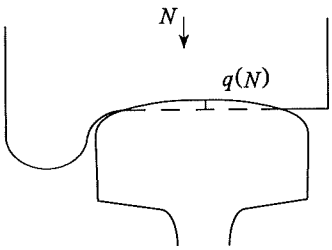

Figure 3.10: The penetration of the wheel into the rail.

The force is found by

$$N = \left(\frac{q(N)}{q(1)} \right)^{\frac{3}{2}}, \tag{3.10}$$

where $q(1)$ is the penetration for a wheel load of 1 N. We can use 3.10 to define an equivalent stiffness

$$c_{hertz} = \frac{N}{q(N)} = \frac{N^{\frac{1}{3}}}{q(1)}, \tag{3.11}$$

where c_{hertz} is called the Hertzian spring. If the stiffness is known we can find the normal force by calculating the penetration.

Because the penetration depend on the point of contact, $q(1)$ and consequently c_{hertz} will vary with the lateral displacement of the wheelset. Such variations are shown in [Jensen, 1995] for different track configurations. In our simulations we approximate the Hertzian spring with a constant stiffness of $1 \cdot 10^9$ N/m.

For each position of the wheelset and the rails we can calculate the penetration of the wheel into the rail, Δp_z. Δp_z is the distance between wheel and rail in the direction of the normal to the contact plane. This penetration corresponds to $q(N)$ when N is the force along the normal to the contact plane. We find N by computing

$$N = -c_{hertz} \Delta p_z \approx -1 \cdot 10^9 \text{ N/m } \Delta p_z . \tag{3.12}$$

The expressions for the penetration are derived in appendix B. For the right and left wheel we get

$$\begin{aligned} \Delta p_{z,r} &= \sin \delta_r (a_{rail,r} - a_r + y_{rail,r} + y_{irr,r} - y_w + \phi_w r_r) + \\ &\quad \cos \delta_r (z_0 + r_0 - z_r - r_r + z_{rail,r} + z_{irr,r} - z_w - \phi_w a_r) , \\ \Delta p_{z,l} &= -\sin \delta_l (-a_{rail,l} + a_l + y_{rail,l} + y_{irr,l} - y_w + \phi_w r_l) + \\ &\quad \cos \delta_l (z_0 + r_0 - z_l - r_l + z_{rail,l} + z_{irr,l} - z_w + \phi_w a_l) , \end{aligned} \tag{3.13}$$

where z_0 and r_0 are the vertical coordinate of the contact point and the rolling

radius when the wheelset is placed in its central position. If the vehicle is running on a track with irregularities, $y_{irr,r}$, $y_{irr,l}$, $z_{irr,r}$ and $z_{irr,l}$ describe the lateral and vertical irregularities of right and left wheel respectively. Otherwise, $y_{irr,r}$, $y_{irr,l}$, $z_{irr,r}$ and $z_{irr,l}$ are set to zero.

When we calculated the geometrical parameters we found some places on the profiles where no contact took place. Consequently there were jumps in the geometrical parameters for certain lateral displacements of the wheelset (see table 3.2). Near these jumps there is a possibility of more than one contact point. An example of two point contact is illustrated in figure 3.11. The figure displays the positions of contact on the rail and the corresponding contact ellipses.

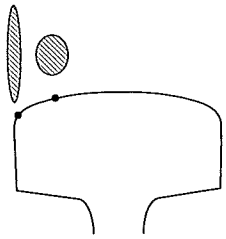

Figure 3.11: Two simultaneous contact points.

If the wheelset in the simulations obtains a lateral displacement corresponding to a displacement near a jump we first find the main contact patch and then we perturb the wheelset laterally to look for a possibility of contact at the other side of the jump. Contrary to the method described in [Pascal, 1991], the two contact areas are treated independently.

3.3 The tangential contact problem

The contact region between wheel and rail will consist of a region with slip, where the bodies slip over each other, and a region with adhesion, where the bodies because of friction are glued together. The result is, that the two elastic bodies seem to slide slowly at the contact. This phenomenon is called creep or creepage and gives rise to the creep forces. An illustration of how the slip and adhesion region can be, is shown in figure 3.12.

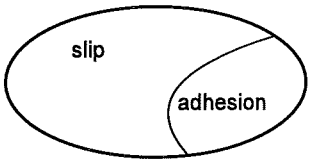

Figure 3.12: An example of the areas of slip and adhesion.

3.3.1 Creepage

In the contact area three different forms of creep exist: longitudinal, lateral and spin creep. The longitudinal creep, ξ_x and the lateral creep, ξ_y are the relative velocity between wheel and rail in the contact plane. The spin creep, ξ_{sp} is the relative angular velocity between wheel and rail about an axis normal to the contact plane.

The creepages are defined by

$$\xi_x = \frac{(\text{longitudinal velocity of wheel} - \text{longitudinal velocity of rail})_{\text{at contact point}}}{\text{rolling velocity}},$$

$$\xi_y = \frac{(\text{lateral velocity of wheel} - \text{lateral velocity of rail})_{\text{at contact point}}}{\text{rolling velocity}},$$

$$\xi_{sp} = \frac{\begin{array}{c}(\text{angular velocity of wheel} - \\ \text{angular velocity of rail})_{\text{around the normal to the contact plane}}\end{array}}{\text{rolling velocity}},$$

where the rolling velocity is the forward speed of the vehicle, V.

The velocity of the wheel consists of a translatory motion and an angular velocity of the wheel-axle. The velocity of the rail is only a translatory motion. The creepages are calculated in appendix C. Neglecting the second order terms of displacements and rotations we obtain the following results:

For the longitudinal creep on right and left wheel we find

$$\begin{aligned} \xi_{x,r} &= 1 - \frac{a_r}{R} + \frac{r_r\Omega - a_r\dot{\psi}_w}{V}, \\ \xi_{x,l} &= 1 + \frac{a_l}{R} + \frac{r_l\Omega + a_l\dot{\psi}_w}{V}. \end{aligned} \tag{3.14}$$

The lateral creep on right and left wheel is

$$\begin{aligned} \xi_{y,r} &= -\frac{\psi_w}{\cos\delta_r}\left(1 - \frac{a_r}{R}\right) + \frac{\dot{y}_w - r_r\dot{\phi}_w - \dot{y}_{rail,r}}{V\cos\delta_r}, \\ \xi_{y,l} &= -\frac{\psi_w}{\cos\delta_l}\left(1 + \frac{a_l}{R}\right) + \frac{\dot{y}_w - r_l\dot{\phi}_w - \dot{y}_{rail,l}}{V\cos\delta_l}. \end{aligned} \tag{3.15}$$

Finally, the spin creep is given by

$$\xi_{sp,r} = \frac{\Omega \sin \delta_r + \dot{\psi}_w \cos \delta_r}{V}, \qquad \xi_{sp,l} = \frac{-\Omega \sin \delta_l + \dot{\psi}_w \cos \delta_l}{V}. \tag{3.16}$$

For straight track the reciprocal of the radius, $1/R$ is zero. If the track is assumed to be rigid the lateral velocities of the rails are zero, or if the track is assumed to move as one body the motion of the two rails is identical: $y_{rail,r} = y_{rail,l}$.

3.3.2 Creep forces

To determine the relation between creep and creep forces it is necessary to solve the rolling contact problem by calculating the slip and adhesion region, and finding the resulting shear stress distribution.

The first contact theory was developed by Carter in 1926. Carter investigated a two-dimensional contact problem. Extensions of Carter's theory to the three-dimensional contact problem was studied throughout the 60's. The main contributers were Johnson, Vermeulen and Kalker. Today an exact nonlinear theory has been developed by Kalker. For a detailed survey of contact theories we refer to [Kalker, 1990].

For small creepages, the relation between creep and creep forces is approximately linear. Assuming the area of slip to be so small that its influence can be neglected, and Hertz' theory to apply, Kalker has developed a linear theory.

According to Kalker the linear creep forces in the longitudinal direction, $T_{x,linear}$ and the lateral direction, $T_{y,linear}$ and the linear spin-creep moment about the normal to the contact plane, $M_{z,linear}$ are given by

$$\begin{bmatrix} T_{x,linear} \\ T_{y,linear} \\ M_{z,linear} \end{bmatrix} = -Gc^2 \begin{bmatrix} C_{11} & 0 & 0 \\ 0 & C_{22} & cC_{23} \\ 0 & -cC_{23} & c^2C_{33} \end{bmatrix} \begin{bmatrix} \xi_x \\ \xi_y \\ \xi_{sp} \end{bmatrix}, \tag{3.17}$$

where

$$G = \frac{E}{2(1-\sigma)} \quad \text{and} \quad c = \sqrt{ab}\,. \tag{3.18}$$

C_{11}, C_{22}, C_{23} and C_{33} are the creep coefficients. The creep coefficients are defined by Kalker and listed in [Kalker, 1990]. They are dependent on the modulus of elasticity, E, the Poisson's ratio, σ and the ratio of the semiaxes of the contact ellipse (a/b).

The linear theory is only valid for small values of creepage. When the creepage increases the creep force - creepage relationships become nonlinear and the coefficient of adhesion, μ will have an influence. For large values of creepage the creep forces will be limited by Coulomb's law of friction, μN. In this situation, the wheel is in a condition of complete sliding. If nothing else is mentioned $\mu = 0.3$ is used in the simulations.

The nonlinear exact theory of Kalker is described in [Kalker, 1990]. The theory is not given in an analytical form, but is implemented in a program called CONTACT. Because CONTACT needs a lot of computational time it is not realistic to use it for simulations of the dynamics of a railway vehicle. Kalker has therefore developed another program called FASTSIM. FASTSIM is based on a simplified contact theory. Compared with CONTACT Kalker concludes that FASTSIM works remarkably well with errors up to 10 % in special cases with large spin. Although FASTSIM is faster than CONTACT it is not quite as fast as an analytical expression.

In search of an analytical expression we come across Johnson and Vermeulen's nonlinear theory, [Vermeulen, 1964]. Johnson and Vermeulen assumed the region of adhesion to be an ellipse just touching the leading edge of the contact ellipse. Hereby they could come up with the resulting tangential force in a formula. The effect of spin is not included in Johnson and Vermeulen's

theory.

Another theory is described by Shen, Hedrick and Elkins, [Shen, 1983]. Shen, Hedrick and Elkins combine the linear theory of Kalker and the nonlinear theory of Johnson and Vermeulen in such a way that the spin creepage is taken account of. In this approximation the creep forces and moment is first calculated by 3.17 and then restricted by the cubic saturation law of Johnson and Vermeulen:

The resultant force of Kalker's linear theory is

$$T_R' = \sqrt{T_{x,linear}^2 + T_{y,linear}^2} \,. \tag{3.19}$$

This force is reduced in accordance with Johnson and Vermeulen's theory, so the resultant nonlinear tangential force, T_R becomes

$$T_R = \mu N \begin{cases} \dfrac{T_R'}{\mu N} - \dfrac{1}{3}\left(\dfrac{T_R'}{\mu N}\right)^2 + \dfrac{1}{27}\left(\dfrac{T_R'}{\mu N}\right)^3 & \text{for } T_R' < 3\mu N \\ 1 & \text{for } T_R' \geq 3\mu N \end{cases} . \tag{3.20}$$

We then have an approximation of the nonlinear longitudinal and lateral creep forces

$$T_x = \frac{T_{x,linear}}{T_R'} T_R \quad , \quad T_y = \frac{T_{y,linear}}{T_R'} T_R \,. \tag{3.21}$$

A discussion of the validity of this theory can be found in [Shen, 1983]. The theory is suitable for all values of longitudinal and lateral creepage and for small values of spin. Kalker mentions in [Kalker, 1990] that this theory is perhaps the best nonlinear theory available today for railway simulations.

To show the shape of a creep force we have computed the lateral force using both Shen, Hedrick and Elkins' theory and FASTSIM.The results are shown in figure 3.13 and 3.14.

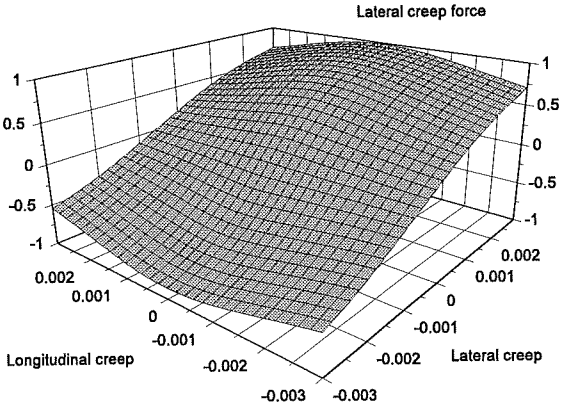

Figure 3.13: The lateral creep force in dependence of the lateral and longitudinal creepage. The spin creep is 0.3 m^{-1}. The theory of Shen, Hedrick and Elkins is used.

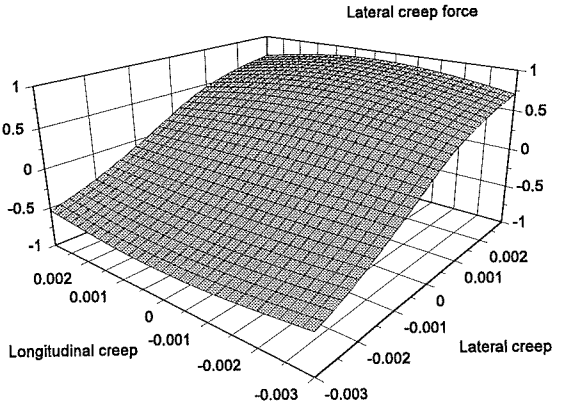

Figure 3.14: The lateral creep force in dependence of the lateral and longitudinal creepage. The spin creep is 0.3 m^{-1}. The theory of Kalker implemented in FASTSIM is used.

The figures display the lateral creep force as a function of the longitudinal and lateral creepage. The spin is chosen to be 0.3 m^{-1}. In the figures the force is normalised within the limit of adhesion, μN. The nonlinear shape of the creep force is clear. Comparing the figures we find that for large negative and positive lateral creepage there is a small deviation.

Although the simplified theory of Kalker implemented in FASTSIM is more correct than the theory of Shen, Hedrick and Elkins, we will use Shen, Hedrick and Elkins' theory. This is because Shen, Hedrick and Elkins' theory is much faster than FASTSIM. Another possibility would be to make a table of FASTSIM. This has been done for example in the simulation program SIDIVE, [Giménez, 1991]. In chapter 5 we show a simulation using FASTSIM compared with using Shen, Hedrick and Elkins' theory.

3.4 Projection of contact forces

In the above we have described how the contact forces is computed in the coordinate systems, which are attached to the contact points. To use the forces in the equations of motion the forces must be projected to the wheelset coordinate system.

This is done by using the transformation matrices described in paragraph 2.2. For the right and left contact point we get

$$
\begin{aligned}
F_{contact,r} &= \begin{bmatrix} 1 & 0 & 0 \\ 0 & \cos\delta_r & \sin\delta_r \\ 0 & -\sin\delta_r & \cos\delta_r \end{bmatrix} \begin{bmatrix} T_{x,r} \\ T_{y,r} \\ -N_r \end{bmatrix} = \begin{bmatrix} T_{x,r} \\ T_{y,r}\cos\delta_r - N_r\sin\delta_r \\ -T_{y,r}\sin\delta_r - N_r\cos\delta_r \end{bmatrix}, \\
F_{contact,l} &= \begin{bmatrix} 1 & 0 & 0 \\ 0 & \cos\delta_l & -\sin\delta_l \\ 0 & \sin\delta_l & \cos\delta_l \end{bmatrix} \begin{bmatrix} T_{x,l} \\ T_{y,l} \\ -N_l \end{bmatrix} = \begin{bmatrix} T_{x,l} \\ T_{y,l}\cos\delta_l + N_l\sin\delta_l \\ T_{y,l}\sin\delta_l - N_l\cos\delta_l \end{bmatrix}.
\end{aligned}
\tag{3.22}
$$

The moments of the creep and normal forces are found in a similar way and in addition using knowledge of the position of contact.

Chapter 4

Methods of analysis

The model of the dynamic behaviour of a railway vehicle is a nonlinear system. Because even a slightly nonlinear system can show a complex behaviour, which can never be found in the corresponding linearised system, it is important to analyse the model by nonlinear methods. During the last ten years railway dynamics analysts have become more and more aware of this fact.

To be able to analyse our models, the equations of motion are transformed to a system of first order nonlinear differential equations

$$\dot{x} = F(x,p) , \qquad x \in \mathbb{R}^N , \tag{4.1}$$

where N is the number of equations and p is a vector containing the parameters in the system. The first order system is found by a substitution of the velocities of the degrees of freedom by additional degrees of freedom.

In 4.1 the vehicle speed, V is the main parameter. If there are irregularities on the track, these are included in p and p becomes a time dependent vector.

4.1 Stability studies

One of the main problems to solve when designing a railway vehicle is to ensure the vehicle is stable at all operational speeds. The stability can be defined when the vehicle is running on a perfectly straight track without irregularities. The parameters in p will be independent of time and we can consequently analyse the solutions to the system and their stability. We use the speed as the variable parameter.

Because 4.1 is a nonlinear parameter dependent system, we can obtain different types of solutions. For a varying parameter, these can change their

stability through various bifurcations. A detailed description of bifurcation theory can be found in [Guckenheimer, 1883] or [Wiggins, 1988]. Here we outline briefly the main idea behind the local bifurcation theory:

> Given a stationary point on a flow (or a fixed point on a map), if the point is hyperbolic, i.e. the real parts of the eigenvalues of a linearization of the system around the point are different from zero (or the modulii from one), the Lyapunov theorem states that the stability of the solution can be determined by the eigenvalues. If the point is non-hyperbolic, we have a bifurcation.
>
> Let us concentrate on a non-hyperbolic point. A linearization of the parameter-dependent system around the point will be invertible, consequently the implicit function theorem guarantees that a solution exists and it will vary with the parameter. This variation is found by reducing the system using the center manifold theorem. The N-dimensional system is projected on a plane, which is tangential to the plane defined by the eigenvector(s) corresponding to the eigenvalue(s), which has a zero real part (or a unit modulus). The center manifold theorem states that this projection possesses the same dynamics around the point as the N-dimensional system. The bifurcation is analysed by an analysis of the projection.

When analysing the running behaviour of the vehicle, we are interested in stable solutions. It is however important to mention that the unstable solutions are just as important for the global picture. For a nonlinear system, the unstable solutions influence the appearance of stable solutions and their basin of attraction.

First we find the stationary solution of our system, $F(x_0, p) = x_0$. For this the degrees of freedom are zero. Except for the vertical displacements, which have a value because of the penetration of the wheels into the rails and of the motion of the rails. But by a transformation we can obtain the trivial zero-solution, $x_0 = 0$ for the stationary solution.

To determine the behaviour of the system around the stationary solution we calculate the eigenvalues of a linearization of the system around x_0. At low

vehicle speeds, the real parts of the eigenvalues are negative and the solution is attracting. At high speeds, the real parts are positive and the solution is repelling. The velocity at which the stationary solution goes from being attracting to repelling, i.e. loses its stability, is called the *linear critical speed*, V_{linear}. In railway dynamics we find the loss of stability is through a Hopf-bifurcation.

4.1.1 Hopf-bifurcation

A Hopf bifurcation is characterised by a complex conjugate pair of imaginary eigenvalues, $\pm i\omega_0$ crossing the imaginary axis. Hereby, a periodic solution with the period $T = 2\pi/\omega_0$ is created. This periodic solution can either be stable or unstable. If the solution is stable, it will exist for speeds higher than V_{linear} and the bifurcation is called supercritical. If it is unstable, it will exist for speeds lower than V_{linear} and the bifurcation is called subcritical. An illustration of the two types of Hopf-bifurcations is shown in figure 4.1.

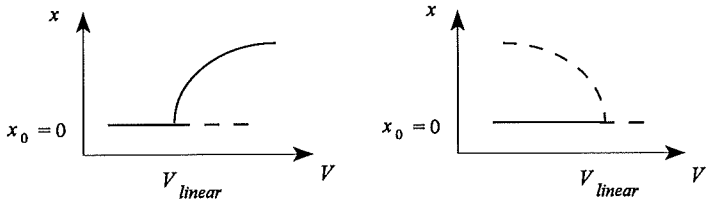

Figure 4.1: Two types of Hopf-bifurcations. The left side of the figure illustrates a supercritical bifurcation, while the right side illustrates a subcritical bifurcation. In the diagrams a solid line symbolizes a stable solution and a dotted line an unstable solution.

It is the Taylor series up to degree three, which decides the type of bifurcation. Because our system is a large system with many degrees of freedom and with complex nonlinearities we use numerical time integration around the

bifurcation and do not calculate the Taylor series to determine the type of bifurcation. Usually in railway dynamics a subcritical bifurcation is found.

4.1.2 Some bifurcations of periodic solutions

The Hopf-bifurcation creates a periodic solution, which also can bifurcate. Here we mention some of the most common bifurcations of periodic solutions found in railway systems.

A periodic solution is characterized by its repeating itself after the period. Taking a cross-section of the flow of the solution, the so-called Poincaré section, we obtain an N-1 dimensional Poincaré plane in which the oscillating solution can be described by a map, $P(x)$. The periodic solution will be a fixed point on this map, $P(x_0) = x_0$. The stability of the periodic solution is found by analysing the stability of the fixed point. For this we use the eigenvalues of the linearization of the map around the fixed point. If all the eigenvalues have a modulus less than one, the solution is stable, while it is unstable for a modulus for one eigenvalue of more than one.

When an eigenvalue crosses the unit circle through +1, the system can either undergo a saddle-node bifurcation or a symmetry-breaking pitchfork bifurcation. The bifurcations are illustrated in figure 4.2. For a saddle-node bifurcation, the two solutions collide and vanish. The figure shows the situation where a stable periodic solution reverses and becomes unstable (the bifurcation is also called a turning-point). For a symmetry-breaking bifurcation, a periodic solution becomes unstable and two asymmetric solutions are created.

When an eigenvalue crosses the unit circle through -1, the system undergoes a period-doubling bifurcation. A sketch of this bifurcation can be the same as the one for the symmetry-breaking bifurcation. A periodic solution loses its stability and a solution with the double period is created. Both for the symmetry-breaking and the period-doubling bifurcation, the solutions created may be stable or unstable. Figure 4.2 shows the case where the solutions are stable.

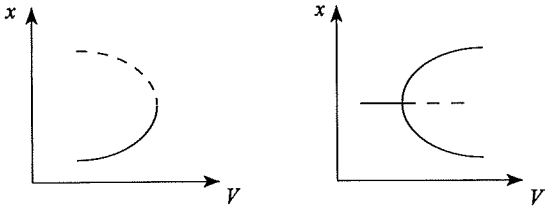

Figure 4.2: The left side of the figure illustrates a saddle-node bifurcation and the right side a symmetry-breaking bifurcation. In the diagrams a solid line symbolizes a stable solution and a dotted line an unstable solution.

4.1.3 Short introduction to chaos

Apart from being periodic or quasi-periodic, solutions can be chaotic. By a chaotic motion we mean an oscillating bounded solution which never repeats itself. Considering the solution in a Poincaré plane we find that contrary to a periodic solution, the trajectory never comes back to the same point. The points in the plane illustrate the chaotic attractor. Although the trajectory shows irregular behaviour the attractor is deterministic.

Chaotic motion is often characterized by the fact that two solutions which at one time are close at a later time can be as far from each other as the size of the attractor. We say that a chaotic motion has sensitive dependence on initial values. Therefore a good way to indicate, whether a a trajectory is chaotic or not, is to calculate the Lyapunov exponents. A Lyapunov exponent is an expression for how attracting or repelling a certain direction near the trajectory is. If one or more Lyapunov exponents are positive the trajectory is chaotic. On the other hand if the largest lyapunov exponent is zero the trajectory is periodic or quasi-periodic. More information about Lyapunov exponents and a way to compute them is described in [Parker, 1989]. Other features with chaos and methods to analyse chaos can for instance be found in [Devaney, 1989].

One way for a system to obtain chaos can be a cascade of period doubling

bifurcations. In this case, the size of the chaotic attractor will grow slowly with the parameter. An example from railway dynamics of the generic features with a period doubling cascade can be found in [Slivsgaard, 1994a]. Another way to obtain chaos can be through so-called type-I intermittency when a chaotic attractor exists immediately after a saddle-node bifurcation.

The development and appearance of chaos in models of railway systems are for instance discussed in [Kaas-Petersen, 1986], [Meijard, 1989], [Jaschinski, 1990], [True, 1992], [Slivsgaard, 1993] and [Knudsen, 1994]. An overall view is given in [True, 1993]. In general in these papers, the railway model has been fairly simple, so it has been possible to analyse them in detail. An experimental verification of the chaotic motion of a wheelset has been prensented by [Tanifuji, 1995].

4.1.4 The typical scenario

In order to determine the stability of a railway vehicle, we want to find the lowest velocity at which a stable oscillating solution occurs. We call this speed the *nonlinear critical speed*, $V_{nonlinear}$. If the Hopf-bifurcation is supercritical, the linear and nonlinear critical speeds can be the same. But as mentioned above, the loss of stability of the stationary solution occurs often through a subcritical Hopf-bifurcation. The unstable periodic solution hereby created can restore its stability in a saddle-node bifurcation. This could be at the nonlinear critical speed. This situation is shown in figure 4.3.

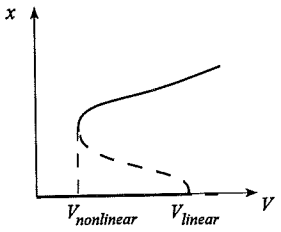

Figure 4.3: An example of a bifurcation scenario.

For velocities between the linear critical speed and the nonlinear critical speed, there exists at least three solutions:

- a stable stationary solution
- an unstable periodic solution
- a stable periodic solution

It is the basin of attraction of the solutions, which decides, which solution applies to the vehicle. Because our system is high dimensional, it is not possible to calculate the basin of attraction of the solutions. Therefore, knowing a solution for one speed, a good way of finding the solution for another speed is to follow the solution as the speed varies.

The situation shown is the most simple. Bifurcations of the periodic solutions can result in more solutions appearing. Especially the nonlinear critical speed can be determined by a saddle-node of another solution than the one created by the Hopf-bifurcation. It is therefore important to investigate the parameter space carefully.

4.2 Methods of investigation

The size of the system and the type of nonlinearities in the system cause us to analyse the system numerically. To do that we have developed a simulation program. This program is developed in combination and as a continuation of the work of [Jensen, 1995]. A rough structure of a part of the program is given in appendix F. For the time integration we use a Runge Kutta with adaptive step control, [Press, 1992].

When finding the critical speeds, we want to follow the solutions in dependence of one or two parameters. Assuming a solution is found for one value of the speed, this can be done by path-following. The linear critical speed is found by a calculation of the eigenvalues of the stationary solution, while it is more difficult and time-consuming to find the nonlinear critical speed.

One method is to use Newton-Raphson iteration to determine zero solutions for a residue function on the map of a periodic solution, $q = P(x) - x$. The method is implemented in the program PATH, [Kaas-Petersen, 1989]. This program can locate stable and unstable periodic solutions and bifurcation points in dependence on one or two parameters.

Another possibility is to use pure time integration. By altering the speed in small increments we have a good chance of staying on the same attractor. For each increment, a transient is removed so we are sure of being on the attractor. This method is slow but its advantage is that it can find all kinds of stable attractors (periodic, chaotic etc.) and the initial attractor can be aperiodic. It cannot find unstable solutions.

In our investigations we use pure time integration. To be sure that we start on an oscillating solution we start the integration using a speed above the linear critical speed. When varying the speed, the results are displayed mainly by bifurcation diagrams showing the maximum lateral displacement of each oscillation of a wheelset against the vehicle speed. If there are two asymmetric solutions both of them are shown. When varying two parameters only the bifurcations determining the critical speeds are followed.

For a system with many degrees of freedom the above method can be difficult to carry out. To get an overall picture of the influence of a parameter on the dynamic behaviour of a large system, we choose to consider the system using a transient analysis. The vehicle is disturbed laterally and after integrating over the duration of a few seconds its motion is examined. A sketch of two possible trajectories for two different speeds is shown in figure 4.4. The attractors are not found so we cannot be sure of determining the nonlinear critical speed by this method, but we can get an idea as to how attracting the oscillating motions and the stationary solution are.

When a vehicle is negotiating a curve its quasi-static position in the curve is of interest. Especially the position of the wheelset and hereby the angle of attack and contact forces describe how the vehicle is running in the curve. The fastest way to find the quasi-static position is to use a Newton-Raphson iteration. We use a more time consuming but simpler method by applying pure time integration.

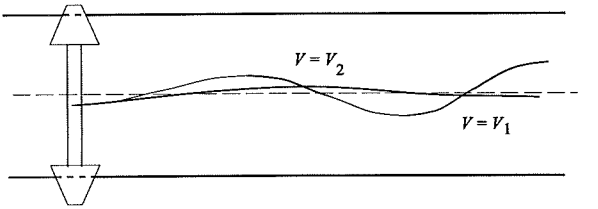

Figure 4.4: Two possible trajectories.

4.2.1 Irregularities on the track

There are many possibilities for analysing a vehicle running on a track with irregularities or going into or out of a curve. The straightforward method is to make time integration and display time series of displacements and accelerations. But further analysis of the results from the time integration can be made, for example

- Determination of comfort level for passengers. There are different methods to determine the comfort of passengers, we refer to [Eickhoff, 1993].

- Wear index or the energy dissipation given by

$$W = T_x \xi_x + T_y \xi_y + M_z \xi_{sp} .$$

- The frequency response. To study which frequencies in the irregularities of the track the vehicle is particularly sensitive to.

In this way, an idea of the consequence of variations of parameters can be found.

In our analysis of the vehicle running on a track with irregularities or entering

or leaving a curve, the parameters are held constant, so we do not analyse the results from the time integration further.

We use the simulations of the vehicle running on a track with irregularities for comparison with corresponding measurements. By this the mathematical model of the vehicle can be tested.

Chapter 5

A few remarks on modelling

To illustrate different features in the modelling we use a model of a prototype of the single-axle bogie used in the test vehicle. The bogie, which is suggested by Frederich, is called KERF (**K**urvengesteuertes **E**inzel**r**adsatz-**F**ahrwerk) and is shown in figure 5.1.

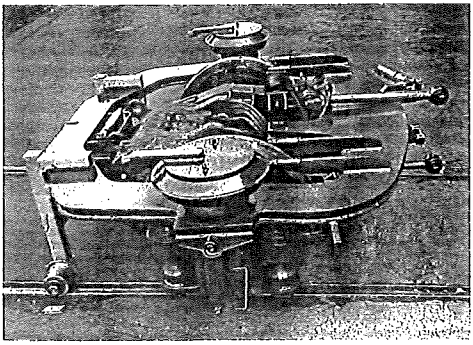

Figure 5.1: The KERF bogie.

5.1 The model

The mechanical system considered consists of a wheelset, which is connected to the bogie frame through the primary suspension. The bogie is connected to the car through the secondary suspension. Hereby the model includes three bodies: a wheelset, a bogie frame and the half of a car body. The primary task of the model is to investigate the dynamics of the bogie, therefore only half a car is considered and the yaw motion of the car is neglected.

The degrees of freedom are given in table 5.1. These degrees of freedom gives rise to a system of 25 first order nonlinear differential equations.

Table 5.1: A description of the degrees of freedom in the model of the single-axle KERF bogie.

Degree of freedom	Description
y_w	Lateral displacement of wheelset.
ψ_w	Yaw rotation of wheelset.
z_w	Vertical displacement of wheelset.
ϕ_w	Roll rotation of wheelset.
ϑ	The perturbation of the angular velocity of the wheelset around the lateral axis.
w_r	Displacement between the damper and stiffness in the right yaw damper.
w_l	Displacement between the damper and stiffness in the left yaw damper.
y_b	Lateral displacement of bogie.
ψ_b	Yaw rotation of bogie.
z_b	Vertical displacement of bogie.
ϕ_b	Roll rotation of bogie.
y_c	Lateral displacement of car body.
z_c	Vertical displacement of car body.
ϕ_c	Roll rotation of car body.

Information about the construction of the KERF bogie and its suspension elements was obtained from the company Linke-Hofmann-Busch. A sketch of the suspension elements in the bogie is shown in figure 5.2. The primary suspension consists of four springs acting in the three directions of displacement and four vertical dampers. The secondary suspension consists of two springs acting in the three directions of displacement, two longitudinal springs to prevent the bogie from pitching, one lateral damper, two vertical dampers, two longitudinal dampers with series stiffnesses the so-called yaw dampers, and two springs simulating the stiffness of the steering system.

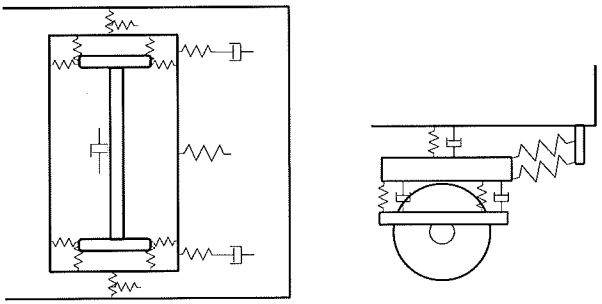

Figure 5.2: The suspension elements in the KERF bogie.

The system, which steers the single-axle bogie in curves, is modelled in this case as two springs parallel to the yaw dampers. When we only model one bogie we cannot include the yaw motion of the car and the coupling between two cars. These two motions are essential for the steering, so in this model we cannot describe the full effect of the steering. In a later chapter, where a model of two whole cars is considered, we will study the full effect of the steering system.

5.2 The analysis

In the simulations presented the bogie has the DSB82-1 wheel profile and runs on a track with UIC60 rails with an inclination of 1/20. The track is straight, perfect and completely rigid. For varying velocity, V we determine different kinds of oscillating motion.

We will use the model to investigate whether the modelling of a vehicle described in the first chapters can be simplified. Often in railway dynamics lateral and vertical motions are treated independently. However when we compute the normal forces using an elastic approach we need the vertical motions to find the normal forces. So both the lateral and vertical motions must be included.

A modelling parameter, which perhaps can be neglected, is the degree of freedom for the perturbation of the angular velocity, ϑ. The acceleration of the angular velocity is given by the longitudinal creep forces:

$$I_y \dot{\vartheta} = r_l T_{xl} + r_r T_{xr} , \tag{5.1}$$

where I_y is the moment of inertia of the wheelset around the lateral axis. T_{xr} and T_{xl} are the right and left longitudinal creep forces respectively. On straight track these forces are small for displacement of the wheelset without flange contact. Therefore we expect the influence of the perturbation of the angular velocity on the stability of the bogie to be small. This expectation will be investigated further.

To analyse which creep force theory it is necessary to use, we will calculate the creep forces using both the theory of Shen, Hedrick and Elkins, [Shen, 1983] and the simplified theory of Kalker implemented in FASTSIM, [Kalker, 1990].

In the following analysis we will hereby study the dynamics of the model of the single-axle bogie when

- using the creep force theory of Shen,Hedrick and Elkins and
  neglecting the motion of $\dot{\vartheta}$
  including the motion of $\dot{\vartheta}$

- using the creep force theory implemented in FASTSIM

The different methods are compared to study the differences between the results from the simulations and consequently the dynamics of the bogie.

5.2.1 Calculations using the theory of Shen, Hedrick and Elkins

We start computing the creep forces by applying the theory of Shen, Hedrick and Elkins. Doing this we neglect first the perturbation of the angular velocity of the wheelset.

5.2.1.1 Neglecting changes in the angular velocity of the wheelset

The stationary solution of the model will lose its stability through a subcritical Hopf-bifurcation at $V = 62.9$ m/s. Figure 5.3 shows a bifurcation diagram of the maximum lateral displacement of the wheelset as a function of the speed.

Let us consider the scenario for decreasing speed. For $V = 70$ m/s a symmetric periodic solution with flange contact exists. This solution will lose its stability at $V \approx 66.1$ m/s. A saddle-node bifurcation at $V \approx 66.5$ m/s creates a periodic solution, which vanishes at $V \approx 63.7$ m/s. In the interval of speed between 62.6 m/s $< V <$ 64.8 m/s a periodic solution exists. It has an amplitude corresponding to what marks the first jump in the geometrical parameters (see table 3.2). The amplitude increases for increasing velocity. Finally, at $V \approx 64.2$ m/s there is a saddle-node bifurcation. The stable periodic solution hereby created will for decreasing speed decrease in amplitude.

We have found an interval of speed, where three stable periodic and symmetric solutions exist: one with flange contact, one with an amplitude corresponding to just a touch of the flange and one without flange contact.

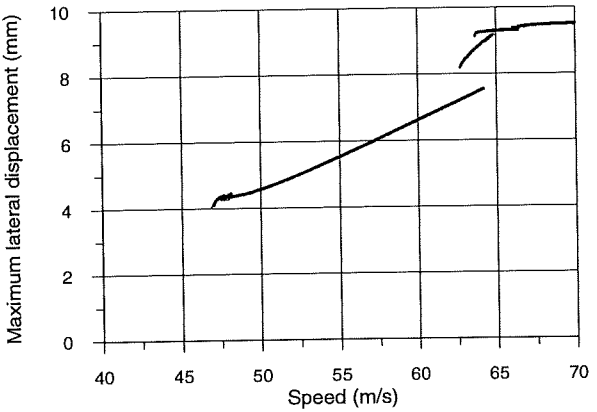

Figure 5.3: Bifurcation diagram showing the maximum lateral displacement of the wheelset against vehicle speed. The perturbation of the angular velocity of the wheelset is neglected in the computaion. Shen, Hedrick and Elkins theory is used.

A magnification of figure 5.3 is shown in figure 5.4. In figure 5.4 we find, that a symmetry-breaking bifurcation destabilizing a periodic solution at $V \approx 48.29$ m/s leads to a period adding sequence for decreasing speed. The asymmetric limit cycle undergoes a period doubling bifurcation at $V \approx 47.92$ m/s. Immediately hereafter a band of chaos exist. This band disappears quickly in a period three solution. A blow-up of the scenario for decreasing speed is shown in figure 5.5. The period three solution undergoes a symmetry-breaking bifurcation, whereafter a band of chaos exists.

Notice, the period adding sequence is periodic solutions separated by chaotic motions. Due to our system is symmetric the sequence of periodic windows for decreasing speed is: an unsymmetric period one, a symmetric period three, an unsymmetric period two, a symmetric period five, etc. Figure 5.5 shows clearly the windows in the sequence with two asymmetric period two solutions and the symmetric period five solution. Another example of a period adding sequence can be found in [Matsumoto, 1987].

A discussion of the chaotic regions is given in paragraph 5.3.

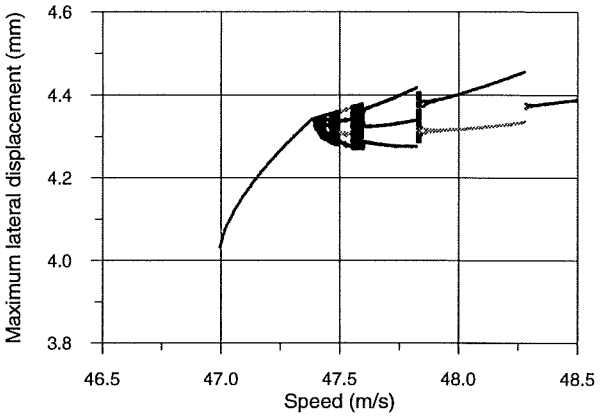

Figure 5.4: Bifurcation diagram showing the maximum lateral displacement of the wheelset against vehicle speed. A magnification of figure 5.3.

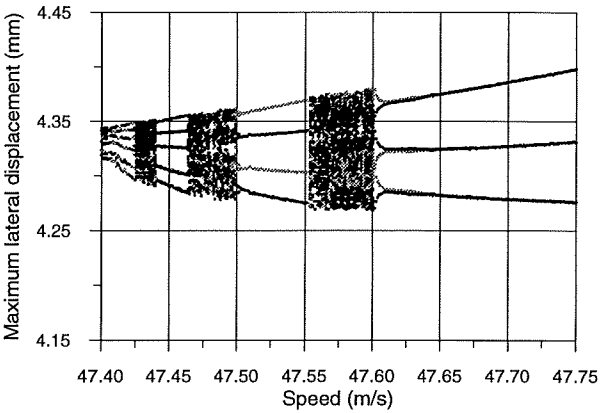

Figure 5.5: Bifurcation diagram showing the maximum lateral displacement of the wheelset against vehicle speed. A magnification of figure 5.4.

The sequence disappears at $V \approx 47.4$ m/s, where a periodic limit cycle exists. This limit cycle undergoes a saddle-node bifurcation at $V \approx 47$ m/s. For speeds below this, we have not found any oscillating solutions.

Neglecting the change in the angular velocity in our modelling, we find a linear critical speed of 62.9 m/s and a nonlinear critical speed of 47 m/s.

5.2.1.2 Including changes in the angular velocity of the wheelset

A bifurcation diagram of the maximum lateral displacement is given in figure 5.6. At $V = 70$ m/s two asymmetric solutions exist. For decreasing speed these solutions turn into one symmetric solution through a reverse symmetry-breaking at $V \approx 68.5$ m/s. The symmetric solution remains stable until $V \approx 48$ m/s, where it vanishes in a saddle-node bifurcation. Moreover, there is a stable periodic solution without flange contact in the interval of speed 50.7 m/s $< V <$ 62.2 m/s

The nonlinear critical speed is found to be $V \approx 48$ m/s, while the linear value is calculated to $V = 62.8$ m/s.

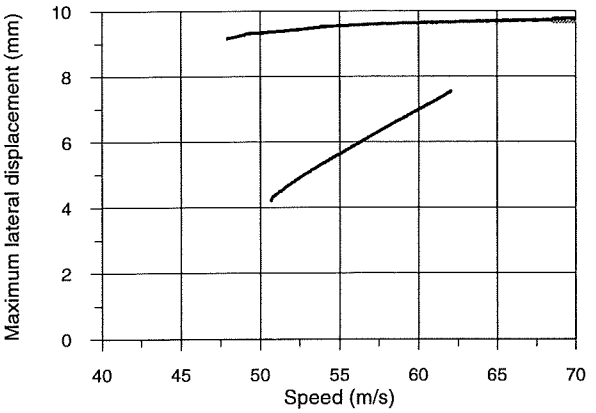

Figure 5.6: Bifurcation diagram showing the maximum lateral displacement of the wheelset against vehicle speed. The change in the angular velocity is included and the theory of Shen, Hedrick and Elkins is used.

5.2.1.3 Comparison

Comparing figure 5.6 with figure 5.3 we find an essential difference. The solution with flange contact will exist for much lower velocities, when the degree of freedom $\hat{\vartheta}$ is included in the simulations. We note that this solution does not attract particulary well at lower speeds. The nonlinear critical speed does not become lower, because the solution without flange contact vanishes at $V \approx 50.7$ m/s. This solution will not as in the case without $\hat{\vartheta}$ undergo a period adding sequence. So even for small lateral displacements the angular velocity seems to influence the dynamics.

The perturbation of the angular velocity has an appreciable value for a wheelset with flange contact. This is due to, the large spin creepage at the wheel with flange contact results in a large difference between the longitudinal creep forces at right and left wheel. The computations indicate, that the pertubation also has an influence on the nonlinear stability of the bogie. Which means that the saddle-node bifurcation, where the solution with flange contact vanishes, will be shifted towards lower speeds.

One reason why the perturbation of the angular velocity has so large an influence is, that its effect on the forces keeps the solution with flange contact stable as the speed decreases. $\hat{\vartheta}$ increases the creepage and consequently the creep forces. This means when including $\hat{\vartheta}$ in the simulations the effects in the bogie, that prevents it from oscillating, must overcome bigger forces.

From another point of view, we use that the large creepage for a solution with flange contact because of the friction loss will damp the solution. When the creepage increases due to $\hat{\vartheta}$ the oscillating solution consequently becomes more damped and less liable to bifurcate.

We reach the conclusion that the *perturbation of the angular velocity must be included* in the following simulations.

5.2.2 Calculations using the contact program FASTSIM

If we employ the program FASTSIM in computing the creep forces instead of the theory of Shen, Hedrick and Elkins we get the bifurcation diagram shown in figure 5.7.

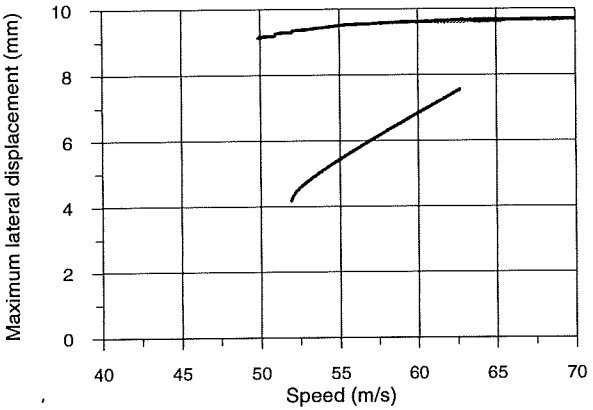

Figure 5.7: Bifurcation diagram showing the maximum lateral displacement of the wheelset against vehicle speed. The figure is computed using the creep force theory implemented in FASTSIM. The perturbation of the angular velocity of the wheelset is included.

A comparison with figure 5.6 shows that on the whole we have the same picture. A solution with flange contact will vanish at $V \approx 49.9$ m/s and another solution without flange contact will exist in the interval of speed 52.1 m/s $< V <$ 62.7 m/s. Calculating a Poincaré section of the solution with flange contact we find that two asymmetric solutions exist for $V = 62.5$ m/s. Because of the demands for high computational time and the small amplitude difference between a periodic solution and the one we have calculated, the characteristics of the solutions have not been investigated further.

With the model we obtain a nonlinear critical speed of $V \approx 50$ m/s and a linear critical speed of $V = 64.6$ m/s.

5.2.2.1 Evaluation

Calculations of the maximum lateral displacement of the wheelset indicate, that the theory of Shen, Hedrick and Elkins gives approximately the same results as FASTSIM. FASTSIM gives rise to slightly bigger critical speeds, but shows, on the whole, the same scenario of solutions. Also for a solution with flange contact where we could expect a difference in the dynamics due to the large spin creepage.

If we compute the frequencies of the oscillating solutions we find, that the solutions calculated using FASTSIM have frequencies a little higher than using Shen, hedrick and Elkins theory. Comparing the two methods, the maximum difference in frequency is found to be 0.1 Hz.

Because FASTSIM is considerably slower than the theory of Shen, Hedrick and Elkins, and because this investigation indicates, that the two creep theories yield the same results within the desired accuracy, we *apply the theory of Shen, Hedrick and Elkins* in the following chapters.

5.3 Discussion of chaotic regions

Let us study the period adding sequence from paragraph 5.2.1.1 in more details. The appeareance of a period three solution indicates that we have possibly found chaos. As stated by Li and York "period three implies chaos", [Li, 1975]. Furthermore we calculate the largest Lyapunov exponent for a trajectory at V = 47.59 m/s. It is found to converge towards 0.43. The positive value reveals we have found a chaotic transient.

To get a picture of the chaotic attractor, we calculate a Poincaré section at V = 47.59 m/s. The result is shown in figure 5.8. As often with chaotic attractors, the figure indicates that there are foldings in the attractor.

For a value of the lateral displacement of the wheelset of 4.34 mm there is a bend in the attractor in figure 5.8. At this value the curvature of the right rail is changing from 300 mm to 80 mm. All the rest of the geometrical

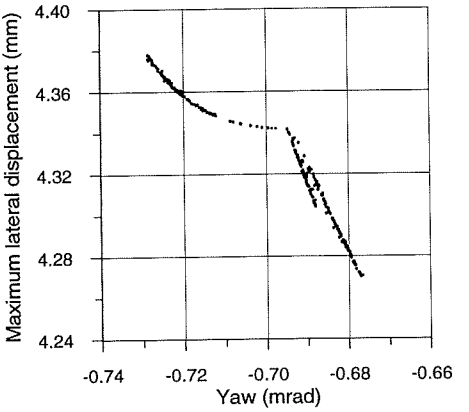

Figure 5.8: Poincaré section displaying the maximum lateral displacement of the wheelset against the yaw of the wheelset at $V = 47.59$ m/s.

parameters are smooth for values of the lateral displacement in the attractor. The curvature influence the contact ellipse between wheel and rail and consequently the creep forces. Figure 5.9 shows the contact ellipse for a curvature of 300 mm and 80 mm.

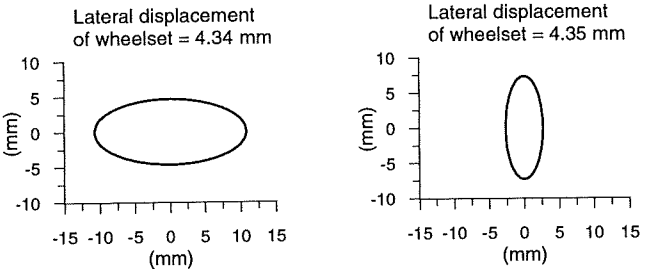

Figure 5.9: Two different contact ellipses between right wheel and rail. $R_{rail,r}$ is 300 mm for the left ellipse and 80 mm for the right ellipse.

Considering figure 5.4 for increasing speed we find that the chaotic sequence starts when the amplitude reaches 4.34 mm. The discontinuity in the curvature could hereby be the reason for the sequence.

To study this statement we make a cubic spline approximation of the curvatures. Using this the discontinuities are smoothened out. Figure 5.10 shows the inverse radii of curvature of a UIC60 rail inclined at 1/20 in dependence on the lateral displacement of the wheelset. The figure illustrates the curvature when using a linear interpolation and when the discontinuities are smoothened out by a cubic spline.

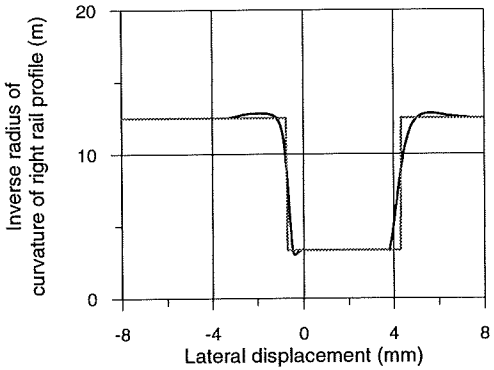

Figure 5.10: The radius of curvature of right rail as a function of the lateral displacement of the wheelset. One curve using a linear interpolation and one using a cubic spline are shown.

A bifurcation diagram of the solutions using the spline approximation is given in figure 5.11. For lateral displacements around 4 mm the figure shows that the oscillations now are periodic. The only bifurcation is a saddle-node at $V \approx 47.2$ m/s. This means, we find no period adding sequence, when the curvatures are smooth.

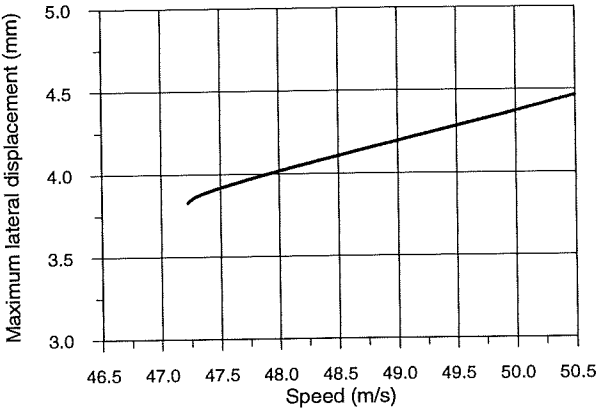

Figure 5.11: Bifurcation diagram showing the maximum lateral displacement of the wheelset against vehicle speed. In the computation a cubic spline of the radii of curvatures is used. The change in the angular velocity is neglected and the theory of Shen, Hedrick and Elkins used.

When the wheel and rail profiles are new or newly reprofiled the discontinuities in the radii of curvatures are present, however as the profiles get worn we expect these discontinuities to be smoothened out. So the situation shown can possibly be an estimate of the bogie running on slightly worn profiles.

5.4 A sum up

In this chapter we have investigated a few features in the modelling of a railway vehicle. To do this we have used a model of a single-axle bogie alone.

We have seen that neglecting the perturbation of the angular velocity of a wheelset has a considerable effect on the dynamics of the bogie. The perturbation affects the dynamics in such a way that an oscillating solution with flange contact remains stable at lower speeds if the perturbation is

included compared to it is neglected. Therefore we conclude that *the pertubation must be included* in the modelling.

The creep force theory of Shen, Hedrick and Elkins has been compared with the simplified theory of Kalker implemented in FASTSIM. Approximately the same dynamics of the bogie was found using the two theories. Therefore *the theory of Shen, Hedrick and Elkins is used* in the following simulations.

Finally we have analysed a period adding sequence for the reason for its appearance. We have found that the sequence is developed at a lateral displacement of the wheelset where there is a jump in the curvature of a rail and consequently a change of the contact ellipse. By smoothened out the jumps in curvature using a spline the period adding sequence disappears.

Chapter 6

Measurements of track flexibility

To be able to model the track we need to know some properties and parameter values for the track. In [Knothe, 1993] some values for stiffnesses and damping are given for different track elements mainly in England and Germany. Experiments under Danish conditions, where slightly different track constructions are used, can give grounds for comparison.

For such a complex system as a track it is interesting to investigate, if the characteristics of the flexibility will be nonlinear functions of the load, or if there is a difference depending on whether the load is placed over a sleeper or between two sleepers.

To achieve a better understanding of the track, the measuring group in DSB Consult has made a couple of measurements of the flexibility of the track. Because it is very difficult on the border of the impossible to measure damping, only displacements have been measured.

6.1 Test load experiment

The measuring group in DSB Consult has in week 16 of 1993 made a static test load experiment to find the characteristics of the flexibility of a given track. Tibor Gajdár from the Technical University of Budapest took part in the measurements.

Only the displacement of the track as a whole was measured, and not the displacement of the individual elements. The experiment was a pilot experiment. Because of practical reasons such as the need for working on the track for a long time, the demand for new mono-block sleepers and UIC60 rails etc, it was made on a new track near Halskov, to be more precise at km 108. The track is going to be used as a connecting to the Great Belt bridge.

6.1.1 The experiment

In the experiment we used a freight car loaded with gravel. The total load of car and gravel was 35800 kg. This gave rise to an axle-load of 17900 kg. The freight car was placed in different ways, so that one of the wheelsets rested in three different positions:

- just above one sleeper
- on the edge of a sleeper
- between two sleepers

A drawing of the positions of the wheelset is shown in figure 6.1. Here the position of the measuring points is also shown. At each measuring point a displacement transducer was attached. A displacement transducer is used for measuring the relative displacement between two points with an accuracy of a couple of hundredths of a millimeter.

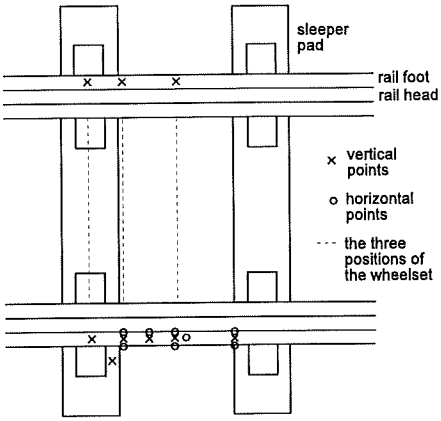

Figure 6.1: The three positions of the wheelset and the measuring points.

The change in force in the vertical direction was made by a stepwise lift of the freight car. This was done using hydraulic jacks. In this way it was possible to load and unload the track with different values. The lateral forcing of the track was made by pulling the axle using a pulley. In this way it was possible to load the track laterally by a stepwise force increasing to 25 kN. The maximum force was limited by reasons of security.

6.1.2 Test results

In the following we discuss the most important results.

Generally, we found that the displacements are independent of the position of the wheelset. Calculations in [Jønsson, 1994] reveal this. Jønsson et al. show, that the self-displacement of the rails and hereby the discrete support of the rails compared to a continuous support can be neglected, when considering the rails at low frequencies. Furthermore these results support the reproducibility of the measurements.

6.1.2.1 The lateral measurements

An example of results of the lateral measurements is shown in figure 6.2. The figure shows the lateral displacement of the rail as a function of the load and the position of the measuring points. In the figure it appears that the basic motion is a distortion of the rail web, while the whole track hardly moves sideways at all. The motion is composed of a bending of the web and a rotation of the rail, which results in a deformation of the pad. Because we did not measure the vertical motion of a point on the rail foot during the lateral measurement, we do not know how much the pad deforms. So we cannot conclude anything about the nature of the deformation.

Considering the values of the displacement we find them pretty small. The maximum is 0.2 mm for a force of 25 kN. This displacement corresponds to a distortion of the rail head about the rail foot of 1.5 mrad.

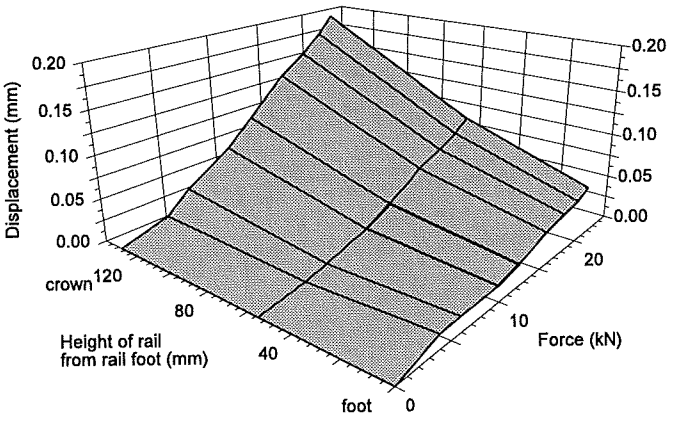

Figure 6.2: The lateral displacement of the foot, the web, and the crown of the rail as a function of the forcing.

6.1.2.2 The vertical measurements

For the vertical measurements the picture is more complicated. The results of a load experiment are shown in figure 6.3. The figure shows the vertical displacement of both sides of the track as a function of lifting and lowering of the freight car respectively.

It is remarkable that there is a big difference between the two sides of the track. One side has a maximum vertical displacement of 1 mm, while the other side moves only 0.2 mm. If the experiment was made with equal load on each wheel, the difference must be due to the substructure; but we cannot exclude the possibility that the difference is caused by the wheel load being not as expected.

Figure 6.3 shows two hystereses. The curves for unloading lie above the curves for loading. However, we use a mean value in the following evaluation. For a wheel load over 2 tons we find a fairly linear relation between the loading/unloading and the vertical deflection.

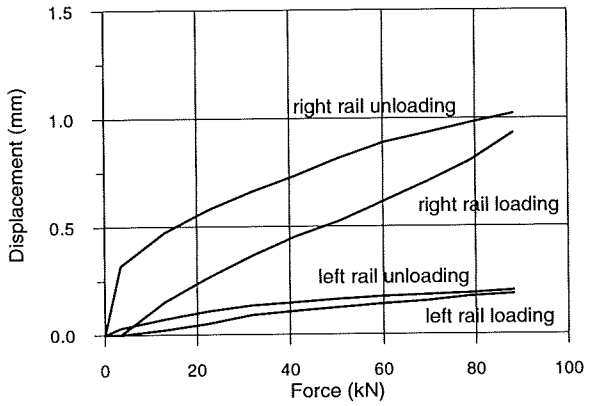

Figure 6.3: The vertical displacement as a function of the forcing.

6.2 Measurements with a passing train

Besides measurements using a static load we have measured the deformation of a track when a train passes.

In connection with trials of the running characteristics of DSB's new ER-train the measuring group in DSB Consult has measured the flexibility of a track. The measurements were carried out in June 1994 near Viby (Sjælland) station in the direction towards Roskilde. The track is a main line built with twin-block sleepers and UIC60 rails.

The selected cross section (km 42,159) is in a curve. Using results from the track recording car, Matissa MVP8 the radius of the curve was found to be 2300 m and the cant to be 24 mm. The cross section was chosen on the basis of the track measurering car recordings showing large track irregularities near the section. Therefore we expect to see dynamic of both quasi-static forcing and forcing by track irregularities.

Measurements using strain gauges and displacement transducers were made when different types of trains (ER, IC3, EA etc) passed with different speeds. Here we concentrate on the displacement measurements. These give us an idea of the motion of the track but not the spring characteristics, because the force acting on the track is unknown.

The position of the five displacement transducers is shown in figure 6.4. There were displacement transducers only on the right side of the track measured in the direction of travel (towards Roskilde).

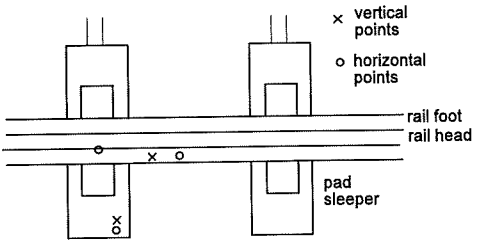

Figure 6.4: The measuring points.

6.2.1 The test results

When a train passed the passing of each wheelset was reflected on the displacement transducers. This picture was more characteristic for the vertical than the lateral measurements. Between two wheelsets in a bogie there was a certain displacement, while there was no displacement between two bogies.

The measurements show that an increasing speed results in increasing displacements in both lateral and vertical directions. This indicates that the dynamics of the passing train increases with increasing speed. Lateral accelerations measured for some of the trains confirm the lateral results. In the vertical direction our results contradict what investigations in Sweden

have shown, [Hammarlund, 1994]. The experiments discussed in [Hammarlund, 1994] were made on a newly built straight track and showed that the vertical forces and accelerations of the track did not increase essentially with increasing speed of a passing X2000-train. The difference between our results and Hammerlund et al's results can possibly be due to the large irregularities on our track.

Another tendency is for the displacements measured on the foot of the rail to be smaller than the displacements measured on the sleeper. This was found for both the lateral and the vertical case. The result is remarkable but can be explained in the measuring points on the foot and on the sleeper not being exactly at the same cross section or in a rolling of the sleeper block. The sleeper block can roll if the support on the left side of the block is more solid than the right side. If this is the case then we can expect a wider gauge than the nominal at the cross section measured. Applying results from the track recording car we find in fact that this is the case.

6.2.1.1 The lateral measurements

An example of the lateral measurements is shown in figure 6.5.

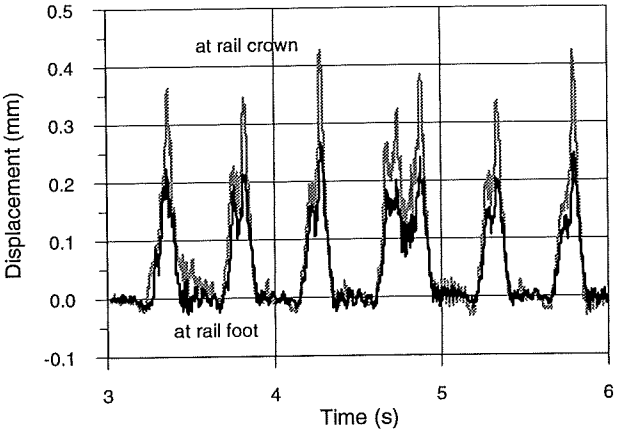

Figure 6.5: The displacement of the foot and the crown of the rails when an IC3-train passes by with 140 km/h.

The figure shows the lateral displacement of the rail foot and rail head when an IC3-train passes at 140 km/h. Six bogies can be seen in the figure. We find both a motion of the head and the foot of the rail. Two wheelsets on a bogie give rise to approximately the same displacement of the rail foot, while the motions of the rail head are different.

The reason why the displacement is larger when the rear wheelset in a bogie passes compared to the front, could be that either the lateral contact force is bigger for the rear wheelset, or the rail already is displaced when the rear wheelset passes. The difference in displacement for two wheelsets on the same bogie becomes more characteristic as the speed increases.

The displacement of the crown of the rail compared to the foot is most likely due to a bend of the rail web. But another explanation could be that the displacements not is measured exactly at the same cross section, and the force therefore not is the same in the two cases.

Figure 6.5 shows that the displacement of the rail foot in average is 0.2 mm for each bogie. If the IC3 has a speed of 50 km/h the measurements give an average value of 0.13 mm, while a speed of 200 km/h gives 0.5 mm. For all speeds and vehicles, we find a maximum difference between the displacement of the rail crown and foot of 0.2 mm.

6.2.1.2 The vertical measurements

In figure 6.6 a vertical measurement of the motion of the rail foot, when an IC3 train passes at 50 km/h, is shown. At this speed we expect little vertical dynamics in the train. In the figure we see that the rear wheelset in a bogie gives rise to bigger displacements of the rail than the front wheelset in the bogie. Because the IC3 train is symmetrical this result could be due to dynamics in the train or to an initial displacement of the rail when the rear axle passes.

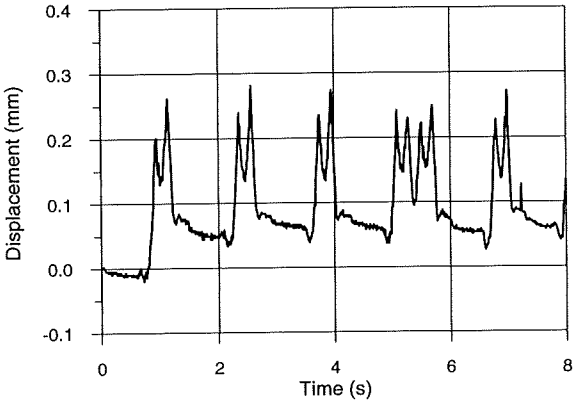

Figure 6.6: The vertical displacement of the rail when a train passes by.

6.3 Evaluation

The track forces were not found in the dynamic experiment, and in the static experiment we found a varied picture of the behaviour of the track. Hereby, the experiments have not yielded a well-defined stiffness for the flexibility of the track.

The test load experiment has shown how big a dispersion there can be on the same track:

Let us consider the track to be a mass supported by a simple spring. Using the test load experiment we can calculate a vertical stiffness, $c_{track,z}$, for the whole flexibility of the track:

- right rail $c_{track,z} \approx 80$ kN / 0.89 mm $\approx$ 90 MN/m
- left rail $c_{track,z} \approx 80$ kN / 0.18 mm $\approx$ 450 MN/m

As a comparison British Rail research use in their simulation program, VAMPIRE a default value of a vertical stiffness of 100 MN/m, [Eickhoff, 1993].

If we instead consider the rail to be a continuously supported beam, the continuous support can be defined by a so-called rail support parameter, $c_{ballast,z}$. The rail support parameter can be calculated from the static test load experiment. A method for doing this is described in [Kerr, 1987]. The method considers the load from several axles. Using the test load experiment the vertical displacement of the rail under one wheel, z_{rail} is determined by

$$z_{rail} = \frac{P\beta}{2c_{ballast,z}}(1 + e^{-\beta l}(\cos\beta l + \sin\beta l)) , \qquad (6.1)$$

where

$$\beta = \sqrt[4]{\frac{c_{ballast,z}}{4EI_{rail,y}}} . \qquad (6.2)$$

l is the distance between the axles of the freight car (6 m), E is the modulus of elasticity of the rail and $I_{rail,y}$ is the moment of inertia about the lateral axis of the rail (UIC60 rail: $I_{rail,y} = 28.63 \cdot 10^{-6}$ m^4). P is the wheel load.

Applying 6.1, we can by an iterative procedure compute the rail support parameter to be:

- right rail $c_{ballast,z} \approx 55$ MN/m^2
- left rail $c_{ballast,z} \approx 470$ MN/m^2

In [Esveld, 1989] it is stated that the rail support parameter usually lies in the interval from 9 MN/m^2 for a poor track quality to 90 MN/m^2 for a good track quality.

The relation between the ballast support parameter, $c_{ballast,z}$ and the support of a simple mass, $c_{track,z}$ can be found if we neglect the influence of the load from several axles:

$$c_{track,z} = \sqrt[4]{c_{ballast,z}^{3} 64\, E I_{rail,y}} \,. \tag{6.3}$$

The values given by Esveld can then be used as an estimate of the support of the simple mass, 20 MN/m < $c_{track,z}$ < 130 MN/m.

From these considerations the vertical displacement of the left rail as evaluated is unusually small. Which means either the ballast was extremely hard or the determination of the wheel load was wrong in the test load experiment. The displacement measured of the right rail must be said to be usual.

The dynamic experiment indicates how the track moves when a train passes. Contrary to the static experiment we find that the lateral motion consists both of a motion of the rail foot and a distortion of the crown about the foot. If in the test load experiment we consider Prud'homme's criteria, [Prud'homme, 1967] we find that for a lateral force up to 25 kN we are far from a permanent shift of the track. For the static case this could be the reason why the rail foot does not move.

In both measurements the distortion of the rail web is found to be maximum 1.5 mrad. To study the influence of the distortion on the geometrical parameters we calculate the geometry for a change in inclination of 2 mrad with regard to 1/20 or 1/40.

Figure 6.7 displays the difference in the rolling radius between a UIC60 rail inclined at 1/40 = 25 mrad and inclined at 23 mrad. The maximum difference is found to be 1.2 mm near the contact with the flange. Compared to the rolling radius with a nominal value of 0.475 m, we conclude that a change in inclination of 2 mrad does not have any essential influence on the geometrical parameters.

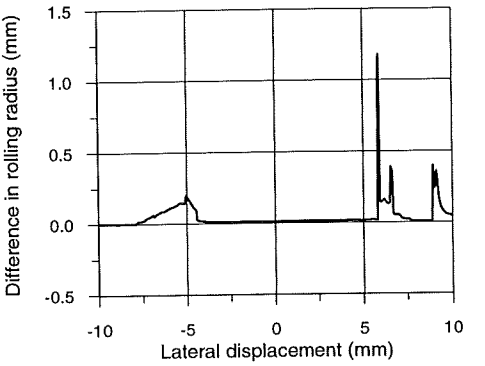

Figure 6.7: The difference in the rolling radius of right wheel between a UIC60 rail inclined 25 mrad and 23 mrad.

For a passing train the track irregularities will cause some oscillations and hereby accelerations in the car. Because of this we cannot use the centrifugal acceleration together with gravity as an estimate of the lateral force acting in the cross section measured. Studying the results from test runs with IC3 made by DB-Minden, [DB-Minden, 1991] we find an indication that an estimate of the total lateral contact force on a bogie can be calculated from the lateral accelerations on the car body, the yaw accelerations on the car body and the lateral accelerations on the bogie. DB-Minden measured both the wheel-rail contact forces and the accelerations.

Let us assume that the twin block sleeper moves as one rigid body laterally and that the average lateral displacement of the rail foot is due to the total lateral contact force from one bogie. We can then compute a lateral stiffness, $c_{track,y}$, for the lateral displacement of the whole track. For an IC3-train running at 200 km/h accelerations in the train were measured. From these accelerations we calculate the lateral contact force on each axle to be 8 kN at the cross section measured. Thus we find

- $c_{track,y} \approx 8 \text{ kN} / 0.5 \text{ mm} = 16 \text{ MN/m}$.

The default value used in the simulation program VAMPIRE is 25 MN/m,

[Eickhoff, 1993].

Because the twin-block sleeper does not move as one rigid body in the vertical direction, the wheel load and not the axle load is essential for the vertical displacement of the rail. Although we know the weight of the train and assume the vertical dynamics to be negligible, we cannot calculate the wheel load, because the points of contact are unknown. We cannot therefore calculate a vertical stiffness for the track in the dynamic case.

Comparing dynamic measurements of the vertical and lateral displacements we find that the magnitude of the displacements is almost the same. Because the vertical forces are assumed to be bigger than the lateral forces, the measurements indicate that the track is more stiff in the vertical than in the lateral direction.

In the measurements we have considered the track as one element and not discussed the flexibility of the individual elements as the pad and substructure. The values are therefore not directly comparable with the one given in [Knothe, 1993].

Chapter 7

Simulations using a flexible track

When modelling the flexibility of a track the system can be considered from different points of view. If you are interested in the dynamics of the track itself you must consider one or more elements in the track to be elastic bodies, for example by using finite element methods. On the other hand if you (as we) are interested in the dynamics of a vehicle on a flexible track, the track can be considered more simply.

The dynamics of a track have been studied throughout the world. For a detailed description we refer to [Knothe, 1993], which is a general article on work done on modelling track. Table 7.1 shows a table from [Knothe, 1993] listing which frequency domains a model must include to describe the different problems that arise in railway technology.

Table 7.1: General problems with vehicle-track interaction (from [Knothe, 1993]).

Problem	Frequency (Hz)
Railway dynamics	0 - 20
Bogie and unsprung mass, e.g. fatigue of axles	0 - 500
Irregularities on the surface of wheel or rail, e.g. corrugation	0 - 1500
Track components, e.g. fatigue of rail in bending	0 - 1500
Wheel-rail noise	0 - 5000
Structure-borne noise and vibration	0 - 500

An example of an elastic model of both rails and sleepers can be found in [Nielsen, 1993]. Among other things such a model can compute, are the bending stresses in the sleepers, for example when the rails are corrugated. Because a simple model of a bogie is used, the model is not very suitable for describing the dynamics of the bogie.

We are mainly interested in studying the dynamics of a vehicle, so our model of the track should be valid for a low frequency domain. For this we can use a simple model of the track, for example just a single body following each wheelset.

7.1 Simple model of the track

In this section we consider the track as a rigid body following a wheelset. The track can move as a whole in the lateral and vertical directions, and will hereby obtain a lateral degree of freedom, y_{track} and a vertical degree of freedom, z_{track}. The model of the track is shown in figure 7.1.

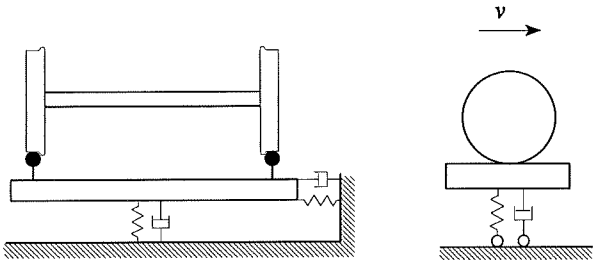

Figure 7.1: A simple model of the track.

Our measurements of the flexibility of the track have shown that the torsion of the railhead about the foot is small. We found that a small torsion has a scant influence on the geometrical parameters and consequently on the dynamics of the vehicle. Therefore we neglect the torsion of a rail. Because we only consider situations where the support is the same at right and left side, also the roll of the track is neglected. We notice that the motion of right and left rail is the same in the model.

According to [Berg, 1994] the parameters used in a single body model of the track can be chosen in such a way that they bear a relation to beam models of the rails. The way to do this is to introduce a shape function following each wheelset. An example given in [Berg, 1994] shows that the calculated generalized parameters have a bigger value than the given values themselves. Because the uncertainty around the given values is large, we have decided not to use a similar point of view.

To determine the equivalent mass of the track is difficult, if not impossible. On a rough estimate the value is estimated to be $m_{track} \approx 500$ kg (a section of two rails, sleeper and ballast).

The measurements described in chapter 6 have not resulted in an unambiguous value for a stiffness of the track in a lateral or vertical direction. For a track model as ours [Eickhoff, 1993] suggests a stiffness of $c_{track,y} = 25$ MN/m in the lateral direction and $c_{track,z} = 100$ MN/m in the vertical direction, while [DFVLR] suggests $c_{track,y} = 20$ MN/m and $c_{track,z} = 40$ MN/m. As calculated in paragraph 6.3 the value given in [Esveld, 1989] can be transformed to 20 MN/m $< c_{track,z} <$ 130 MN/m. Using this as well as the measurements we know the order of magnitude of the stiffnesses.

We derive the equations of motion of the track by using Newton's second law

$$\begin{aligned} m_{track}\ddot{y}_{track} &= c_{track,y}y_{track} + k_{track,y}\dot{y}_{track} - F_{contact,y}\,, \\ m_{track}\ddot{z}_{track} &= c_{track,z}z_{track} + k_{track,z}\dot{z}_{track} - F_{contact,z}\,, \end{aligned} \tag{7.1}$$

where the values of damping $k_{track,y}$ and $k_{track,z}$ are chosen as the percentage of the critical damping, which ensures the track follows the motion of a wheelset.

For a model of a vehicle we use the model of a single-axle bogie described in chapter 5.

7.1.1 Comparison with rigid track

To find the influence of a flexible track on the dynamics of the bogie we first calculate a bifurcation diagram similar to the one with the rigid track in paragraph 5.2. The bifurcation diagram displaying the maximum lateral displacement of the wheelset against the vehicle speed is shown in figure 7.2. In the figure the rails are UIC60 rails inclined at 1/20. For the track flexibility, a lateral stiffness of 20 MN/m and a vertical stiffness of 60 MN/m are used.

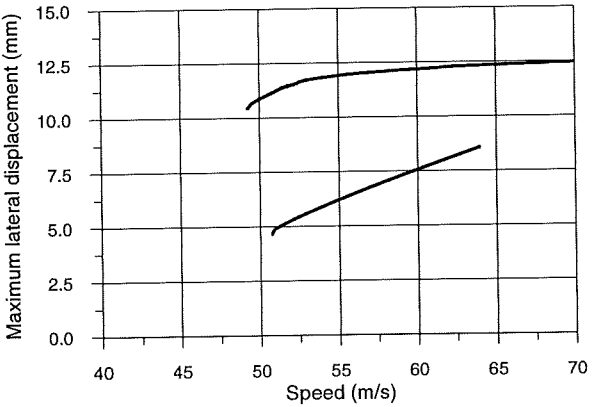

Figure 7.2: Bifurcation diagram showing the maximum lateral displacement of the wheelset against vehicle speed. The bogie is running on flexible track with $c_{track,y}$ = 20 MN/m and $c_{track,z}$ = 60 MN/m.

A periodic solution with flange contact exists at $V = 70$ m/s. For decreasing speed this solution vanishes in a saddle-node bifurcation at $V \approx 49.3$ m/s. Another periodic solution exists in the interval of speed 50.8 m/s $< V <$ 64 m/s.

Comparing with the figure for the rigid track in paragraph 5.2 we find that

the lateral displacement of the wheelset is bigger in figure 7.2. This is due to the motion of the track. Considering the lateral displacement of the track the difference in amplitude of wheelset displacements is found to be the lateral displacement of the track. Furthermore, we find that for the flexible track the solution with flange contact does not symmetry-break at high speed. Other wise the same solutions are found.

For the rigid track the linear critical speed is computed to be 62.8 m/s and the nonlinear critical speed to be 48 m/s, while the linear critical speed for the flexible track is 62.6 m/s and the nonlinear critical speed is 49.3 m/s. We have found that there is a small but unimportant difference in the critical speeds.

7.1.2 Critical speeds

In the following we use the simple track model to investigate the dependence of the flexibility of the track on the linear and nonlinear critical speed. When the bogie is running on a straight perfect but flexible track consisting of UIC60 rails inclined at 1/20 or 1/40 we vary

- the lateral flexibility of track
- the vertical flexibility of track
- the coefficient of adhesion

to hereby calculate the stability of the bogie in a two parameter space.

7.1.2.1 Critical speeds as a function of the lateral flexibility of the track

In the above investigations we have found that the critical speeds between a certain flexible track and a rigid track are almost the same. However if the flexibility has an influence we expect it to be lateral. One reason to an expected influence is that the nonlinear critical speed is determined by a saddle-node of a solution with flange contact.

Figure 7.3 and 7.4 show the critical speeds as a function of the lateral flexibility of the track. Figure 7.3 is computed for the bogie running on rails with an inclination of 1/20, while figure 7.4 is for the inclination 1/40.

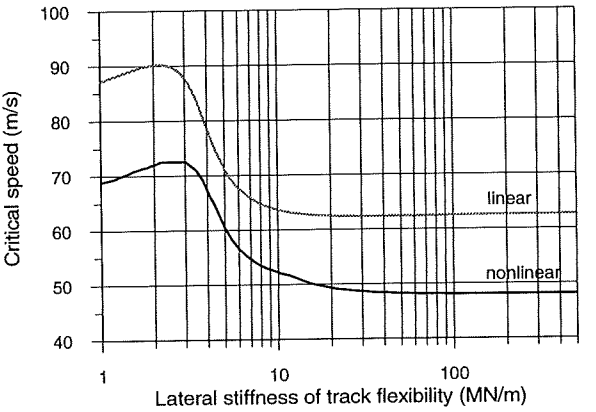

Figure 7.3: The linear and nonlinear critical speed as a function of the lateral flexibility of the track in a logarithmic scale. The rails are UIC60 rails inclined 1/20 and $c_{track,z}$ = 60 MN/m.

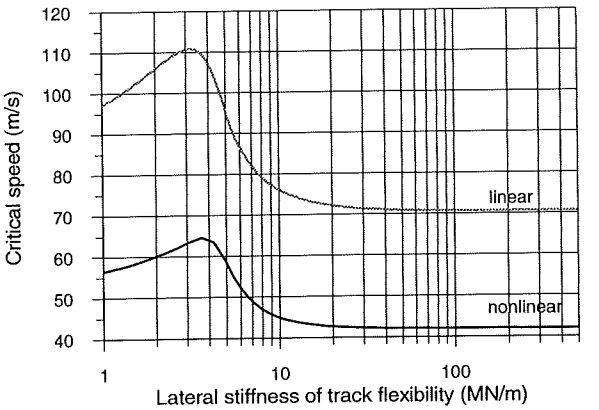

Figure 7.4: The linear and nonlinear critical speed as a function of the lateral flexibility of the track in a logarithmic scale. The rails are UIC60 rails inclined 1/40 and $c_{track,z}$ = 60 MN/m.

Comparing the two figures we find that even though the linear critical speed is higher for an inclination of 1/40 than 1/20 the nonlinear critical speed is lower.

The figures illustrate that the linear and nonlinear critical speeds show the same variation as a function of the lateral track stiffness. Stiff springs will not cause a change in the critical velocities. As the spring becomes softer the critical speeds will change. The largest critical speed is found for a stiffness around 3 MN/m.

In [Ostermeyer], where the rails are modelled as Euler-Bernoulli beams on a Winkler foundation, similar results are found. Using linear computations Ostermeyer determines the linear critical speed of a two-axle bogie as a function of the lateral flexibility of the foundation. The same variations as in figure 7.3 and 7.4 are found. For very high flexibility (not examined here) Ostermeyer finds big variations in the linear critical speed.

In reality the track is rather stiff. When we consider realistic values for the track stiffness, the calculations show that the flexibility of the track in the lateral direction has little influence on the critical speeds.

7.1.2.2 Critical speeds as a function of the vertical flexibility of the track

In investigations of the dynamics of a railway vehicle it is often assumed that the coupling between the horizontal and vertical motions can be neglected. Therefore we expect the vertical flexibility of the track to have little influence on the critical speeds.

A calculation of the critical speeds as a function of the vertical stiffness of a track inclined at 1/20 is shown in figure 7.5. As expected we find no variation at all. A similar result is found for a track inclination of 1/40.

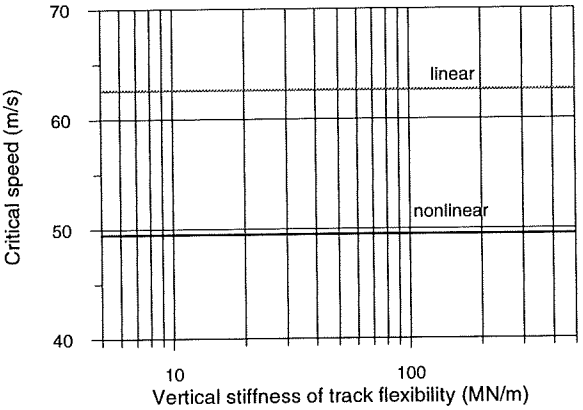

Figure 7.5: The linear and nonlinear critical speed as a function of the vertical flexibility of the track in a logaritmic scale. The rails are UIC60 rails inclined at 1/20 and $c_{track,y}$ = 20 MN/m.

7.1.2.3 Critical speeds as a function of the coefficient of adhesion

When a vehicle is running on a track it is seldom that the coefficient of adhesion between wheel and rail is known. On the other hand, the coefficient of adhesion will vary as the train moves on the railway line. This is for example due to weather conditions. Consequently, it seems relevant to investigate the dynamics of the vehicle for different coefficients of adhesion. According to [Garg, 1986] typical values lie in the interval from 0.1 for wet conditions to 0.4 for dry conditions, while [Eickhoff, 1993] describes a value between 0.3 and 0.4 to be the most common. (With wet leaves on the rails in autumn the coefficient of adhesion may be even lower than 0.1).

The linear and nonlinear critical speeds as a function of the coefficient of adhesion are shown in figure 7.6 and 7.7. Figure 7.6 is for a rail inclination of 1/20 and figure 7.7 is for a rail inclination of 1/40. Two different lateral stiffnesses of the track are examined: $c_{track,y}$ = 20 MN/m and $c_{track,y}$ = 40 MN/m.

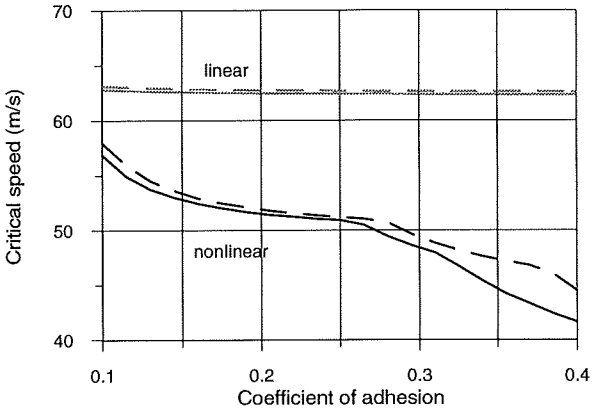

Figure 7.6: The critical speeds as a function of the coefficient of adhesion. The rails are UIC 60 rails inclined at 1/20 and $c_{track,z}$ = 60 MN/m. The solid line is for $c_{track,y}$ = 40 MN/m and the dotted line for $c_{track,y}$ = 20 MN/m.

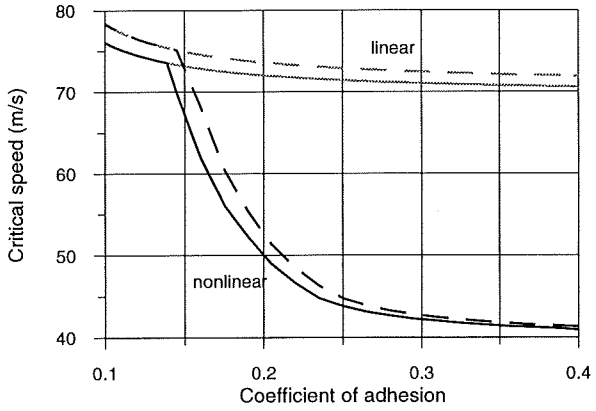

Figure 7.7: The critical speeds as a function of the coefficient of adhesion. The rails are UIC 60 rails inclined at 1/40 and $c_{track,z}$ = 60 MN/m. The solid line is for $c_{track,y}$ = 40 MN/m and the dotted line for $c_{track,y}$ = 20 MN/m.

As the adhesion coefficient varies the linear critical speed remains approximately the same, while the nonlinear critical speed changes. The nonlinear critical speed decreases for increasing coefficient of adhesion. The two different lateral track stiffnesses show almost the same variation. However there is a deviation between the nonlinear critical speeds for the inclination of 1/20 and a coefficient of adhesion between 0.3 and 0.4.

In figure 7.6 we see a sudden change in the curve for the nonlinear critical speed around a coefficient of adhesion of 0.28. This bend is due to the nonlinear critical speed changing from being a saddle-node bifurcation of a solution without flange contact to a saddle-node of a solution with flange contact, as the coefficient of adhesion increases.

Considering the rail inclination of 1/40 we find that the type of bifurcation of the stationary solution changes with the coefficient of adhesion. For small coefficients of adhesion the loss is through a supercritical Hopf-bifurcation, so the linear and nonlinear critical speeds are the same and the the amplitude of the oscillation grows continuously with the speed. For larger coefficients of adhesion the stationary solution undergoes a subcritical Hopf-bifurcation with jump to an oscillating solution.

Comparing the figures we find that except for small values of the coefficient of adhesion the inclination of 1/40 gives rise to the lowest nonlinear critical speed.

The tendency of a decreasing nonlinear critical speed for an increasing coefficient of adhesion is also illustrated by [Jensen, 1995]. Jensen has found that this is the case for a model of a bogie on the Danish IC3 train and four different track configurations.

7.1.3 Summary

Using a simple model of the track, investigations of the dynamics of a single-axle bogie have shown that changes in the elasticity of the track are not important for the stability of the bogie. The vertical elasticity of the track will not have any influence at all, while a soft stiffness for the lateral elasticity will increase the critical speeds.

Making the comparison with the bogie running on a rigid track we have shown that the critical speeds and the scenario of solutions are almost the same for a rigid and a flexible track. Looking instead at the amplitudes of the displacement of the wheelset the only difference is that for a flexible track the displacement of the track is added to the displacement of the wheelset. Another example of this result can be found in [Jensen, 1994].

For the two track configurations we have seen that the bogie running on rails with an inclination of 1/40 generally have a lower nonlinear critical speed than running on rails inclined at 1/20. This is in contrast to the results from the linear analysis.

7.2 The rails modelled as Euler-Bernoulli beams

We have found that some of the nonlinear critical speeds are saddle-node bifurcations of solutions with flange contact. For a solution with flange contact we obtain an impact force between wheel and rail indicating the contact with the flange.

As an approach to analysing how the track moves when affected by such a force we consider the rails as discretely supported Euler-Bernoulli beams. Inspired by [Zhai, 1993] we model the track as two Euler-Bernoulli beams which are discretely supported by sleepers. The sleepers are assumed to be rigid bodies supported by the ballast. Contrary to Zhai and Sun, who include the interaction of the ballast, we model the ballast as an elasticity underneath each sleeper.

The model can be lateral or vertical. This means that the rails and sleepers can either move laterally or they can move vertically. We use the same type of model in the two cases. A drawing of the vertical model of one rail is shown in figure 7.8.

The correctness of an Euler-Bernoulli simplification of the rails is dependent on the bending stiffness of the rails. Because the bending stiffness against a lateral motion is smaller than against a vertical motion, the Euler-Bernoulli

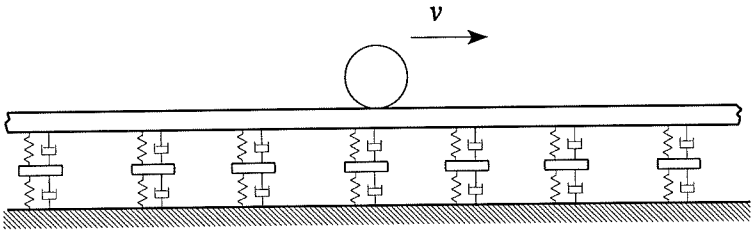

Figure 7.8: A rail as a discretely supported beam.

simplification is more correct in the vertical than the lateral case.

In the lateral case the rail web will obtain a distorsion due to that the contact force does not pass through the shear center of the rail. According to [Grassie, 1992] this distortion is significant at higher frequencies. At lower frequencies [Ripke, 1991] illustrates that the web will bend, but the crown and the foot will move in phase. In [Thomson, 1995] it is described that omitting the torsional effects in a rail underpredict the lateral accelerations.

From the measurements described in chapter 6 we found that the main lateral motion of the rail when the first axle of a bogie passes by was a translational motion and not a distortion. However a distortion was found when the rear axle of the bogie passes by.

For simplification we neglect the distorsion of the rail web. Consequently we model the minimum motion of the rail crown. We can say that the model is a first approach to an elastic discretely supported model of the rails treated independently and combined by the sleepers. Laterally the model describes not the nature of the motion of the rail itselves.

The lateral or vertical motion of the right or left rail, u is determined by the partial differential equation

$$EI_{rail}\frac{\partial^4 u}{\partial x^4} + m_{rail}\frac{\partial^2 u}{\partial t^2} = -\sum_{i=1}^{N_{sleeper}} F_{sleeper}\delta(x - x_i) - \sum_{j=1}^{N_{wheelset}} F_{contact}\delta(x - x_j) , \quad (7.2)$$

where E is the modulus of elasticity of the rail, I_{rail} is the moment of inertia about the vertical or lateral axis and m_{rail} is the mass of the rail per meter. $\delta(x)$ is Dirac's delta function. The number of sleepers is $N_{sleeper}$ and the position of the sleepers in the longitudinal direction is x_i. The force from each sleeper is

$$F_{sleeper}(t) = c_{pad}(u(x_i,t) - u_{sleeper}(t)) + k_{pad}(\dot{u}(x_i,t) - \dot{u}_{sleeper}(t)) , \quad (7.3)$$

where $u_{sleeper}$ is the lateral or vertical motion of the sleeper, c_{pad} and k_{pad} are the stiffness and damping of the pad, respectively. The number of wheelsets is $N_{wheelset}$ and the position of the wheelsets in the longitudinal direction is x_j. The contact force from each wheel in the lateral or vertical direction is $F_{contact}$.

Using the method of separation 7.2 can be solved. The calculations are given in appendix D. For the motion of each rail we obtain

$$u = \sum_{n=1}^{N} P_n(x)q_n(t) , \quad (7.4)$$

where p_n is the rail mode function

$$p_n(x) = \sqrt{\frac{2}{m_{rail}L}}\sin\frac{n\pi x}{L} , \quad (7.5)$$

and q_n is defined by a time dependent differential equation

$$\ddot{q}_n(t) + \frac{EI_{rail}}{m_{rail}}\left(\frac{n\pi}{L}\right)^4 q_n(t) = -\sum_{i=1}^{N_{sleeper}} F_{sleeper}p_n(x_i) - \sum_{j=1}^{N_{wheelset}} F_{contact}p_n(x_j) . \quad (7.6)$$

L is the length of track considered. N is the mode number.

Because the sleepers are assumed to be rigid, the equation of motion for each sleeper becomes

$$m_{sleeper}\ddot{u}_{sleeper} = F_{sleeper,r} + F_{sleeper,l} - c_{ballast}u_{sleeper} - k_{ballast}\dot{u}_{sleeper}, \qquad (7.7)$$

where $m_{sleeper}$ is the mass of a sleeper. $c_{ballast}$ and $k_{ballast}$ describe the flexibility of the ballast. In the vertical case the roll of the sleepers is neglected.

7.2.1 Simulations

In a later chapter we use the model in the vertical case. Here we consider the lateral flexibility of the track to analyse its influense on the motion on a bogie. Both the motion of right rail, $y_{rail,r}$ and left rail, $y_{rail,l}$ are determined by equation 7.2.

When using such a model of the track, the problem is that a long track will give a large number of differential equations. In our simulations we use a length of 125 m and a mode number of 200. To describe the motion of the track we then need a system consisting of 600 second order nonlinear differential equations.

The rails are assumed to be UIC60 rails inclined at 1/20 (m_{rail} = 60 kg, $I_{rail,z}$ = 5.41 · 10^{-6} m^4). The distance between the sleepers is 0.625 m. For the elasticity of the pad we use values inspired by the one given in [Ripke, 1991]. The lateral stiffness of the ballast is chosen as 40 MN/m.

The vehicle is the single-axle bogie, which is modelled in chapter 5.

A time simulation for the bogie running at 50 m/s is shown in figure 7.9. The figure displays the lateral motion of left and right rail at the position of the wheelset for an oscillation where the wheelset hunts and flange contact occurs. From the figure we find that there is a difference between the displacements of the two rails. The difference occurs at flange contact. This indicates that the meeting of the flange will move only the rail it strikes and not the whole track structure.

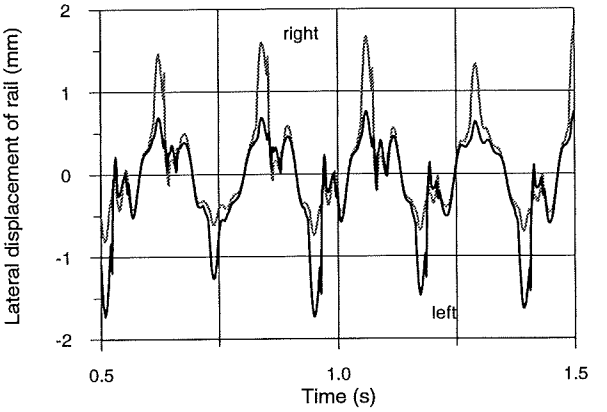

Figure 7.9: The lateral displacement of the right and left rail when the wheelset having flange contact. The rails are modelled as Euler-Bernoulli beams.

This large motion of the rail compared to the sleeper could mean that neglecting distorsion of the rail web may be too inaccurate and consequently a more complex model is needed to simulate the lateral dynamics of the rails when affected by the flange. However the simulation illustrates some kind of a minimum expected motion of the crown.

7.2.2 Comparison with simple model

If instead we use the simple track model from the previous paragraph, we find the motion of the track to be as plotted in figure 7.10. Even though we have no direct connection between the track stiffness for the simple model and the stiffness of the ballast in the beam model we choose the same value. So the lateral track stiffness is 40 MN/m in figure 7.10.

Comparing figure 7.9 and 7.10 we find that some higher frequency oscillations are smoothened out using the simple model. The displacement of the rail under the wheel with flange contact is almost the same, but for the rail at the wheel without flange contact the situation is different.

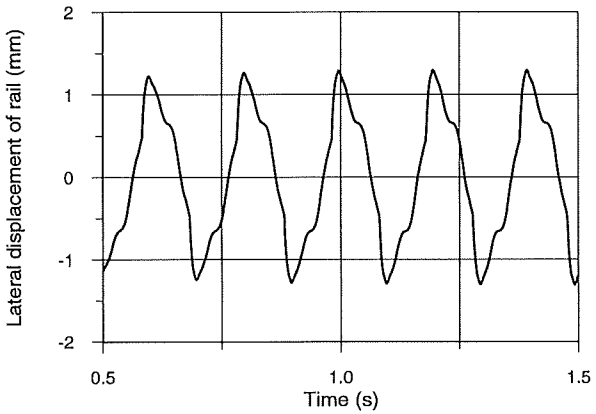

Figure 7.10: The lateral displacement of the rails when the wheelset having flange contact. The simple track model is used.

Considering the motion of the track the models display different dynamics. Because the motion of the two rails are the same in the simple model, figure 7.10 does not reflect the independent motion of the rails. If we assume figure 7.10 to show an average of the motion of the two rails plotted on figure 7.9 we find pretty good agreement.

Because it is the contact point at the flange and not the one at the tread that is dominant, we expect the two models to show approximately the same dynamics of the bogie. The lateral displacement of the wheelset using the two models of the track is shown in figure 7.11. Looking at the curve calculated by the beam model we see that it is aperiodic and the amplitude is a little bigger than for the curve calculated by the simple model. However, the biggest difference between the models is to be found in the frequency of the oscillations: 5 Hz using the simple model and 4.3 Hz using the beam model.

When using the two models to simulate the dynamics of a wheelset without flange contact occuring, the two models show almost identical results both for the motion of the bogie and the motion of the track. For such a motion the rails are affected by low frequency forces and there is no need for an elastic

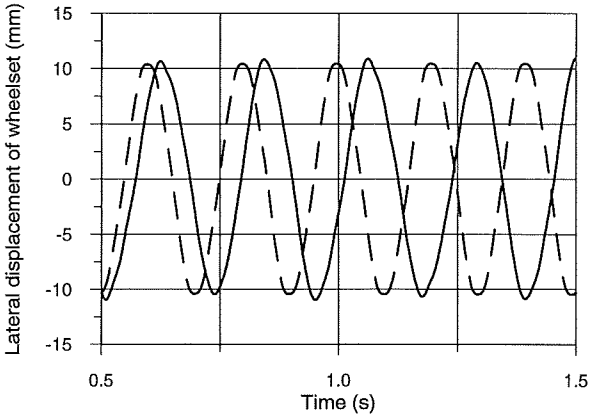

Figure 7.11: The lateral displacement of the wheelset running on a flexible track. The solid line is when the rails are modelled as beams while the simple track model is used for the dotted line.

model. The motion of the two rails is find to be approximatley the same.

Although the comparison between the two models has shown differences in the dynamics of the bogie, we would say that these differences are so small that the calculations in paragraph 7.1 are suitable for giving a picture of the influence of a flexible track on the stability of the bogie. Time simulations for other vehicle speeds support this.

The elastic beam model should be extended to include the distortion of the rail webs. In consequence we do not expect the lateral displacement of the rail head to increase so much and the wheel-rail geometry to change so much that it could have a significant influence on the dynamics.

From a practical point of view this conclusion is preferable because the elastic model is not usable for stability investigations of vehicles. However due to its discreteness the model is useful for investigating the effect on the vehicle of a broken connection between rail and sleeper or a varying support of the sleepers - i.e. transient analyses.

Chapter 8

The test vehicle

To get a full understanding of the steering of the single-axle bogie, it is not enough to model only one bogie. The whole test vehicle must be considered. The test vehicle is shown in figure 8.1. It consists of two S-train cars from DSB built in 1972, on which a bogie on the driving trailer is replaced by the KERF bogie.

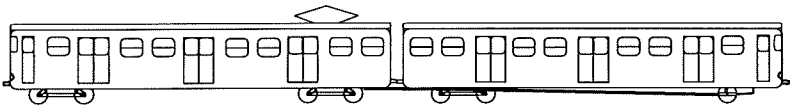

Figure 8.1: The two-car test vehicle.

8.1 The model

A mathematical model of the test vehicle consists of two cars, four bogies and seven wheelsets. The degrees of freedom of the bodies are the same as the one described in chapter 2.

The construction of the three two-axle bogies is similar, but with different masses and moments of inertia. For each wheelset on the two-axle bogies, the primary suspension consists of two springs acting in the three directions of displacement and two vertical dampers. The secondary suspension consists of two springs acting in the three directions of displacement, two vertical dampers and one lateral damper. For the two two-axle bogies on the same car the values of stiffnesses and dampers are the same, while the values are

different for the two-axle bogie on the other car. All the suspensions are linear. For the construction of the single-axle bogie we refer to the description in chapter 5.

The mechanical steering system is built up of a coupling rod between the two cars and two angle rods connected to the single-axle bogie. A drawing is shown in figure 8.2. The idea is that the deflection angle between the two car bodies is used as a passive steering signal. When the front car enters a curve the coupling rod will turn and the two angle rods will yaw, so the wheelset on the single-axle bogie is forced into a suitable position on the curve.

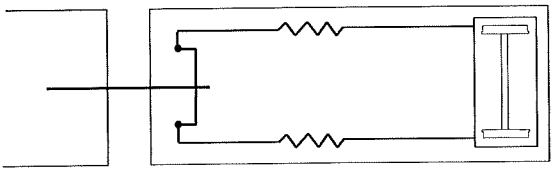

Figure 8.2: The mechanical steering system.

The steering is modelled in such a way that the coupling rod has two degrees of freedom: a lateral motion, y_{coup} and a yaw motion, ψ_{coup}. Each of the angle rods has one degree of freedom describing the yaw motion, ψ_{angle}. The coupling rod is connected to each car by a lateral spring. The angle rods are connected to the coupling rod by lateral springs and to the single-axle bogie by longitudinal springs. The stiffness of these longitudinal springs is in the following called the stiffness of the steering system, $c_{steering}$. The other springs are very stiff.

Furthermore, the angle rods are, at their center of gravity, connected to the car body by links. These links lead to the positions of the center of gravity of the angle rods being the same as the corresponding points on the car body and the forces acting on the angle rods being transfered to the car body. Because the mass of the angle rods is small compared with the mass of the car body, we neglect the accelerations of the angle rods in the transfering

forces.

As an example of a transfering force, the longitudinal spring between an angle rod and the bogie gives, among others, rise to a moment on the car body:

$$M_{link\ car,z} = c_{steering} \Delta r_x d_{car\ angle,y} \ , \tag{8.1}$$

where Δr_x is the relative longitudinal displacement between the point of attack of the spring on the bogie and on the angle rod. $d_{car\ angle,y}$ is the lateral position of the angle rod on the car body.

If we assume the track to be rigid, we obtain a system of 121 first order nonlinear differential equations for describing the motion of the test vehicle. In the following we consider the direction of travel where the single-axle bogie is placed at the front end of the vehicle.

8.2 Comparison with model of the single-axle bogie alone

To investigate whether there is a difference between the results from the model of the whole two-car vehicle and the model of the single-axle bogie alone (chapter 5), we compute a bifurcation diagram of the maximum lateral displacement of the single-axle bogie. The rails are UIC60 rails inclined at 1/20. As $c_{steering}$ we choose the same value as the one used as the longitudinal spring directly to the carbody in the model of only the single-axle bogie. The bifurcation diagram is shown in figure 8.3.

At $V = 70$ m/s there exists a solution with flange contact. The characteristic of this solution has not been studied further. For decreasing speed the solution remains until 51.3 m/s, whereafter it settles down to a low amplitude periodic solution. This low amplitude solution disappears in a saddle-node bifurcation at $V \approx 50.4$ m/s. Increasing the speed the periodicity vanishes at $V \approx 60.5$ m/s and a chaotic motion is developed. A blow up of the chaotic region is given in figure 8.4. The figure shows there is a periodic window in the attractor.

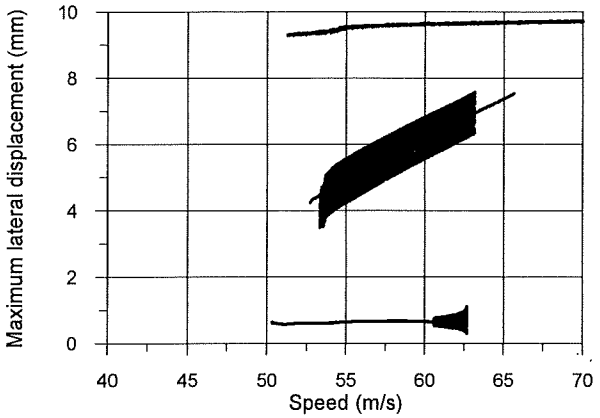

Figure 8.3: Bifurcation diagram showing the maximum lateral displacement of the wheelset on the single-axle bogie against vehicle speed.

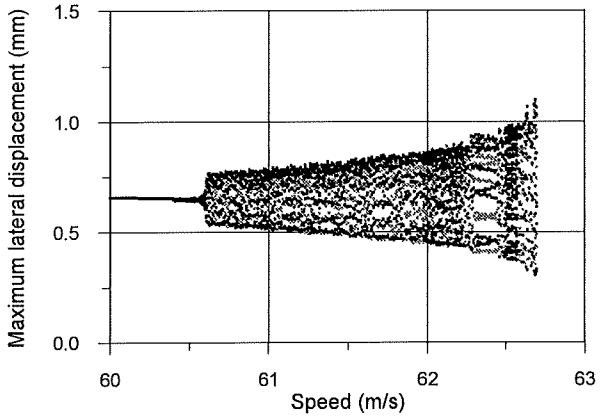

Figure 8.4: Bifurcation diagram showing the maximum lateral displacement of the wheelset on the single-axle bogie against vehicle speed. A magnification of figure 8.3.

Due to the complexity and the size of the dynamical system it has not been possible to analyse the transition to chaos in detailed. Computing a time series immediately after $V = 60.5$ m/s, we find the solution looks like a quasi-periodic solution. This is supported by considering a poincaré section of the maximum lateral displacement of the wheelset on the single-axle bogie against the lateral displacement of the car body. The section illustrates a close curve. However the quasi-periodicity vanishes quickly. At $V = 61$ m/s we compute a largest lyapunov exponent of a trajectory to converge towards 15.7 and we find that the close curve from the poincaré section obtains a width.

Another poincaré section of the chaotic attractor at $V = 61$ m/s is given in figure 8.5. In the figure the maximum lateral displacement of the wheelset on the single-axle bogie is plotted against the yaw motion of the wheelset. The attractor is slightly asymmetric. The figure illustates that there is a bend in the attractor at a lateral displacement of the wheelset just before 0.75 mm. Similar as we found in chapter 5 the bend corresponds to a change in a radius of curvature of the rails. In this case it is the left rail changing in curvature from 300 mm to 80 mm.This means the attractor contains a discontinuity in a parameter which influences the contact ellipse.

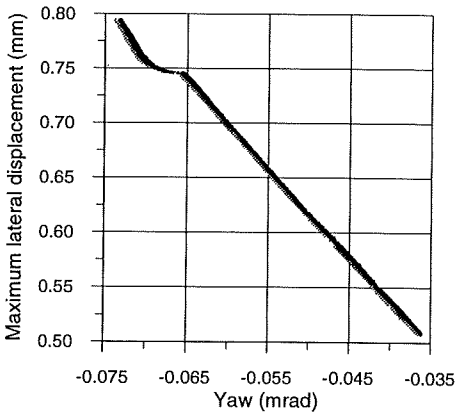

Figure 8.5: Poincaré section displaying the maximum lateral displacement of the wheelset on the single-axle bogie against the yaw of the wheelset for $V = 61$ m/s.

Increasing the speed the chaotic attractor disappears at $V \approx 62.7$ m/s and the trajectory jumps to another chaotic attractor, see figure 8.3. A magnification of a piece of this attractor is given in figure 8.6. The figure illustrates that there is periodic windows in the attractor. The window at $V = 60$ m/s is an asymmetric period six solution. For decreasing speed the attractor vanishes at $V \approx 53.5$ m/s whereafter the trajectory settles down to the low amplitude periodic solution. For increasing speed the attractor vanishes at $V \approx 63.2$ m/s, whereafter the trajectory jumps to the solution with flange contact.

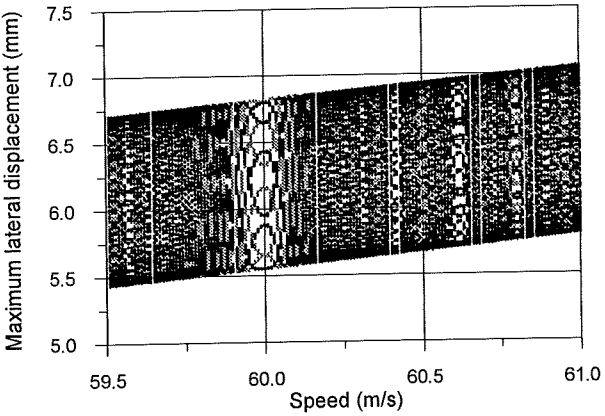

Figure 8.6: Bifurcation diagram showing the maximum lateral displacement of the wheelset on the single-axle bogie against vehicle speed. The figure displays a piece of a chaotic attractor.

From figure 8.3 we see that besides the described solutions there is a periodic solution without flange contact in the interval of speed $52.7 < V < 65.7$ m/s. The amplitude of this solution is so that it will be in the chaotic attractor shown in figure 8.6 (therefore it is not visible at all speed in the figure). Varying the initial conditions we find that the periodic solution is much more attracting than the chaotic solution and consequently that the chaotic solution is very hard to reach.

Comparing with paragraph 5.2 we find that the two models corresponds as regards to the solution with flange contact and the periodic solution with an

amplitude of the wheelset in the interval between 4 mm and 7 mm. The latter exists in a larger interval of speed for the model of the two whole cars. Moreover the model of the two cars yields a low amplitude solution and a chaotic solution. The model predicts a nonlinear critical speed of 50.4 m/s while the model of the bogie alone yields $V_{nonlinear} \approx 48$ m/s.

We hereby conclude that using a model of the whole steering system compared with just using two springs affects the dynamics of the single-axle bogie.

8.3 Stability simulations

In the following we will analyse the stability of the two-car test vehicle in dependence of two parameters:

- the stiffness of the steering system, $c_{steering}$
- the damping coefficient of the yaw dampers on the single-axle bogie,

where the focus will be on the steering system.

8.3.1 Varying steering stiffness

The stiffness of the steering system is an important design parameter. It must ensure the vehicle is stable when running on straight track and the single-axle bogie is steered properly in curves. Therefore we investigate the stability of the vehicle in dependence on the stiffness of the steering system for four different track configurations:

- UIC60 rails with a gauge of 1435 mm and an inclination of 1/20 or 1/40.
- DSB45 rails with a gauge of 1435 mm and an inclination of 1/20 or 1/40.

These track configurations may all be found on the network of Copenhagen.

First we make a linear analysis. The maximum real part of the eigenvalues of the linearized system is calculated for the different track configurations. The calculations indicate two main areas of instability; one for high speeds and low steering stiffnesses and one for low speeds and high steering stiffnesses. Beside this, the area for low speeds and stiffnesses seems to have a low damping rate. The worst track configuration for the stability is the DSB45 rails inclined at 1/20, while the UIC60 rails inclined at 1/40 seems to be the best. This agrees with the determination of the equivalent conicity (see chapter 3). The calculations for these two track configurations are shown in figure 8.7 and 8.8.

Computing the eigenvectors of the system we find that the instability is caused by the single-axle bogie. For low steering stiffnesses and high speeds the mode is a lateral and yaw motion of the single-axle bogie and wheelset. For high steering stiffnesses and low speeds the mode is a lateral and yaw motion of the single-axle bogie and wheelset plus a yaw motion of the front car body.

To illustrate the two different kinds of instability, time series are calculated. Figure 8.9 and 8.10 show the lateral motion of the single-axle bogie and the front car body for two different speeds and stiffnesses.

The curves in figure 8.9 show the hunting motion for high speeds and low stiffnesses. The motion is characterized by a hunting frequency around 6 Hz. The displacements of the bogie are large, but the motion is not transmitted through the secondary suspension to the car body. The curves in figure 8.10 show the car body instability for high steering stiffnesses. These oscillations have a much lower frequency and considerable car body displacements.

The appearance of such two types of instability is well-known in railway dynamics. For a further description we can refer to [Wickens, 1965b].

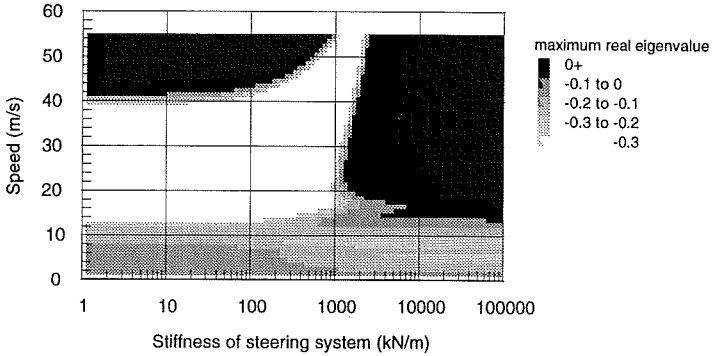

Figure 8.7: The maximum real eigenvalue as function of the stiffness of the steering system (in a logaritmic scale) and the vehicle speed. The track configuration is DSB45 rails inclined at 1/20.

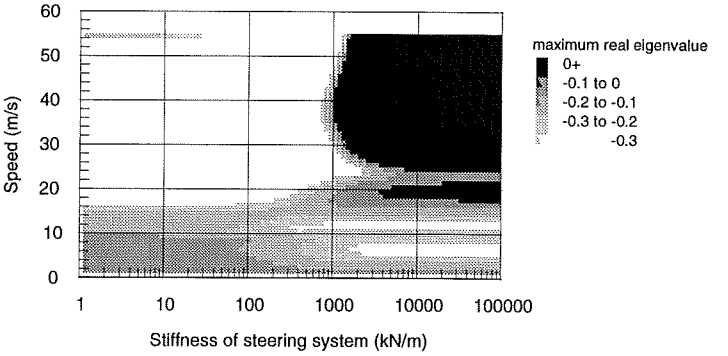

Figure 8.8: The maximum real eigenvalue as function of the stiffness of the steering system (in a logaritmic scale) and the vehicle speed. The track configuration is UIC60 rails inclined at 1/40.

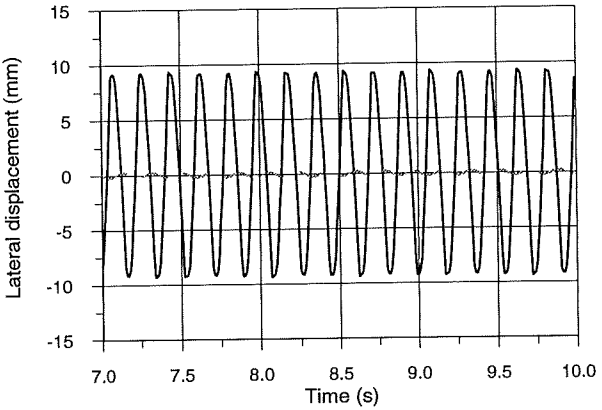

Figure 8.9: A time series of the lateral displacement of the wheelset on the single-axle bogie (solid line) and the car body (dotted line). Computed for a track configuration of DSB45 rails inclined at 1/20, $c_{steering}$ = 100 kN/m, and V = 50 m/s.

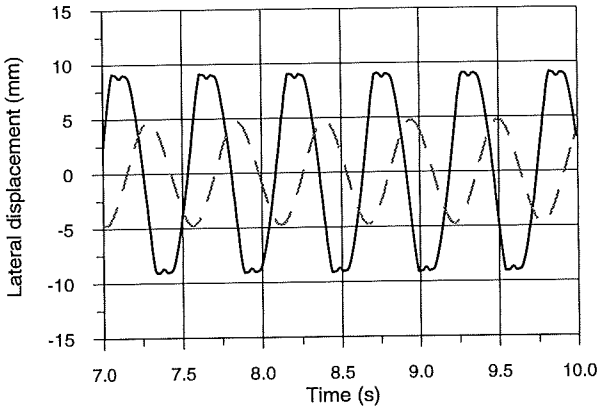

Figure 8.10: A time series of the lateral displacement of the wheelset on the single-axle bogie (solid line) and the car body (dotted line). Computed for a track configuration of DSB45 rails inclined at 1/20, $c_{steering}$ = 10000 kN/m, and V = 30 m/s.

As an approach to a nonlinear analysis, we make a transient analysis. The maximum lateral displacement of the wheelset on the single-axle bogie and the front car body are analysed three seconds after the action of a 4 mm disturbance of the single-axle bogie. The results for the track configurations DSB45 rails inclined at 1/20 and UIC60 rails inclined at 1/40 are shown on figures 8.11 to 8.14. Figure 8.11 and 8.12 show the maximum displacement of the wheelset, while figure 8.13 and 8.14 show the maximum displacement of the car body.

In figure 8.12 we see that the displacement of the wheelset generally will be large with flange contact or small indicating stable run. In figure 8.11 the picture is a little more colourful. Only for a region in the middle, the motion has totally died out. Both types of instability are visible in figure 8.11 and 8.12.

Comparing the wheelset displacement with the linear investigations, we find that the transient analysis indicates that the hunting region will start at lower speeds than found by the linear analysis, i.e. the loss of stability seems to be through a subcritical Hopf-bifurcation. For the region with car body instability and low speeds the instability found by the linear analysis is not clear with regard to the wheelset displacements. This is because an oscillating solution in this region has an amplitude of less than 5 mm. The bogie is unstable, but without flange contact.

The structure of the displacement of the car body is different. As we could expect from figure 8.9, the hunting region is not visible in figure 8.13 and 8.14. On the other hand, the car body instability is easy to see in the figures. The area for low speeds and stiffnesses is noticeable, especially in figure 8.13. Here we find that a disturbance of the wheelset will be transmitted almost undamped to the car body, even though the wheelset displacement is decreasing.

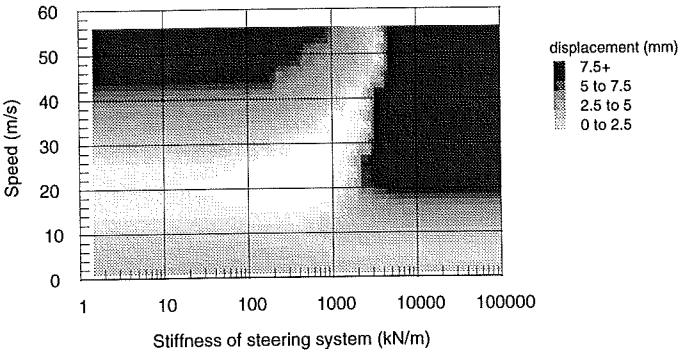

Figure 8.11: The maximum lateral displacement of the wheelset on the single-axle bogie as function of the stiffness of the steering system (in a logaritmic scale) and the vehicle speed. The track configuration is DSB45 rails inclined at 1/20.

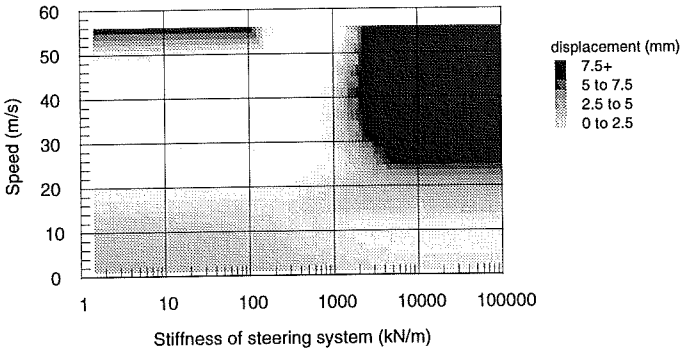

Figure 8.12: The maximum lateral displacement of the wheelset on the single-axle bogie as function of the stiffness of the steering system (in a logaritmic scale) and the vehicle speed. The track configuration is UIC60 rails inclined at 1/40.

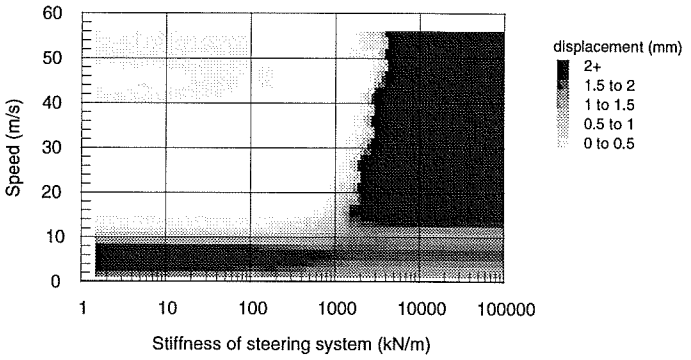

Figure 8.13: The maximum lateral displacement of the front car body as function of the stiffness of the steering system (in a logaritmic scale) and the vehicle speed. The track configuration is DSB45 rails inclined at 1/20.

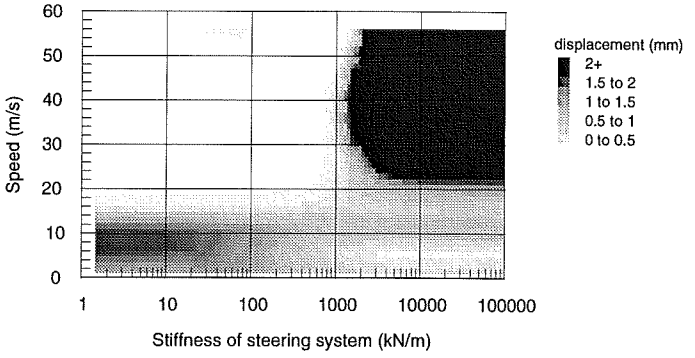

Figure 8.14: The maximum lateral displacement of the front car body as function of the stiffness of the steering system (in a logaritmic scale) and the vehicle speed. The track configuration is UIC60 rails inclined at 1/40.

The transient behaviour of this situation is shown in figure 8.15. The low damped oscillation of the wheelset has a frequency of 0.6 Hz. As a comparison we calculate the kinematic (the Klingel) frequency. The kinematic frequency of the wheelset is given by

$$f = \frac{V}{2\pi}\sqrt{\tan\frac{\lambda_e}{r_0 a_0}}\,, \tag{8.2}$$

where r_0 and a_0 are the rolling radius and the distance between the center of gravity of the wheelset and the contact point when the wheelset is placed in its central position respectively. For the situation shown in figure 8.15 the kinematic frequency is computed to be near 0.6 Hz.

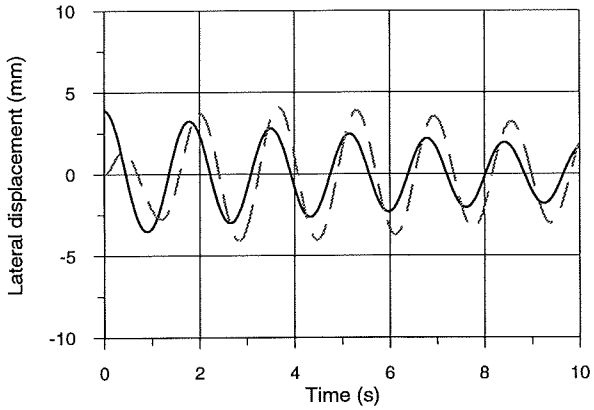

Figure 8.15: A time series of the lateral displacement of the wheelset on the single-axle bogie (solid line) and the car body (dotted line). Computed for a track configuration of DSB45 rails inclined at 1/20, $c_{steering}$ = 10 kN/m, and V = 5 m/s.

Using the same speed and steering stiffness, we calculate the maximum eigenvalue of the stationary solution. This eigenvalue corresponds to a lateral car body oscillation with the same frequency as the one of the oscillation, i.e. the eigenfrequency of the car body and the kinematic frequency are almost the same for low speeds and steering stiffnesses.

From analyses of the vehicle running on the four track configurations, we find an indication that it is possible to choose a steering stiffness so that the vehicle is stable up to at least the maximum operational speed of 120 km/h ≈ 33 m/s. The choice should be a stiffness between 500 kN/m and 1000 kN/m. It has turned out that the worst track configuration is DSB45 rails inclined at 1/20.

Because our system is nonlinear, we know that a transient investigation is not sufficient to determine the nonlinear critical speed. Therefore we calculate bifurcation diagrams. To illustrate the bifurcations at the lowest speeds, the diagram computed for a track configuration of DSB45 rails inclined at 1/20 and a stiffness of the steering system of 500 kN/m is shown in figure 8.16. The figure displays the maximum lateral displacement of the wheelset on the single-axle bogie as a function of the vehicle speed.

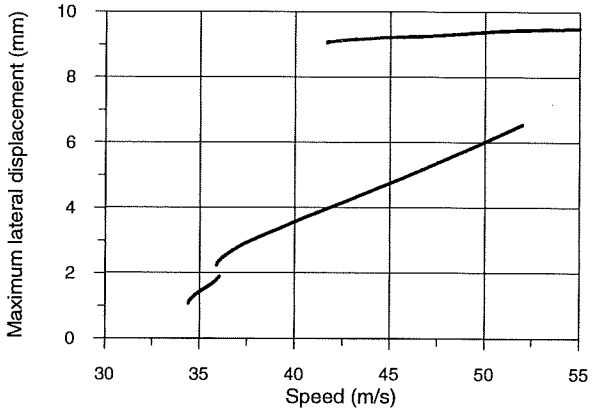

Figure 8.16: Bifurcation diagram showing the maximum lateral displacement of the wheelset on the single-axle bogie against vehicle speed for $c_{steering}$ = 500 kN/m and DSB45 rails inclined at 1/20.

Let us consider the scenario for decreasing speed. At $V = 55$ m/s a periodic solution with flange contact exists. For decreasing speed this solution undergoes a saddle-node bifurcation at $V \approx 41.7$ m/s. Another saddle-node at $V \approx 52$ m/s creates a stable periodic solution. This solution remains stable

until $V \approx 35.9$ m/s where a new saddle-node takes place. Finally, a low amplitude periodic solution exists in the interval of speed 34.4 m/s < V < 36.1 m/s. Hereby, we find a nonlinear critical speed of 34.4 m/s.

In figure 8.17 the saddle-node bifurcation determining the nonlinear critical speed is followed as a function of the steering stiffness in the interval 500 kN/m < $c_{steering}$ < 1000 kN/m. All four track configurations are shown. The figure shows that an increasing steering stiffness increases the nonlinear critical speed.

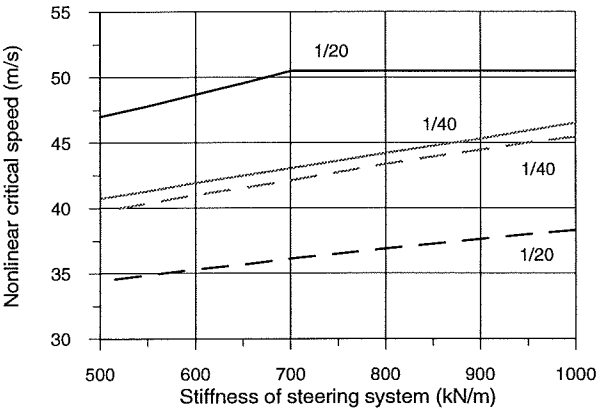

Figure 8.17: The nonlinear critical speed as a function of the stiffness of the steering system. The dashed lines are for DSB45 rails and the solid lines are for UIC60 rails.

For a UIC60 rail inclined at 1/20 there is a bend in the curve. This bend is due to the nonlinear critical speed changing from being a saddle-node of a solution with flange contact to a saddle-node of a solution without flange contact as the stiffness increases. When the rails are inclined at 1/40 the nonlinear critical speed is a saddle-node of a solution with flange contact, while the nonlinear critical speed for the DSB45 rail inclined at 1/20 is determined by a solution without flange contact. In all cases the single-axle bogie gives rise to the nonlinear critical speed. Figure 8.17 shows that in the investigated area of steering stiffness the UIC60 rails inclined at 1/20 gives the best track configuration.

Comparing the nonlinear critical speed with the transient analysis, we find that the transient analysis does not display the nonlinear critical speed. Especially for the rails inclined at 1/40 the nonlinear critical speed is much lower than indicated by the transient analysis. The reason for the differences is that the solutions with flange contact are not very attracting at lower speeds, so we do not reach their basin of attraction by a displacement of the single-axle bogie.

To point out the difference between the linear and nonlinear critical speed, we show in figure 8.18 the linear and nonlinear critical speeds as a function of the steering system. The track configurations are UIC60 and DSB45 rails both inclined 1/20. Figure 8.18 shows that the variations in the linear critical speed are almost the same as the variations in the nonlinear critical speed. However for the DSB45 rails the distance between the linear and nonlinear critical speed is increasing a little as the stiffness of the steering system increases.

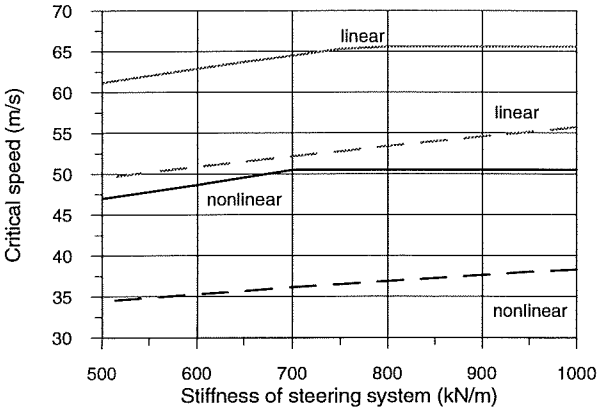

Figure 8.18: The linear and nonlinear critical speeds as a function of the stiffness of the steering system. The dashed lines are for DSB45 rails inclined at 1/20 and the solid lines are for UIC60 rails inclined at 1/20.

Further investigations of the other direction of travel, i.e. the single-axle bogie placed at the rear end of the vehicle, indicate that the vehicle seems to

be more stable, when the single-axle bogie is placed at the back. Some results of the other direction of travel are given in [Slivsgaard, 1994b].

8.3.2 Variation of yaw dampers

Another parameter which has influence on the stability of the single-axle bogie is the yaw dampers. For a steering stiffness of 750 kN/m we compute the linear and nonlinear critical speeds in dependence of the damping coefficient of the yaw dampers on the single-axle bogie. The damping coefficient is varied from 10 % of nominal damping to 200 % of nominal damping. The variations in the critical speeds are shown in figure 8.19. To display the lowest and highest nonlinear critical speeds the track configurations are DSB45 and UIC60 rails both inclined at 1/20.

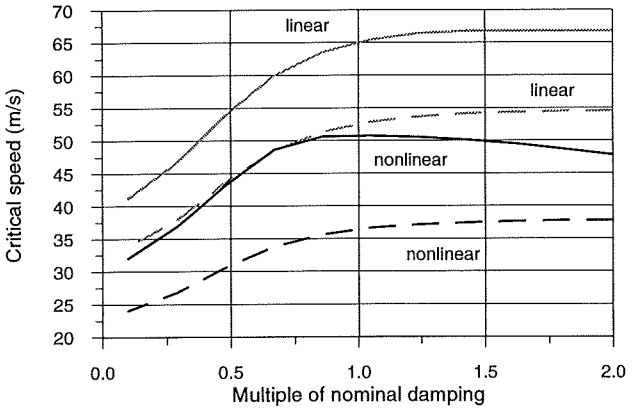

Figure 8.19: The linear and nonlinear critical speeds as a function of the damping of the yaw dampers on the single-axle bogie. The dashed lines are for DSB45 rails inclined at 1/20 and the solid lines are for UIC60 rails inclined at 1/20.

The figure illustrates that for a nominal value of damping cofficient and UIC60 rails inclined at 1/20 we find the maximum nonlinear critical speed. The other curves in the figure show that the critical speeds are increasing with increasing damping coefficient. However the slope of the curves is decreasing as the damping cofficient increases. This means that for the

DSB45 rails inclined at 1/20 the maximum nonlinear critical speed is found when the damping coefficient is twice the nominal value. This maximum nonlinear critical speed is only 1.4 m/s bigger than the critical speed for the nominal value of the damping coefficient.

From this investigation we can say that a good choice for the damping coefficient is the nominal value. We can also say that the yaw dampers should not be removed, because the nonlinear critical speed for the DSB45 rails inclined at 1/20 is less than 25 m/s for a low damping coefficient.

We notice that for the UIC60 rails inclined at 1/20 we have a case where the variations in the linear and nonlinear critical speeds are different. This indicates that for a nonlinear system, a linear analysis is not sufficient to find the effect on the dynamics of a varying parameter.

8.4 Running in curves

The above investigations of the stability have shown us that it is possible to choose a steering stiffness so that the vehicle is stable on the different track configurations. But also the effect of the steering stiffness for the vehicle negotiating a curve must be analysed.

Figure 8.20 shows the quasi-static value of the lateral displacement and the angle of attack of the wheelset on the single-axle bogie as a function of the stiffness of the steering system. The vehicle speed is 30 m/s. For this speed and for high steering stiffnesses, the vehicle will be unstable. Therefore the maximum investigated stiffness is 1 MN/m. The track configurations are UIC60 and DSB45 rails both inclined at 1/20. The curve has a radius of 500 m and a cant of 150 mm. Hereby, we obtain a cant deficiency of 125 mm.

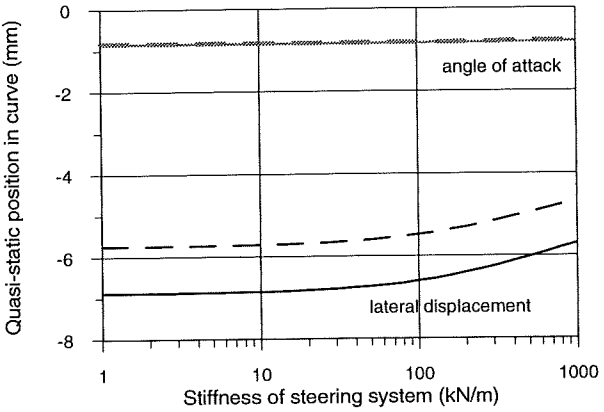

Figure 8.20: The quasi-static position of the wheelset on the single axle-bogie for R = 500 m, h = 150 mm, and V = 30 m/s. The dashed lines are for DSB45 rails inclined at 1/20 and the solid lines are for UIC60 rails inclined at 1/20.

In the figure we see that an increasing stiffness will reduce the displacement of the wheelset. Also the angle of attack, which is less than 1 mrad, decreases a trifle. This means that the wheelset becomes a little more radial with respect to the track center line as the stiffness increases. Hereby, we have an indication that the steering works as intended in the curve. The two track configurations give almost the same angle of attack.

When entering or leaving a curve the single-axle bogie can be steered wrong when placed in front. The bogie is in the curve, but the cars are not. Therefore, there is no angle between the cars and the stiffness of the steering will for a short time prevent the bogie from yawing properly. In an S-curve the missteering is expected to be worse.

As an example of this situation, we simulate the vehicle running through an S-curve. The S-curve is shown in figure 8.21. The radii are 300 m and the cants are zero. There are no transition curves. The rails are UIC60 rails inclined at 1/20. Along the S-curve, the vehicle speed is 14 m/s which corresponds to a cant deficiency of 100 mm. The steering stiffness is chosen as 750 kN/m.

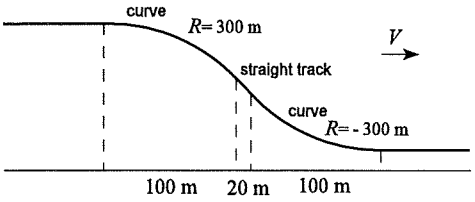

Figure 8.21: An example of an S-curve.

The angle of attack of the wheelset on the single-axle bogie is given in figure 8.22. The figure shows that there will be an angle of attack up to 7 mrad when entering and leaving the curve. Comparing the two curves more oscillations in the angle of attack are found when entering the second curve. For the big angle of attack the wheelset has flange contact. However, the big angle of attack appears only for a short period of time, which means that the duration of missteering is short.

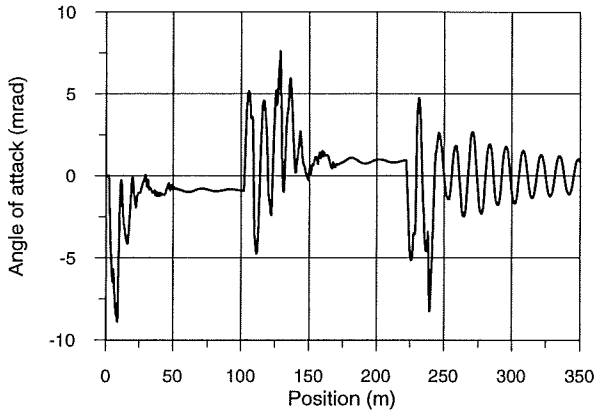

Figure 8.22: The angle of attack of the wheelset on the single-axle bogie when going through an S-curve with a speed of 14 m/s.

In our modelling we have neglected the longitudinal component of the contact point. In chapter 3 we described that the longitudinal component of the contact point only will have an influence if the wheelset has large yaw angles. These can be expected to occur in curves. However in the simulations discussed here we have seen that the angle of attack of the wheelset on the single-axle bogie is pretty small. So we say that neglecting the longitudinal component of the contact point is allowable in the results described.

8.5 Change in the vertical flexibility of the track

To combine our model of a two-car test vehicle with the beam model of the motion of the track (see paragraph 7.2), we consider the vertical case. The vehicle is running on a straight, perfect but flexible track. After a distance of 12.5 m, the flexibility of the ballast changes from being very hard $c_{ballast}$ = 200 MN/m to soft $c_{ballast}$ = 20 MN/m. After a distance of 37.5 m the flexibility changes back to hard. Such changes in track flexibility can be due to transition to and from bridges, tunnels etc.

In the simulations the rails are UIC60 rails inclined at 1/20. To ensure a stable run the vehicle speed is 30 m/s and the steering stiffness is 750 kN/m.

When the flexibility changes the vertical displacement of the front wheelset changes suddenly. The vertical displacement is 0.5 mm for the hard track and 1.9 mm for the soft track. The vertical contact force is shown in figure 8.23. The figure shows that the force varies up to 4 kN at the change in ballast flexibility.

This variation in contact forces confirms results described in [Zarembski, 1994]. Zarembski describes that railroad engineers have observed that locations with change in the flexibility of the track require frequent maintenance. At these locations large dynamic forces due to change in track deflection under load occur. Zarembski refers to measurements that support the increasing of dynamic forcing at transition sites, where the substructure of the track changes.

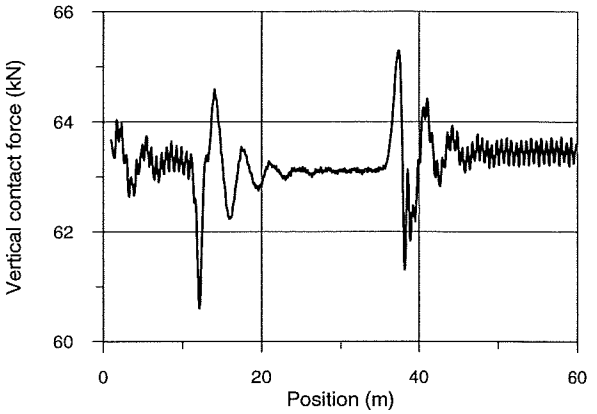

Figure 8.23: The vertical contact force when the flexibility of the track changes.

To study the effect of the changes of track flexibility on the car body we have to include the pitch rotation of the car body. Doing this we find that a change in flexibility gives rise to a vertical acceleration in the car body above the single-axle bogie of maximum 0.14 m/s^2 and over the two-axle bogie of 0.1 m/s^2. The frequency of the acceleration is around 10 Hz. The acceleration above the single-axle bogie is just at the limit of what a human being finds uncomfortable. This means the change in ballast and consequently the change in the vertical contact force has no significant influence on the comfort in the car by itselves.

Looking at the displacement of the track we find the results given in figure 8.24. The dotted line is at a point of the track with a flexibility of 200 MN/m, while the solid is for a flexibility of 20 MN/m. The passing of each axle in the vehicle is visible. The figure illustrates that the effect of the change in flexibility is on the displacement and on the time the track is disturbed. When the single-axle bogie passes, the hard track is disturbed 0.106 seconds while the soft track is disturbed 0.175 seconds. This corresponds to a length of track of 3.18 m and 5.25 m, respectively.

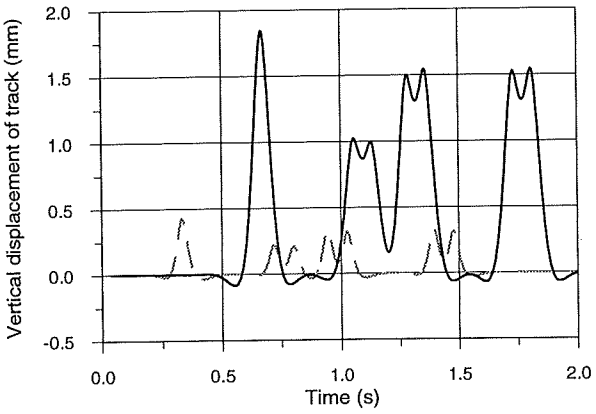

Figure 8.24: The vertical displacement of the track when the two-car test vehicle passes by. The dashed line is for a track section with hard flexibility and the solid line is for a track section with soft flexibility.

Comparing the figure with the results measured described in paragraph 6.2, we find good agreement. The values of displacement calculated here are larger than the measured. This could mean that the flexibility of the measured track was low, the vertical contact forces were high or a combination of both. The shape of the curves is the same.

8.6 A sum up

In this chapter we have analysed the dynamic behaviour of a two-car test vehicle with a single-axle bogie. The model was compared with a model of the single-axle bogie alone (chapter 5) and we found that the model of the whole vehicle gave rise to more oscillating solutions. Especially chaotic motions was found in the two-car model.

The single-axle bogie is steered in curves by a mechanical steering system. Detailed investigations of the influence of the stiffness of this steering system

on the stability of the vehicle have been made by applying different methods:

- First the most common method which is an eigenvalue analysis of the stationary solution was used. Hereby two types of instability was found. The hunting motion at high speeds and low steering stiffnesses and the car body instability at high stiffnesses and lower speeds.

- To illustrate the effect of a disturbance of a wheelset we introduced a transient method. By this an area at low speeds and stiffnesses was found to have a low damping rate of car body oscillations.

- Finally nonlinear methods resulted in the computation of the linear and nonlinear critical speeds.

The investigations led to the determination of a range of the steering stiffness system in which the vehicle is stable for speeds higher than the maximum operational speed.

For a varation of the damping in the yaw dampers attached to the single-axle bogie the linear and nonlinear critical speeds were found. By this we saw an example where the nonlinear critical speed showed a different variation than the linear.

As regards with the performance of the vehicle in curves we have shown a few examples. These illustrate that a stiffness of the steering system determined by the stability investigations gives rise to a pretty good curving behaviour.

The vertical beam model of the track derived in paragraph 7.2 have been used to show the influence of a change in the stiffness of the ballast on the dynamics of the vehicle and the track. We found that the change has an effect on the contact forces, but only a little effect on the comfort in the car by itselves. In respect of the track we have computed how the track moves when the vehicle passes by.

Chapter 9

Track irregularities

A good exercise when dealing with mathematical modelling is to investigate if the model can reproduce experimental data. To compare our model of the two-car test vehicle described in the previous chapter with field measurements, we analyse the vehicle running on a track with irregularities.

9.1 Test runs

In March 1995, test runs of the running characteristics of the two car test vehicle were made on the line between Hellerup and Hillerød north of Copenhagen. Before the runs, the mechanical steering system had been changed to a hydraulic system. The change was done mainly to reduce weight and because of lack of space underneath the coaches. However, the dynamic effect of the hydraulic system should be the same as for the mechanical one. In the modelling, we continue therefore using the mechanical approach. A description and drawing of the hydraulic steering can be found in [Ahrens, 1994].

During the runs, the lateral accelerations on the single-axle bogie, on the two-axle bogie on the same car and on the car body above the two bogies were measured. Furthermore, a strain gauge on one of the hydraulic cylinders in the steering recorded the force from the steering, and a displacement transducer measured the displacement of one yaw damper on the single-axle bogie. A picture of the displacement transducer mounted on the yaw damper is shown in figure 9.1. The vehicle speed and the position of the vehicle were found using a tacheometer. The speed was around 30 m/s.

Before the runs the wheels were reprofiled to have the DSB82-1 profile. Although the rail profiles are non-ideal, we use ideal profiles in the simulations. For the track sections discussed here the start profile was DSB45 rails inclined at 1/20. The track irregularities on the line were recorded in

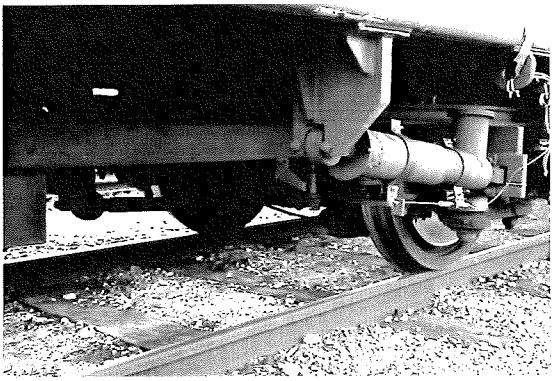

Figure 9.1: A picture of the displacement transducer mounted on a yaw damper.

February 1995. The results are transfered to be used in the simulations as the irregularities on the track. During the trials the weather was dry, but not sunny. In the simulations, we use a coefficient of adhesion on 0.3.

9.1.1 General results from the test runs

Here only a brief summary of the results from the test runs is given.

During the test the vehicle was running stably. For several runs on the same line we found the same results. This means that the data measured were reproducible.

Comparing the two bogies we find that the single-axle bogie is more affected by irregularities and switches than the two-axle bogie. For example, at Birkerød station (near km 24) a switch results in a lateral acceleration peak on the single-axle bogie of around 5.5 m/s^2 and on the two-axle bogie of around 3 m/s^2. The result is however not so surprising, because the two-axle bogie has the distance between the wheelsets to smear out the effect of an irregularity.

For the two directions of travel we find that the accelerations are bigger when the single-axle bogie is placed at the front end of the vehicle. When making this comparison we have to take into account that the track irregularities are not the same in the two cases. After considering the irregularities, we find no indication that the one track should be better than the other. So it seems as if the single-axle bogie is more sensitive to irregularities when it is placed at the front as compared with the back.

The results from the strain gauges on one of the hydraulic cylinders in the steering system give us an idea of the force from the steering system. Because of irregularities the force varies on straight track. However these variations have the same magnitude when the single-axle bogie is entering a curve, is actually in a curve, or is leaving a curve. This indicates that the position of the wheelset in a curve corresponds to, what the steering system forces it to adopt.

9.2 Comparison between measurements and simulations

For the comparison we choose two track sections; a straight line and a line containing a curve. For these sections the measurements show some dynamics in the vehicle. The direction of travel was towards Hillerød. The single-axle bogie was at the front of the vehicle.

9.2.1 Straight track

Let us first consider the run on the section with straight track. The track section is between Allerød and Hillerød, just after km 30. One kilometer of track and only the lateral irregularities are investigated. The lateral deviations of the track from a nominal gauge of 1435 mm are shown in figure 9.2. The irregularities vary around ± 2.5 mm, so the gauge varies around 1440 mm. On this track we study the lateral accelerations in the car body just above the single-axle bogie.

Besides looking at measurements, we compare our own simulations with simulations made with the vehicle dynamics simulations program SIDIVE.

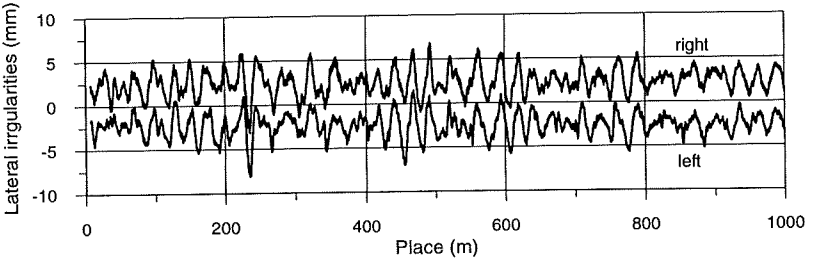

Figure 9.2: The lateral irregularities of right and left rail at the straight track section near km 30.

SIDIVE has been developed at CAF in Spain, [SIDIVE]. The two-car test vehicle is modelled in SIDIVE with the same construction and parameters as we have used in our own modelling. In this way, we can compare the results from the two programs.

The results found in our simulations, by SIDIVE, and by the measurements are given in figure 9.3, 9.4 and 9.5. In the three cases the vehicle speed was 30.8 m/s. The graphs in figure 9.3 and 9.4 are almost identical, so the two simulation programs give the same results. Comparison with the results from the measurements give the same variations, but the amplitudes are higher in figure 9.5 compared with figures 9.3 and 9.4.

9.2.2 Negotiating a curve

The other track section, which includes a curve, lies between Birkerød and Allerød around km 27. In figure 9.6, the measured inverse radius and cant for the section are shown. The curve is a left hand curve with a radius around 830 m and a cant around 58 mm. The lateral track irregularities are shown in figure 9.7. On the straight track the gauge varies around 1435 mm, while it goes up to 1450 mm in the curve.

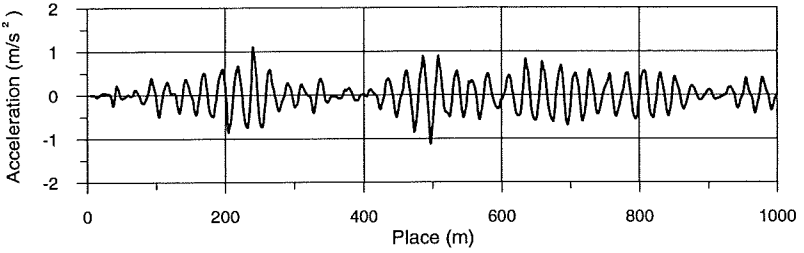

Figure 9.3: Simulated lateral acceleration in the car body above the single-axle bogie for the track section near km 30. Computed using the program described here.

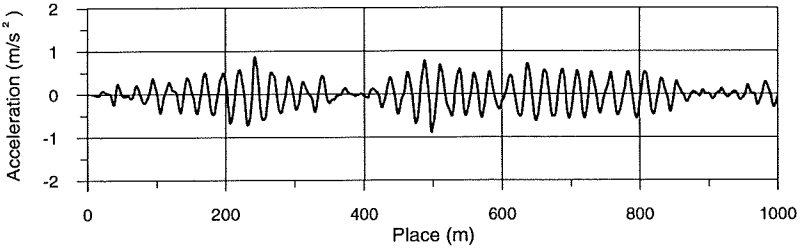

Figure 9.4: Simulated lateral acceleration in the car body above the single-axle bogie for the track section near km 30. Computed using the simulation program SIDIVE.

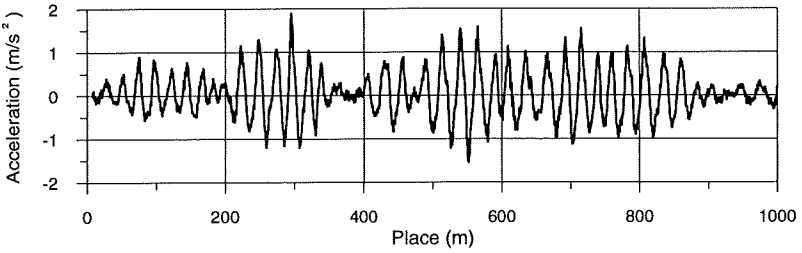

Figure 9.5: Measured lateral acceleration in the car body above the single-axle bogie for the track section near km 30.

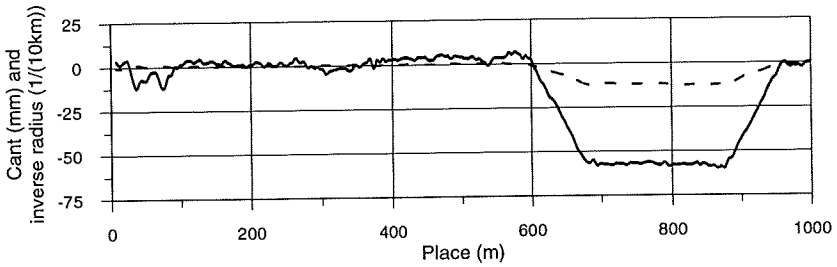

Figure 9.6: The solid line is the cant and the dashed line is the inverse radius of the track section near km 27.

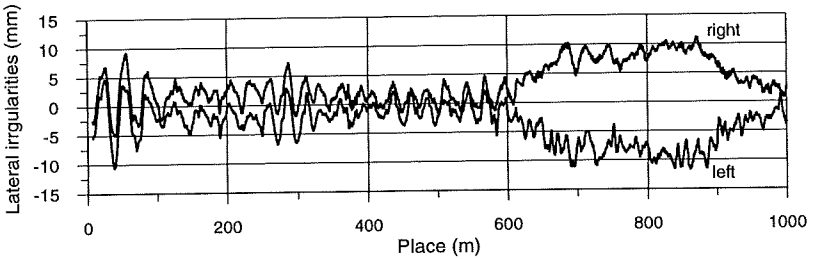

Figure 9.7: The lateral irregularities of right and left rail at the track section including a curve near km 27.

Figure 9.8 and 9.9 show the lateral accelerations in the car body above the single-axle bogie based on our simulations and the measurements. The vehicle speed is 30 m/s.

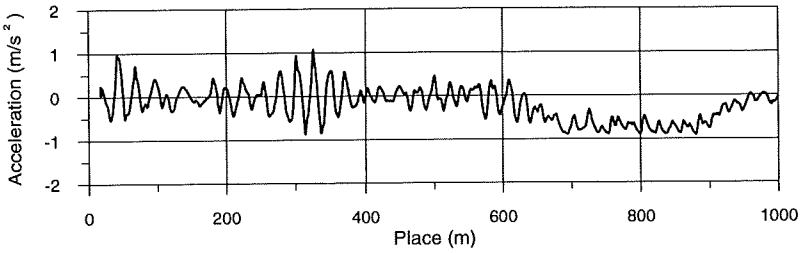

Figure 9.8: Simulated lateral acceleration in the car body above the single-axle bogie for the track section near km 27. Computed using the program described here.

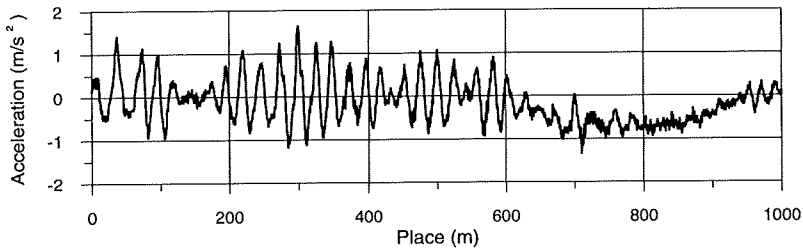

Figure 9.9: Measured lateral acceleration in the car body above the single-axle bogie for the track section near km 27.

Comparing the two figures, we find that the quasi-static acceleration is the same, but as in the previous example the measured accelerations are a little bigger on the straight track. The variations in the figures are the same.

Looking at the accelerations on the bogie instead of on the car, the measured accelerations contain much higher frequencies than those calculated. Considering the power spectrum of the data measured we find some frequencies around 10 Hz with high density. Because the kinematic

frequency of the wheelset in this situation is between 4 and 5 Hz, we do not expect the irregularities to cause so high frequencies. These frequencies could be due instead to eigenfrequencies in the bogie frame. To make a comparison between our simulations and the measurements, we remove all frequencies above 7 Hz. The results are shown in figure 9.10 and 9.11. The figures indicate the same overall pattern but the number and size of the acceleration peaks are different.

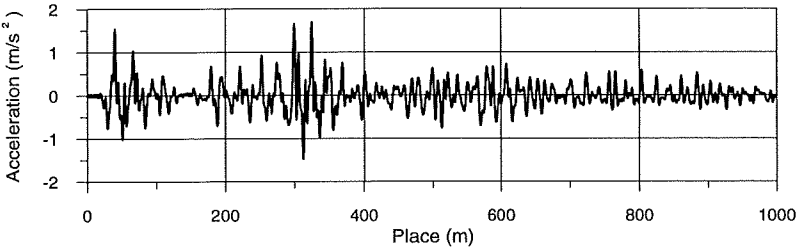

Figure 9.10: Simulated lateral acceleration in the single-axle bogie for the track section near km 27. Computed using the program described here.

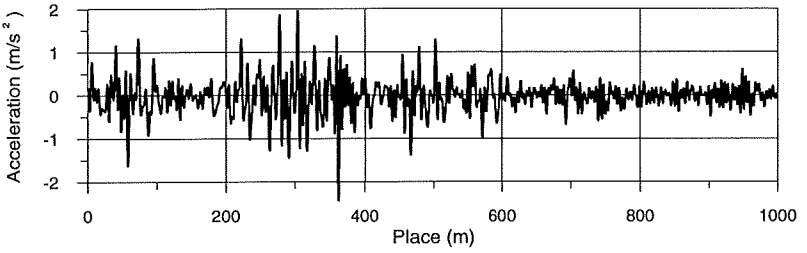

Figure 9.11: Measured lateral acceleration in the single-axle bogie for the track section near km 27.

Finally, we want to compare the relative displacements of a yaw damper on the single-axle bogie. The simulated and measured displacements are given in figure 9.12 and 9.13. Here we find very good agreement both qualitatively and quantitatively. The main difference is that the simulations show a few more oscillations at the end of the curve section, but the average displacement along the curve is the same.

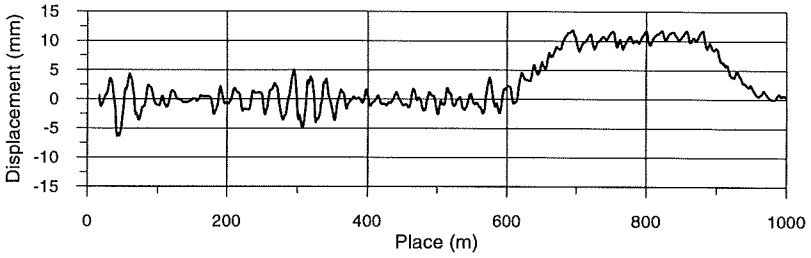

Figure 9.12: Simulated lateral displacement of a yaw damper on the single-axle bogie for the track section near km 27. Computed using the program described here.

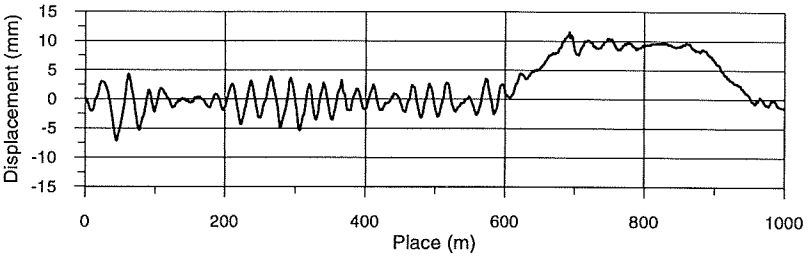

Figure 9.13: Measured lateral displacement of a yaw damper on the single-axle bogie for the track section near km 27.

In the simulations we can compute the angle of attack of the single-axle bogie in the curve. We find that the angle of attack for the wheelset in the curve is having a mean value around 0.5 mrad. We conclude hereby that the bogie is steered well in the curve.

9.3 Evaluation

We have illustrated that we find very good agreement between calculations with the simulation program developed here and the simulation package SIDIVE. Other theoretical investigations give the same conclusion.

Making comparison between the simulations and the measurements, we find that the measured and calculated displacements for a yaw-damper on the single-axle bogie correspond well. This indicates that the yaw motion of the single-axle bogie in the two cases seems to be the same. The calculated lateral accelerations show the same variations but the amplitudes are lower than those measured.

If we consider the two accelerations measured in the car body (one above each bogie) we can calculate the lateral motion and the yaw motion of the car. Comparing these with the simulated ones, we find that there is better agreement for the yaw motion than for the lateral motion. This supports the agreement for the displacement of the yaw damper.

Reasons for the difference in the lateral accelerations could be that the parameters used in the calculations are not the same as in real life. Some parameters of importance could be:

- In the model only linear characteristics of suspensions are used. It is however seldom that a suspension element is totally linear.

- When a suspension element is manufactured the accuracy to which its characteristics can be made is limited. We have not included any deviations from the values given.

- We assume the weight of the car body to be equally distributed. If there is a shift in the weight this could affect the accelerations.

- We have seen in the simulations discussed in previous chapters that the profiles are important for the stability of the vehicle. In the simulations we have used ideal wheel and rail profiles. The wheel profiles were reprofiled before the runs but the rail profiles were worn.

- The coefficient of adhesion is unknown and can vary along the track.

- In the simulations the track is considered as being rigid. The flexibility of the track could have an influence on the dynamics.

The influence of the coefficient of adhesion is investigated further. To do this we use the track section near km 30. We do not change the coefficients of adhesion along the track, but make several runs with different coefficient of adhesion. In figure 9.14 the difference of the acceleration on the car body above the single-axle bogie between using a coefficient of adhesion of 0.2 and 0.4 is plotted. The figure shows that at some places along the track the deviation can be up to 0.8 m/s^2. Considering the accelerations this deviation is not only due to the amplitudes being different but also to the diverging frequencies. Generally the amplitudes of the accelerations are larger for a coefficient of adhesion of 0.2 than for 0.4.

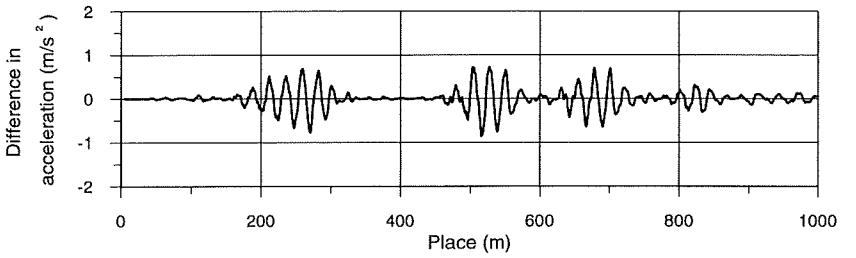

Figure 9.14: The difference in the lateral acceleration in the car body above the single-axle bogie between using a coefficient of adhesion of 0.2 and 0.4.

From figure 9.14 we find that the coefficient of adhesion have an influence on the lateral dynamics. This is contrary to an analysis of the lateral ride described in [Eickhoff, 1993]. Eickhoff et al illustrate that changes in the coefficient of adhesion above 0.2 have a little effect on the lateral ride. However as it also appears from figure 9.14 the influence is very dependent on the irregularities and consequently the track section analysed.

As mentioned above the flexibility of the track can be expected to have an influence on the accelerations simulated. Using the simple track model as a model of the flexibility of the track (paragraph 7.1) we can make the same simulations as above. We find that the lateral motion of the track is small and making comparison with the simulations on the rigid track we find no significant difference in the accelerations on the car body.

9.3.1 Reproducible results

Several simulations with different initial conditions give the same trajectory over a period of integration of a few seconds. This means, the simulated data as well as the measured data are reproducible. If we increase the speed so the vehicle becomes unstable, the accelerations become bigger but are still reproducible with respect to changes in initial conditions.

In railway dynamics results is most often found to be reproducible. However in [Pascal, 1994] it is described that test runs with an unstable freight car under the same conditions give different results. Also in simulations Pascal shows that the trajectory of the motion of the freight car running on the irregular track is very sensitive to initial conditions. Compared to the test vehicle the suspension elements in a freight car have dry friction and are therefore highly nonlinear. Consequently the freight car is expected to show more complex behaviour than a passenger car.

The reason why Pascal find non-reproducible results can be that the trajectory is chaotic and therefore illustrates a sensitive dependence on initial conditions, or there are two possible solutions for the system to which the trajectory due to small variations is changing.

9.3.2 Nonlinear analysing of track irregularities

Using methods from nonlinear dynamics the track irregularities can be analysed.

If we consider the irregularities of a straight track as a time series, $s(n)$ we can determine the largest Lyapunov exponent of this series by using a method described in [Wolf, 1985]. The method is based upon a reconstruction of the phase space using the information in s(n). In 1981 Takens described that the phase space can be reconstructed by a d-dimensional vector, [Takens, 1981]:

$$y(n) = (s(n),\ s(n + T),\ ...,\ s(n + (d - 1)T)) , \tag{9.1}$$

where T is called the delay time and d the embedding dimension. These two parameters must be defined when determining the largest Lyapunov exponent by the method of Wolf et al. Methods to do this is described in [Abarbanel, 1992] and we refer to [Abarbanel, 1992] for additional information about nonlinear methods to analyse time series.

In the case of the lateral track irregularities of the left and right rail near km 30 we find that the largest Lyapunov exponent for both rails converges to a value around 0.2. This could indicate that the vehicle is forced by a chaotic trajectory. However before making any conclusions further investigation of the significance of the data must be carried out for example by using surrogate data, [Smith, 1992].

We have found that a railway vehicle probably can be exposed to a chaotic forcing. The consequence of such a chaotic forcing is a very interesting topic for a future research.

Chapter 10

Conclusion

We have in the above described the mathematical modelling of a railway vehicle. The aim of this thesis has been not only to focus on the vehicle but also on the track it runs on.

Different models have been analysed by applying methods from nonlinear dynamics. Especially the difference between a linear and a nonlinear analysis has been pointed out by introducing the linear and nonlinear critical speed. When optimizing a parameter we found an example where the linear and nonlinear analysis did not lead to the same optimal value.

We have illustrated that it is not sufficient to consider the trajectory of a disturbance of a bogie to find the nonlinear critical speed. On the other hand the nonlinear critical speed must be found by following solutions as the speed varies. However it has also been shown that transient analyses can be used to investigate how attracting the stable stationary solution is and consequently in which area of the speed range a disturbance of the wheelset will be transfered to the car body.

Using a model consisting of one single-axle bogie we have discussed a few modelling parameters. When neglecting a degree of freedom for the perturbation of the angular velocity of the wheelset in the modelling we have shown that this has an effect on the solutions derived. This was not expected because the perturbation is only present to ensure that the vehicle moves with a constant speed. Furthermore we have described an example of applying the creep force theory of Shen, Hedrick and Elkins or Kalkers simplified theory implemented in FASTSIM give approximately the same solutions to the system.

For the modelling of the track we have considered two models:

- A simple model of the whole track as one rigid body following each wheelset.

- A model where the rails are modelled as Euler-Bernoulli beams discretely supported by rigid sleepers.

We have used the simple model to find the critical speeds of the single-axle bogie in dependence of the flexibility of the track and come to the conclusion that the flexibility seems to have no significant influence on the critical speeds. The simple model was compared with the elastic track model and we found that they show almost the same motion of the bogie. For the motion of the track we found that if flange contact occurs, the two models give different results. However in this case further investigations of the influence of the torsion of the rail webs must be carried out. Furthermore the elastic model has been used to show the variation of vertical contact forces when the support of the sleepers changes.

The parameters for the track models have been inspired by measurements. These measurements, which have been carried out for the track affected by a static load or a passing train, have been discussed.

For a model of a two-car test vehicle with a single-axle bogie we have considered the dynamics for the vehicle running on

- a straight track
- a curved track
- a track with irregularities.

The stability of the vehicle has been studied for a straight track. Here we have focussed on the effect of varying stiffness of the steering mechanism, which controls the yaw of the wheelset in curves. The analysis led to a suitable value for the steering system. Using this value in the simulations of the vehicle negotiating a curve we found that the wheelset on the single-axle bogie had an angle of attack close to the optimal value which yields a minimum wear of wheels and rails.

To test our modelling the simulations of the two-car test vehicle running on a track with irregularities were compared with corresponding meaurements. The comparison illustrated the same variations of the accelerations but the amplitudes differed. The displacement of a yaw damper showed approximately the same picture in the case measured and simulated. We have formulated and discussed some explanations for these results.

Only a few chaotic regions have been found in our investigations of models. For two of these regions the chaotic attractors contained a bend, where the bend corresponds to a lateral displacement of a wheelset which results in a discontinuity in the radius of curvature of a rail. In one case we showed that the chaos disappears, when the discontinuity is smoothened out by a spline.

Generally we conclude that the investigations have led to an better understanding of the dynamic behaviour of a railway vehicle and as to which parameters influence the dynamics.

10.1 Further investigations

To mention a few topics for further investigations we suggest the following.

A continuation of the analysis described here is to investigate the dynamics of the New S-train for the Copenhagen network. We have in detail described how a test vehicle with one single-axle bogie behaves. A study of the new train with only single-axle bogies could be interesting. This can be done without major changes in the program developed.

As regards the flexibility of the track we have simulated how a change in track flexibility can change the dynamic forces between wheel and rail. It will be interesting to analyse this further by measuring the variation of the flexibility along a track and studying how the variation measured influences the dynamic behaviour of the vehicle.

Inspired by the analysis of the track irregularities, we find that an interesting topic for future work in nonlinear dynamics is to analyse how dynamic

system behaves when it is forced not only by a periodic motion but also by a chaotic trajectory. For practical use a simple dynamic system should be considered.

Appendix A

Calculation of relative displacement

In this appendix we describe the general calculation of the relative displacement between two bodies in a railway vehicle running on a straight track. The degrees of freedom for the bodies are mentioned in chapter 2.

The relative displacement between a point on body 1, which is displaced A_{iB1} from its inertial system, and a point on body 2, which is displaced A_{iB2} from its inertial system, is calculated as

$$\Delta r_{12} = \Delta r_1 - \Delta r_2 = \Delta r_{c1} - \Delta r_{c2} + A_{iB1} r_{p1} - A_{iB2} r_{p2} - (r_{p1} - r_{p2}) \,, \quad \text{(A.1)}$$

where

$$\Delta r_{c1} = \begin{bmatrix} 0 \\ y_1 \\ z_1 \end{bmatrix} \quad \text{and} \quad \Delta r_{c2} = \begin{bmatrix} 0 \\ y_2 \\ z_2 \end{bmatrix} \quad \text{(A.2)}$$

are the displacements of the center of gravity of the bodies, and

$$r_{p1} = \begin{bmatrix} dx_1 \\ dy_1 \\ dz_1 \end{bmatrix} \quad \text{and} \quad r_{p2} = \begin{bmatrix} dx_2 \\ dy_2 \\ dz_2 \end{bmatrix} \quad \text{(A.3)}$$

are the position vectors from the center of gravity of the bodies to the points (for instance the places where a spring element is fastened). The two inertial systems must be parallel.

The different coordinate systems are illustrated in figure A.1.

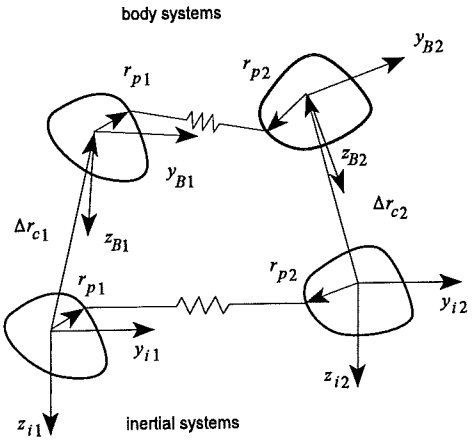

Figure A.1: The relative displacement for a suspension element.

The transformation matrices between the inertial system and the body system are

$$A_{iB\ 1,2} = A_{Bi\ 1,2}^{-1} = A_{Bi\ 1,2}^{T} = \begin{bmatrix} 1 & -\psi_{1,2} & 0 \\ \psi_{1,2} & 1 & -\phi_{1,2} \\ 0 & \phi_{1,2} & 1 \end{bmatrix}. \qquad \text{(A.4)}$$

We can now calculate the relative displacement

$$\Delta r_{12} = \begin{bmatrix} \Delta rx_{12} \\ \Delta ry_{12} \\ \Delta rz_{12} \end{bmatrix} = \begin{bmatrix} 0 \\ y_1 \\ z_1 \end{bmatrix} - \begin{bmatrix} 0 \\ y_2 \\ z_2 \end{bmatrix} + \begin{bmatrix} 1 & -\psi_1 & 0 \\ \psi_1 & 1 & -\phi_1 \\ 0 & \phi_1 & 1 \end{bmatrix} \begin{bmatrix} dx_1 \\ dy_1 \\ dz_1 \end{bmatrix} - \begin{bmatrix} 1 & -\psi_2 & 0 \\ \psi_2 & 1 & -\phi_2 \\ 0 & \phi_2 & 1 \end{bmatrix} \begin{bmatrix} dx_2 \\ dy_2 \\ dz_2 \end{bmatrix} - \left(\begin{bmatrix} dx_1 \\ dy_1 \\ dz_1 \end{bmatrix} - \begin{bmatrix} dx_2 \\ dy_2 \\ dz_2 \end{bmatrix} \right), \tag{A.5}$$

where a computation yields

$$\Delta r_{12} = \begin{bmatrix} dx_1 - \psi_1 dy_1 - dx_2 + \psi_2 dy_2 - dx_1 + dx_2 \\ y_1 - y_2 + \psi_1 dx_1 + dy_1 - \phi_1 dz_1 - \psi_2 dx_2 - dy_2 + \phi_2 dz_2 - dy_1 + dy_2 \\ z_1 - z_2 + \phi_1 dy_1 + dz_1 - \phi_2 dy_2 - dz_2 - dz_1 + dz_2 \end{bmatrix} \tag{A.6}$$

$$= \begin{bmatrix} -\psi_1 dy_1 + \psi_2 dy_2 \\ y_1 - y_2 + \psi_1 dx_1 - \phi_1 dz_1 - \psi_2 dx_2 + \phi_2 dz_2 \\ z_1 - z_2 + \phi_1 dy_1 - \phi_2 dy_2 \end{bmatrix}.$$

This relative displacement is used to find the forces and moments from a spring element placed at the points on the bodies. For clearness we will in the following calculations use a spring element defined by a simple linear homogeneous spring with a stiffness matrix $c = \text{diag}(cx, cy, cz)$ (this could be a primary suspension).

In this way we get the forces on body 1, $F_1 = c(-\Delta r_{12})$ and body 2, $F_2 = c\Delta r_{12}$:

$$F_1 = \begin{bmatrix} Fx_1 \\ Fy_1 \\ Fz_1 \end{bmatrix} = \begin{bmatrix} -cx\,\Delta rx_{12} \\ -cy\,\Delta ry_{12} \\ -cz\,\Delta rz_{12} \end{bmatrix}, \quad F_2 = \begin{bmatrix} Fx_2 \\ Fy_2 \\ Fz_2 \end{bmatrix} = \begin{bmatrix} cx\,\Delta rx_{12} \\ cy\,\Delta ry_{12} \\ cz\,\Delta rz_{12} \end{bmatrix}. \tag{A.7}$$

Then the moments become

$$M_1 = \begin{bmatrix} Mx_1 \\ My_1 \\ Mz_1 \end{bmatrix} = \begin{bmatrix} dx_1 \\ dy_1 \\ dz_1 \end{bmatrix} \times \begin{bmatrix} Fx_1 \\ Fy_1 \\ Fz_1 \end{bmatrix} = \begin{bmatrix} Fz_1 dy_1 - Fy_1 dz_1 \\ Fz_1 dx_1 - Fx_1 dz_1 \\ Fy_1 dx_1 - Fx_1 dy_1 \end{bmatrix}, \tag{A.8}$$

where index 1 is replaced by index 2 for body 2.

We draw to attention that *My* is not used when the degrees of freedom of the pitch motions in vehicle are neglected.

Appendix B

Calculation of penetration

In this appendix we calculate the penetration of the wheel into the rail. The calculations are inspired by Jensen, [Jensen, 1995].

The penetration is used to determine the normal force on the contact plane. We therefore need the penetration in a direction normal to the contact plane. The coordinate systems and transformation matrices are described in chapter 2. The positions of contact are illustrated in figure B.1 and B.2. The longitudinal position of the contact points are neglected in the calculations.

In the basis coordinate system for the wheelset, the contact point on the right wheel is given by

$$v_{wheel,r} = \begin{bmatrix} 0 \\ y_w \\ z_w \end{bmatrix} + A_{iB} \begin{bmatrix} 0 \\ a_r \\ r_r \end{bmatrix} = \begin{bmatrix} -\psi_w a_r \\ y_w + a_r - \phi_w r_r \\ z_w + \phi_w a_r + r_r \end{bmatrix} \tag{B.1}$$

and the left wheel

$$v_{wheel,l} = \begin{bmatrix} 0 \\ y_w \\ z_w \end{bmatrix} + A_{iB} \begin{bmatrix} 0 \\ -a_l \\ r_l \end{bmatrix} = \begin{bmatrix} \psi_w a_l \\ y_w - a_l - \phi_w r_l \\ z_w - \phi_w a_l + r_l \end{bmatrix}. \tag{B.2}$$

Also the position of the contact point on the rail must be found in the basis coordinate system for the wheelset.

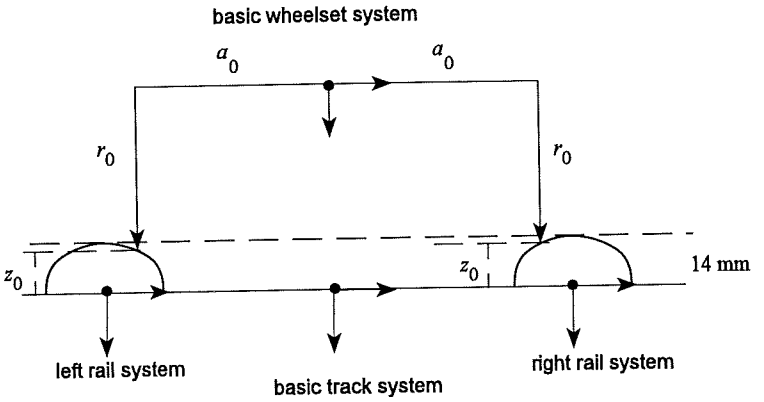

Figure B.1: The position of contact when the bodies are placed in their central position.

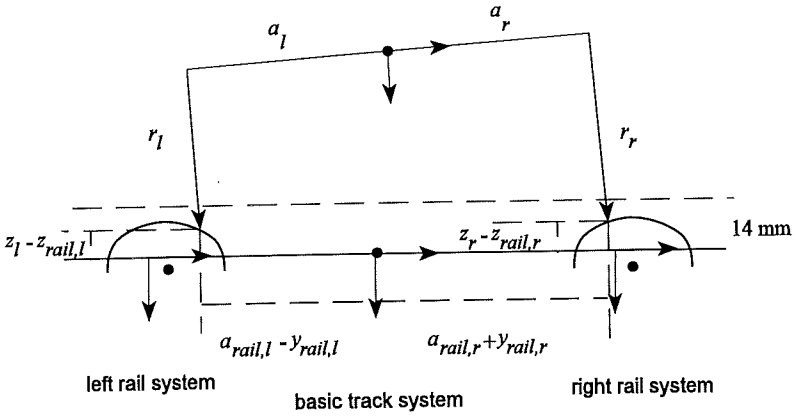

Figure B.2: The position of contact when the bodies are displaced.

For right rail we obtain

$$v_{rail,r} = \begin{bmatrix} 0 \\ a_{rail,r} \\ r_0 + z_0 - z_r \end{bmatrix} + \begin{bmatrix} 0 \\ y_{rail,r} \\ z_{rail,r} \end{bmatrix} + \begin{bmatrix} 0 \\ y_{irr,r} \\ z_{irr,r} \end{bmatrix} \tag{B.3}$$

and for the left rail

$$v_{rail,l} = \begin{bmatrix} 0 \\ -a_{rail,l} \\ r_0 + z_0 - z_l \end{bmatrix} + \begin{bmatrix} 0 \\ y_{rail,l} \\ z_{rail,l} \end{bmatrix} + \begin{bmatrix} 0 \\ y_{irr,l} \\ z_{irr,l} \end{bmatrix}, \tag{B.4}$$

where z_0 and r_0 are the vertical coordinate of the contact point and the rolling radius when the wheelset is placed in its central position. y_{irr} and z_{irr} are the irregularities of a rail.

We can now calculate the penetration

$$\Delta p_{basic} = v_{rail} - v_{wheel} \tag{B.5}$$

This penetration must be projected into the contact plane. Doing this we need the transformation between the basis wheelset system and the coordinate systems attached to the contact points. For right contact point we get

$$\begin{bmatrix} x_{con,r} \\ y_{con,r} \\ z_{con,r} \end{bmatrix} = \begin{bmatrix} 1 & 0 & 0 \\ 0 & \cos\delta_r & -\sin\delta_r \\ 0 & \sin\delta_r & \cos\delta_r \end{bmatrix} \begin{bmatrix} 1 & \psi & 0 \\ -\psi & 1 & \phi \\ 0 & -\phi & 1 \end{bmatrix} \begin{bmatrix} x_{bwheelset} \\ y_{bwheelset} \\ z_{bwheelset} \end{bmatrix}. \tag{B.6}$$

If we use that we have neglected the trigonometric functions of ϕ we obtain

$$\begin{bmatrix} x_{con,r} \\ y_{con,r} \\ z_{con,r} \end{bmatrix} = \begin{bmatrix} 1 & \psi & 0 \\ -\psi\cos\delta_r & \cos(\delta_r - \phi) & -\sin(\delta_r - \phi) \\ -\psi\sin\delta_r & \sin(\delta_r - \phi) & \cos(\delta_r - \phi) \end{bmatrix} \begin{bmatrix} x_{bwheelset} \\ y_{bwheelset} \\ z_{bwheelset} \end{bmatrix}. \tag{B.7}$$

For simplification we asume that ϕ is considerable smaller than δ, so we use $\cos(\delta_r - \phi_r) \approx \cos\delta_r$ and $\sin(\delta_r - \phi_r) \approx \sin\delta_r$. The validation of this assumption has been revealed by the simulations. We then get

$$\begin{bmatrix} x_{con,r} \\ y_{con,r} \\ z_{con,r} \end{bmatrix} = \begin{bmatrix} 1 & \psi & 0 \\ -\psi\cos\delta_r & \cos\delta_r & -\sin\delta_r \\ -\psi\sin\delta_r & \sin\delta_r & \cos\delta_r \end{bmatrix} \begin{bmatrix} x_{bwheelset} \\ y_{bwheelset} \\ z_{bwheelset} \end{bmatrix}. \tag{B.8}$$

Similar for the left contact point we get

$$\begin{bmatrix} x_{con,l} \\ y_{con,l} \\ z_{con,l} \end{bmatrix} = \begin{bmatrix} 1 & \psi & 0 \\ -\psi\cos\delta_l & \cos\delta_l & \sin\delta_l \\ \psi\sin\delta_l & -\sin\delta_l & \cos\delta_l \end{bmatrix} \begin{bmatrix} x_{bwheelset} \\ y_{bwheelset} \\ z_{bwheelset} \end{bmatrix}, \tag{B.9}$$

where we have used $\cos(\delta_l + \phi_l) \approx \cos\delta_l$ and $\sin(\delta_l + \phi_l) \approx \sin\delta_l$.

We can now make a projection on the contact plane. For right contact point we have

$$\Delta p_{contact,r} = \begin{bmatrix} 1 & \psi & 0 \\ -\psi\cos\delta_r & \cos\delta_r & -\sin\delta_r \\ -\psi\, sinn\,\delta_r & \sin\delta_r & \cos\delta_r \end{bmatrix} \cdot \begin{bmatrix} \psi_w a_r \\ a_{rail,r} + y_{rail,r} + y_{irr,r} - y_w - a_r + \phi_w r_r \\ r_0 + z_0 - z_r + z_{rail,r} + z_{irr,r} - z_w - \phi_w a_r - r_r \end{bmatrix} \tag{B.10}$$

and for left contact point

$$\Delta p_{contact,l} = \begin{bmatrix} 1 & \psi & 0 \\ -\psi\cos\delta_l & \cos\delta_l & \sin\delta_l \\ \psi\sin\delta_l & -\sin\delta_l & \cos\delta_l \end{bmatrix} \cdot \begin{bmatrix} -\psi_w a_l \\ -a_{rail,l} + y_{rail,l} + y_{irr,l} - y_w + a_l + \phi_w r_l \\ r_0 + z_0 - z_l + z_{rail,l} + z_{irr,l} - z_w + \phi_w a_l - r_l \end{bmatrix}. \tag{B.11}$$

In determination of the contact forces, we use the penetration in the direction normal to the contact plane. So we want the z-coordinate of $\Delta p_{contact}$:

$$\begin{aligned}
\Delta p_{z,r} &= \sin\delta_r(a_{rail,r} - a_r + y_{rail,r} + y_{irr,r} - y_w + \phi_w r_r) + \\
&\quad \cos\delta_r(z_0 + r_0 - z_r - r_r + z_{rail,r} + z_{irr,r} - z_w - \phi_w a_r)\ , \\
\Delta p_{z,l} &= -\sin\delta_l(-a_{rail,l} + a_l + y_{rail,l} + y_{irr,l} - y_w + \phi_w r_l) + \\
&\quad \cos\delta_l(z_0 + r_0 - z_l - r_l + z_{rail,l} + z_{irr,l} - z_w + \phi_w a_l)\ .
\end{aligned} \tag{B.12}$$

Appendix C

Calculation of creep

In this appendix we describe the general expressions for the creepage. When running on straight track the term $1/R$ is equal to zero. In the calculations we use the coordinate systems described in chapter 2.

The creep is defined as the relative velocities in the contact region between wheel and rail. In the contact region the velocity of the wheel consists of two terms; the angular velocity of the wheel-axle, ω and the translatory motion, V_T. The velocity of the rail in the contact region is assumed to be a translatory motion.

The angular velocity of the wheel-axle is given by

$$\omega = \dot{\phi}_w \vec{x}_{bwheelset} + \Omega \vec{y}_{wheelset} + \dot{\psi}_w \vec{z}_{wheelset}, \tag{C.1}$$

which we want to convert to the wheelset-system

$$\omega = \begin{bmatrix} 1 & \psi_w & 0 \\ -\psi_w & 1 & \phi_w \\ 0 & -\phi_w & 1 \end{bmatrix} \begin{bmatrix} \dot{\phi}_w \\ 0 \\ 0 \end{bmatrix} + \begin{bmatrix} 0 \\ \Omega \\ \dot{\psi}_w \end{bmatrix} = \begin{bmatrix} \dot{\phi}_w \\ -\psi_w \dot{\phi}_w + \Omega \\ \dot{\psi}_w \end{bmatrix}. \tag{C.2}$$

Calculating the translatory motion of the wheelset, we have to take the curves into account. The angle between the level of the rails and the horizontal plane, β is given by the cant devided by the distance between the rails. With a normal cant of maximum 150 mm, we get $\beta_{max} = 0.1$. Hereby, when multiplying with a trigonometric function of β, we can replace the function by the linear terms in its Taylor expansion. The radius of the curve is R and is calculated positive for a right hand curve. The curve is illustrated in figure C.1.

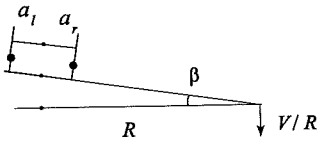

Figure C.1: The parameters in a curve.

In the basic coordinate system for the wheelset we obtain the translatory velocity of the right wheel

$$V_{T,r} = \begin{bmatrix} 0 \\ V\beta/R \\ V/R \end{bmatrix} \times \begin{bmatrix} 0 \\ -R + a_r \\ 0 \end{bmatrix} + \begin{bmatrix} 0 \\ \dot{y}_w \\ \dot{z}_w \end{bmatrix} = \begin{bmatrix} V - Va_r/R \\ \dot{y}_w \\ \dot{z}_w \end{bmatrix}, \tag{C.3}$$

and the left wheel

$$V_{T,l} = \begin{bmatrix} 0 \\ V\beta/R \\ V/R \end{bmatrix} \times \begin{bmatrix} 0 \\ -R - a_l \\ 0 \end{bmatrix} + \begin{bmatrix} 0 \\ \dot{y}_w \\ \dot{z}_w \end{bmatrix} = \begin{bmatrix} V + Va_l/R \\ \dot{y}_w \\ \dot{z}_w \end{bmatrix}. \tag{C.4}$$

By using A_{Bi}, V_T is expressed in the wheelset coordinate axes as

$$\begin{aligned} V_{T,r} &= \begin{bmatrix} 1 & \psi_w & 0 \\ -\psi_w & 1 & \phi_w \\ 0 & -\phi_w & 1 \end{bmatrix} \begin{bmatrix} V - Va_r/R \\ \dot{y}_w \\ \dot{z}_w \end{bmatrix} \\ &= \begin{bmatrix} V - Va_r/R + \psi_w\dot{y}_w \\ -\psi_w(V - Va_r/R) + \dot{y}_w + \phi_w\dot{z}_w \\ -\phi_w\dot{y}_w + \dot{z}_w \end{bmatrix} \end{aligned} \tag{C.5}$$

and

$$V_{T,l} = \begin{bmatrix} V + Va_l/R + \psi_w \dot{y}_w \\ -\psi_w(V + Va_l/R) + \dot{y}_w + \phi_w \dot{z}_w \\ -\phi_w \dot{y}_w + \dot{z}_w \end{bmatrix}. \tag{C.6}$$

Neglecting the longitudinal position of the contact point, the position vector of the right contact point in terms of the wheelset system becomes

$$L_r = a_r \vec{y}_{wheelset} + r_r \vec{z}_{wheelset} \tag{C.7}$$

and of the left contact point

$$L_l = -a_l \vec{y}_{wheelset} + r_l \vec{z}_{wheelset}. \tag{C.8}$$

Now we can calculate the velocity of the wheel at the contact point

$$V_{wheel} = V_T + \omega \times L, \tag{C.9}$$

where we insert the expressions and due to small angles and displacements neglect the second order terms of displacements and rotations

$$V_{wheel,r} = \begin{bmatrix} V - Va_r/R + r_r\Omega - a_r\dot{\psi}_w \\ -\psi_w(V - Va_r/R) + \dot{y}_w - r_r\dot{\phi}_w \\ \dot{z}_w + a_r\dot{\phi}_w \end{bmatrix} \tag{C.10}$$

and

$$V_{wheel,l} = \begin{bmatrix} V + Va_l/R + r_l\Omega + a_l\dot{\psi}_w \\ -\psi_w(V + Va_l/R) + \dot{y}_w - r_l\dot{\phi}_w \\ \dot{z}_w - a_l\dot{\phi}_w \end{bmatrix}. \tag{C.11}$$

V_{wheel} is projected onto the contact plane

$$V_{wheel,r} = \begin{bmatrix} 1 & 0 & 0 \\ 0 & \cos\delta_r & -\sin\delta_r \\ 0 & \sin\delta_r & \cos\delta_r \end{bmatrix} \begin{bmatrix} V - Va_r/R + r_r\Omega - a_r\dot{\psi}_w \\ -\psi_w(V - Va_r/R) + \dot{y}_w - r_r\dot{\phi}_w \\ \dot{z}_w + a_r\dot{\phi}_w \end{bmatrix}$$

$$= \begin{bmatrix} V - Va_r/R + r_r\Omega - a_r\dot{\psi}_w \\ (-\psi_w(V - Va_r/R) + \dot{y}_w - r_r\dot{\phi}_w)\cos\delta_r - (\dot{z}_w + a_r\dot{\phi}_w)\sin\delta_r \\ (-\psi_w(V - Va_r/R) + \dot{y}_w - r_r\dot{\phi}_w)\sin\delta_r + (\dot{z}_w + a_r\dot{\phi}_w)\cos\delta_r \end{bmatrix} \tag{C.12}$$

and

$$V_{wheel,l} = \begin{bmatrix} 1 & 0 & 0 \\ 0 & \cos\delta_l & \sin\delta_l \\ 0 & -\sin\delta_l & \cos\delta_l \end{bmatrix} \begin{bmatrix} V + Va_l/R + r_l\Omega + a_l\dot{\psi}_w \\ -\psi_w(V + Va_l/R) + \dot{y}_w - r_l\dot{\phi}_w \\ \dot{z}_w - a_l\dot{\phi}_w \end{bmatrix}$$

$$= \begin{bmatrix} V + Va_l/R + r_l\Omega + a_l\dot{\psi}_w \\ (-\psi_w(V + Va_l/R) + \dot{y}_w - r_l\dot{\phi}_w)\cos\delta_l + (\dot{z}_w - a_l\dot{\phi}_w)\sin\delta_l \\ -(-\psi_w(V + Va_l/R) + \dot{y}_w - r_l\dot{\phi}_w)\sin\delta_l + (\dot{z}_w - a_l\dot{\phi}_w)\cos\delta_l \end{bmatrix}. \tag{C.13}$$

If we assume that each rail has only one lateral and one vertical degree of freedom, the velocity of a rail is given by

$$V_{rail} = \dot{y}_{rail}\vec{y}_{rail} + \dot{z}_{rail}\vec{z}_{rail}\,, \tag{C.14}$$

and a projection onto the contact plane gives

$$V_{rail,r} = \begin{bmatrix} 1 & \psi & 0 \\ -\psi\cos\delta_r & \cos\delta_r & -\sin\delta_r \\ -\psi\sin\delta_r & \sin\delta_r & \cos\delta_r \end{bmatrix} \begin{bmatrix} 0 \\ \dot{y}_{rail,r} \\ \dot{z}_{rail,r} \end{bmatrix} = \begin{bmatrix} 0 \\ \dot{y}_{rail,r}\cos\delta_r - \dot{z}_{rail,r}\sin\delta_r \\ \dot{y}_{rail,r}\sin\delta_r + \dot{z}_{rail,r}\cos\delta_r \end{bmatrix} \quad \text{(C.15)}$$

and

$$V_{rail,l} = \begin{bmatrix} 1 & \psi & 0 \\ -\psi\cos\delta_l & \cos\delta_l & \sin\delta_l \\ \psi\sin\delta_l & -\sin\delta_l & \cos\delta_l \end{bmatrix} \begin{bmatrix} 0 \\ \dot{y}_{rail,l} \\ \dot{z}_{rail,l} \end{bmatrix} = \begin{bmatrix} 0 \\ \dot{y}_{rail,l}\cos\delta_l + \dot{z}_{rail,l}\sin\delta_l \\ -\dot{y}_{rail,l}\sin\delta_l + \dot{z}_{rail,l}\cos\delta_l \end{bmatrix}, \quad \text{(C.16)}$$

where we have neglected the second order terms of displacements and rotations. For the transformation matrix between the rail system (the basic wheelset system) and the system attached to the contact points we refer to appendix B.

We can now calculate the creepage. The longitudinal creep is given by

$$\xi_x = \frac{V_{wheel,x} - V_{rail,x}}{V}, \quad \text{(C.17)}$$

where C.12 and C.15 are substituted

$$\xi_{x,r} = 1 - \frac{a_r}{R} + \frac{r_r\Omega - a_r\dot{\psi}_w}{V} \quad \text{(C.18)}$$

and C.13 and C.16 are substituted

$$\xi_{x,l} = 1 + \frac{a_l}{R} + \frac{r_l\Omega + a_l\dot{\psi}_w}{V}. \quad \text{(C.19)}$$

The lateral creep is given by

$$\xi_y = \frac{V_{wheel,y} - V_{rail,y}}{V}, \quad \text{(C.20)}$$

where substitution yields

$$\xi_{y,r} = (-\psi_w(1 - \frac{a_r}{R}) + \frac{\dot{y}_w - r_r\dot{\phi}_w - \dot{y}_{rail,r}}{V})\cos\delta_r - (\frac{\dot{z}_w + a_r\dot{\phi}_w - \dot{z}_{rail,r}}{V})\sin\delta_r \tag{C.21}$$

and

$$\xi_{y,l} = (-\psi_w(1 + \frac{a_l}{R}) + \frac{\dot{y}_w - r_l\dot{\phi}_w - \dot{y}_{rail,l}}{V})\cos\delta_l + (\frac{\dot{z}_w - a_l\dot{\phi}_w - \dot{z}_{rail,l}}{V})\sin\delta_l \,. \tag{C.22}$$

These expressions can be simplified on the assumption that the wheel and rail stay in contact. This means projecting of the velocity between wheel and rail into the normal to the contact plane should give zero

$$V_z = V_{wheel,z} - V_{rail,z} = 0 \,. \tag{C.23}$$

For the right contact point we get

$$V_{z,r} = (-\psi_w(V - \frac{Va_r}{R}) + \dot{y}_w - r_r\dot{\phi}_w - \dot{y}_{rail,r})\sin\delta_r + (\dot{z}_w + a_r\dot{\phi}_w - \dot{z}_{rail,r})\cos\delta_r = 0 \tag{C.24}$$

$$\Downarrow$$

$$-(-\psi_w(V - \frac{Va_r}{R}) + \dot{y}_w - r_r\dot{\phi}_w - \dot{y}_{rail,r})\tan\delta_r = \dot{z}_w + a_r\dot{\phi}_w - \dot{z}_{rail,r}$$

and similarly for the left contact point

$$(-\psi_w(V + \frac{Va_l}{R}) + \dot{y}_w - r_l\dot{\phi}_w - \dot{y}_{rail,l})\tan\delta_l = \dot{z}_w - a_l\dot{\phi}_w - \dot{z}_{rail,l} \,. \tag{C.25}$$

Using C.24 and C.25 in C.21 and C.22 leads to

$$\xi_{y,r} = (-\psi_w(1 - \frac{a_r}{R}) + \frac{\dot{y}_w - r_r\dot{\phi}_w - \dot{y}_{rail,r}}{V})/\cos\delta_r \qquad \text{(C.26)}$$

and

$$\xi_{y,l} = (-\psi_w(1 + \frac{a_l}{R}) + \frac{\dot{y}_w - r_l\dot{\phi}_w - \dot{y}_{rail,l}}{V})/\cos\delta_l \,. \qquad \text{(C.27)}$$

Finally, we want to determine the spin creepage, which is defined by the relative angular velocity at the contact point. The spin creepage is found by projecting of the angular velocity of the wheelset into the normal to the contact plane

$$\xi_{sp,r} = \frac{1}{V}[0 \;\; \sin\delta_r \;\; \cos\delta_r]\begin{bmatrix}\dot{\phi}_w \\ \Omega \\ \dot{\psi}_w\end{bmatrix} = \frac{\Omega\sin\delta_r + \dot{\psi}_w\cos\delta_r}{V} \qquad \text{(C.28)}$$

and

$$\xi_{sp,l} = \frac{1}{V}[0 \;\; -\sin\delta_l \;\; \cos\delta_l]\begin{bmatrix}\dot{\phi}_w \\ \Omega \\ \dot{\psi}_w\end{bmatrix} = \frac{-\Omega\sin\delta_l + \dot{\psi}_w\cos\delta_l}{V} \,, \qquad \text{(C.29)}$$

where all second order terms of rotations are neglected.

Appendix D

The rails as Euler-Bernoulli beams

In this appendix we solve a partial differential equation describing the motion of a rail using the method of separation. The method is inspired by Zhai and Sun [Zhai, 1993].

If we model the rail as an Euler-Bernoulli beam the vertical or lateral motion of a rail $u(x, t)$ is given by

$$EI\frac{\delta^4 u(x,t)}{\delta x^4} + m\frac{\delta^2 u(x,t)}{\delta t^2} = -\sum_{i=1}^{N_{sleeper}} F_{sleeper}\,\delta(x - x_i) - \sum_{j=1}^{N_{wheelset}} F_{contact}\,\delta(x - x_j)$$
$$= F_{external}\,\delta(x - x') \qquad (D.1)$$
$$= f(x,t)\ ,$$

where E is the modulus of elasticity of the rail, I is the bending stiffness in the lateral or vertical direction and m is the mass of the rail per meter. $\delta(x)$ is Dirac's delta function. The rail is supported by $N_{sleeper}$ number of sleepers placed at x_i in the longitudinal direction. The force from each sleeper is $F_{sleeper}$. There is running $N_{wheelset}$ number of wheelsets on the rail. Each wheelset is placed at the longitudinal position x_j. The contact force between a wheel and the rail is defined by $F_{contact}$.

We wish to solve D.1 by applying the method of separation. For this, we look for a solution of the form

$$u(x,t) = \sum_{n=1}^{\infty} p_n(x)\,q_n(t)\ . \qquad (D.2)$$

Now we choose p_n in such a way, that p_n is a solution of the homogeneous equation

$$EI\frac{d^4 p_n}{dx^4} + m\omega_n^2 p_n = 0 \,, \tag{D.3}$$

where ω_n, $n = 1, 2 .. \infty$, are constants. The equation has the solution

$$p_n = c_1 \sin\gamma_n x + c_2 \cos\gamma_n x + c_4 \sinh\gamma_n x + c_4 \cosh\gamma_n x \tag{D.4}$$

with $\gamma_n^4 = \dfrac{\omega_n^2 m}{EI}$.

Since the rail is a beam, which is simply supported at the ends and has length L, we obtain the following boundary conditions

$$p_n(0) = \frac{d^2 p_n}{dx^2}(0) = p_n(L) = \frac{d^2 p_n}{dx^2}(L) = 0 \,. \tag{D.5}$$

These are substituted in D.4. For the boundary condition at 0

$$\left.\begin{aligned} c_2 + c_4 &= 0 \\ -\gamma_n^2 c_2 + \gamma_n^2 c_4 &= 0 \end{aligned}\right\} \; c_2 = c_4 = 0 \tag{D.6}$$

and for the boundary condition at L

$$\left.\begin{aligned} c_1 \sin\gamma_n L + c_3 \sinh\gamma_n L &= 0 \\ -c_1\gamma_n^2 \sin\gamma_n L + c_3\gamma_n^2 \sinh\gamma_n L &= 0 \end{aligned}\right\} \Rightarrow \begin{vmatrix} \sin\gamma_n L & \sinh\gamma_n L \\ -\sin\gamma_n L & \sinh\gamma_n L \end{vmatrix} = 0 \tag{D.7}$$

$$\Downarrow$$

$$\sin\gamma_n L \sinh\gamma_n L = 0$$

$\gamma = 0$ is a trivial solution. So we have

$$\gamma_n L = n\pi \Leftrightarrow \gamma_n = \frac{n\pi}{L} \,, \tag{D.8}$$

which is substituted in the boundary condition for $p_n(L)$

$$c_1 \sin\frac{n\pi}{L}L + c_3 \sinh\frac{n\pi}{L}L = 0 \Rightarrow c_3 = 0 \,. \tag{D.9}$$

Now we have an expression for p_n

$$p_n = c_1 \sin \gamma_n x \ . \tag{D.10}$$

q_n can be defined by using the expansion theorem. The right side of equation D.1 is expanded by eigenfunctions

$$f(x,t) = F_{external}\delta(x - x') = \sum_{n=1}^{\infty} f_n(t) p_n(x) \ , \tag{D.11}$$

where f_n fulfill the condition:

$$\begin{aligned} f_n &= \frac{(p_n, f(x,t))}{(p_n, p_n)} \\ &= \frac{\int_0^L \delta(x - x') F_{external} c_1 \sin \gamma_n x \ dx}{\int_0^L c_1^2 \sin^2 \gamma_n x \ dx} \\ &= F_{external} \frac{c_1 \sin \gamma_n x'}{c_1^2 \frac{L}{2}} \\ &= F_{external} \frac{2}{L c_1} \sin \gamma_n x' \ . \end{aligned} \tag{D.12}$$

Substitution in D.1 and using the expansion theorem give an equation for $q_n(t)$

$$\begin{aligned} & EI \gamma_n^4 q_n + m \ddot{q}_n = f_n \\ \Updownarrow \\ & \ddot{q}_n + \frac{EI}{m} \gamma_n^4 q_n = F_{external} \frac{2}{m L c_1} \sin \gamma_n x' \ . \end{aligned} \tag{D.13}$$

c_1 is found by

$$p_n(x') = c_1 \sin \gamma_n x' = \frac{2}{mLc_1} \sin \gamma_n x' . \tag{D.14}$$

Since this must be true for all $\sin\gamma_n x' \neq 0$, we get

$$c_1 = \sqrt{\frac{2}{mL}} . \tag{D.15}$$

Now we can determine $u(x, t)$ by calculating the final sum

$$u(x,t) = \sum_{n=1}^{N} p_n(x) q_n(t) , \tag{D.16}$$

where

$$p_n(x) = \sqrt{\frac{2}{mL}} \sin \frac{n\pi x}{L} \tag{D.17}$$

and $q_n(t)$ is found by solving the differential equation

$$\ddot{q}_n(t) + \frac{EI}{m}\left(\frac{n\pi}{L}\right)^4 q_n(t) = -\sum_{i=1}^{N_{sleeper}} F_{sleeper} p_n(x_i) - \sum_{j=1}^{N_{wheelset}} F_{contact} p_n(x_j) . \tag{D.18}$$

N, which is the mode number, is defined by the frequencies and wavelengths we include in the simulations.

Appendix E

The wheel and rail profiles

The following three pages contain scale drawings of

- the DSB82-1 wheel profile
- the UIC60 rail profile
- the DSB45 rail profile.

DSB82-1 wheel profile:

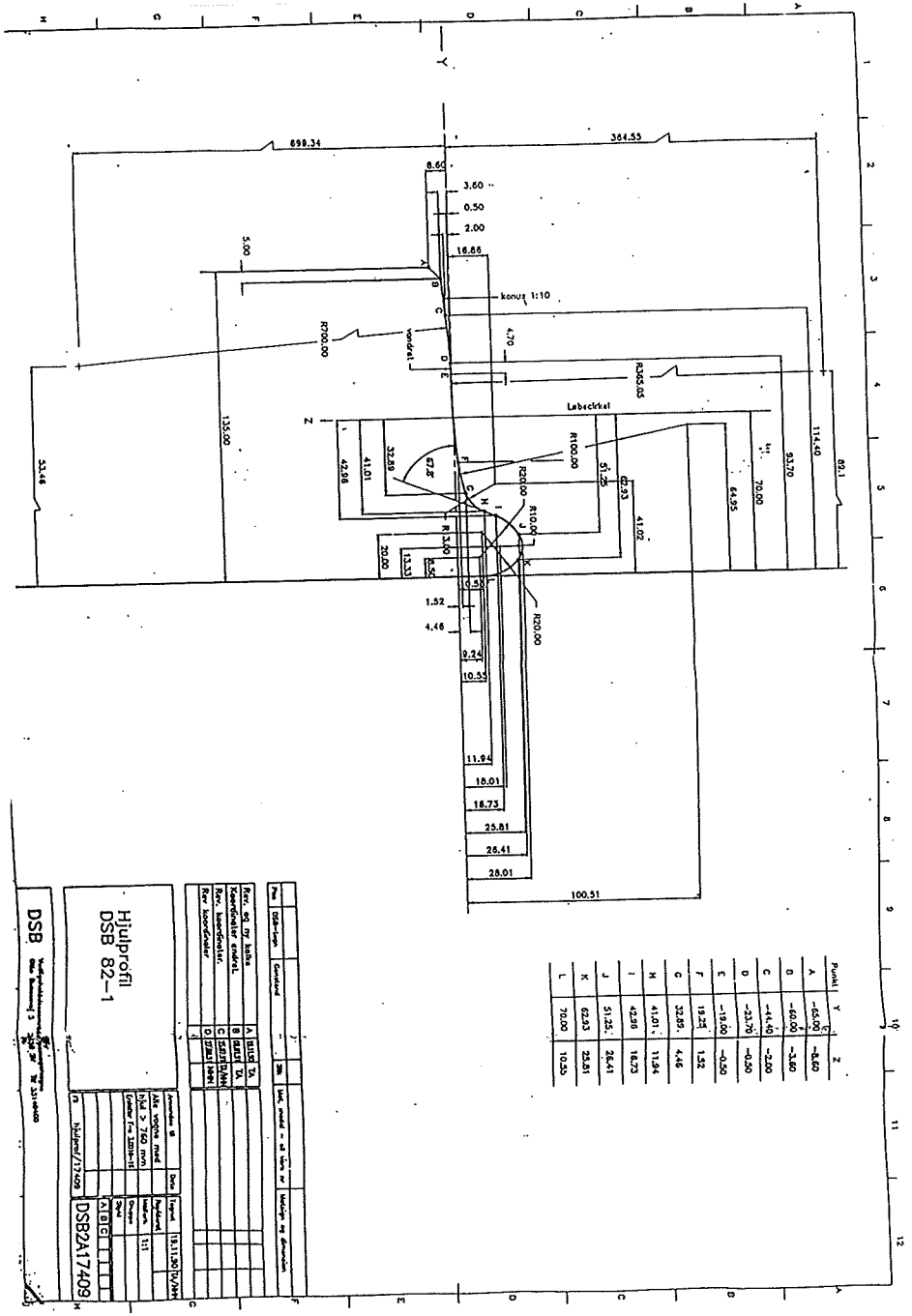

UIC60 rail profile:

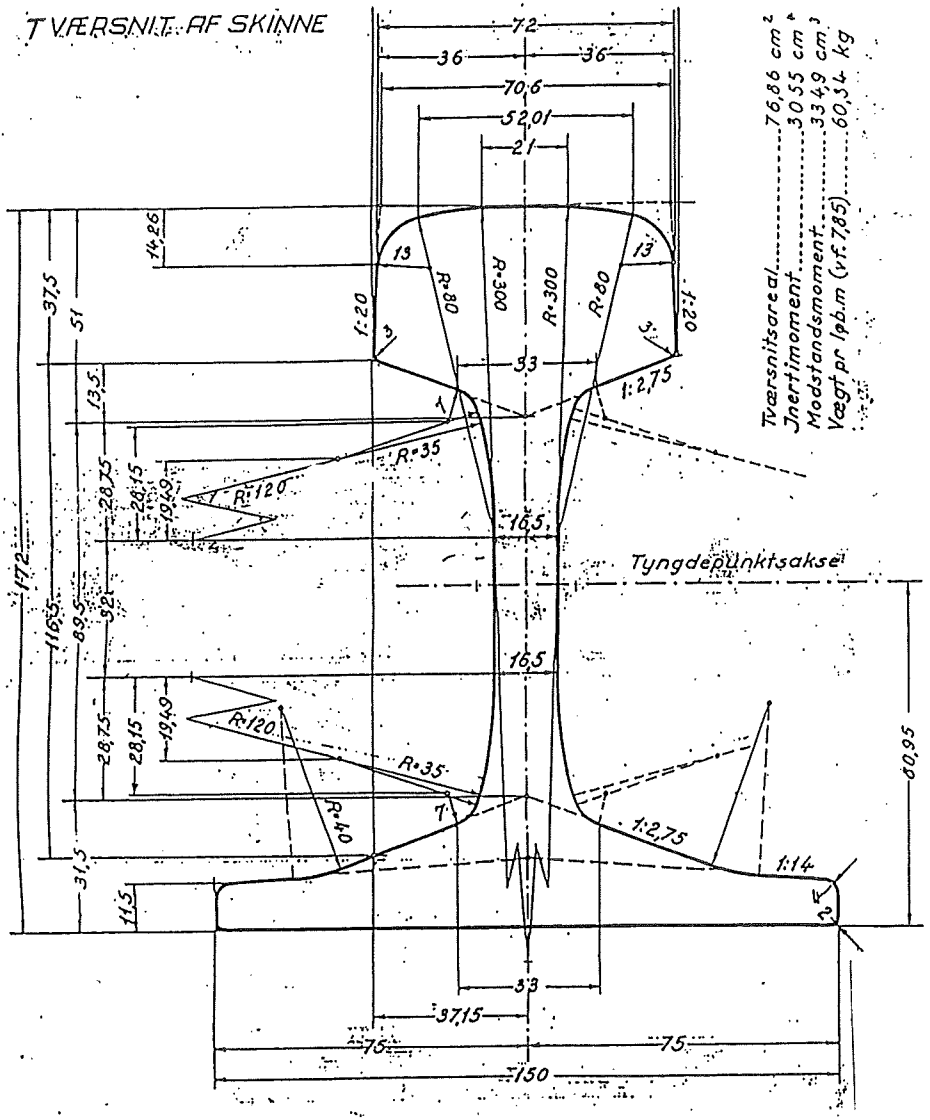

DSB45 rail profile:

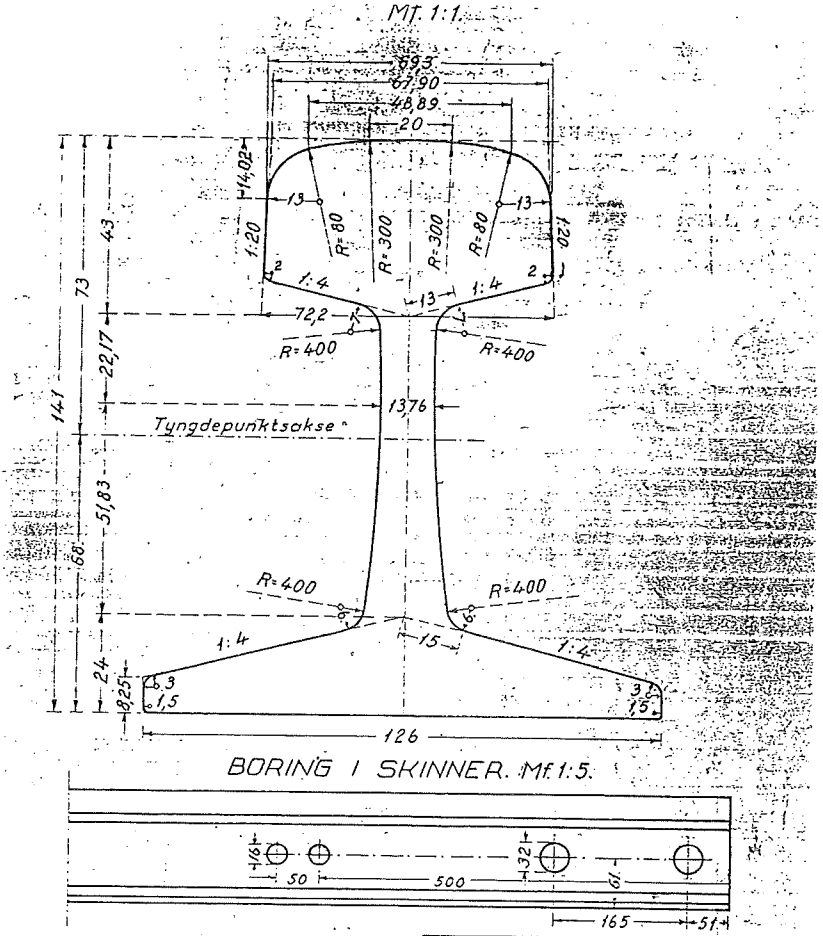

Tværsnitsareal ..... 57,92 cm²
Inertimoment ..... 1520 cm⁴
Modstandsmoment ..... 209 cm³
Vægt pr. løb. m. ..... 45,46 kg.
Huller bores kun efter specifikation.

Målene er i mm.

Danske Statsbaner
Baneafdelingen Sporkontoret

Overbygning V.
Skinne.

Konstr.	d. 16/7 1959.	Blad	5501ᵃ
Tegnet. P. Hyldahl Clausen			
Kontr. M.SS			
Rev. a 16/7.59.			

Appendix F

The structure of the program

We will biefly outline the main structure of the program used for calculation of accelerations.

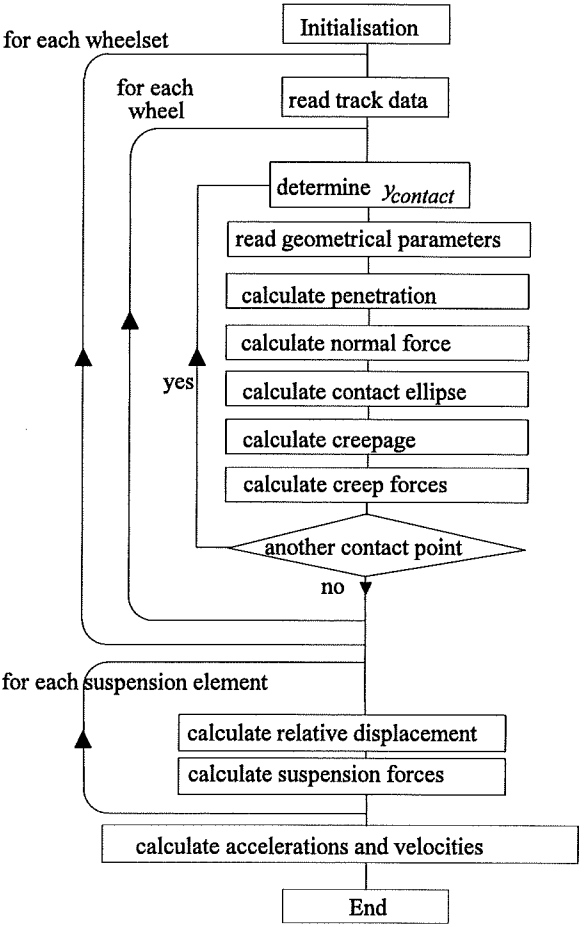

Danish summary - Resumé

Denne afhandling omhandler matematisk modellering af et jernbanekøretøj. Modelleringen er ikke kun fokuseret omkring selve køretøjet, men også sporet det kører på. Forskellige modeller opstilles og deres beskrivelse af køretøjets dynamik undersøges.

Hovedparten af undersøgelserne er koncentreret om stabiliteten af køretøjet. Hermed bliver to begreber introduceret: *den lineære kritiske hastighed* og *den ikke-lineære kritiske hastighed.* Den lineære kritiske hastighed er den hastighed, hvor køretøjet bliver ustabilt ud fra en lineær analyse, mens den ikke-lineære kritiske hastighed bestemmes ud fra, at der ikke findes nogle stabile oscillerende løsninger for hastigheder under denne hastighed. Forskellen mellem en lineær og en ikke-lineær analyser bliver hermed beskrevet.

Ved anvendelse af metoder fra den ikke-lineære dynamik studeres de fundne løsninger, herunder om de er periodiske eller kaotiske. Blandt andet beskrives og analyseres en periode adding sekvens.

Som køretøj benyttes et test tog fra den københavnske S-bane. Toget består af to vogne, hvor en almindelig to-akslet bogie på den ene vogn er erstattet af en enkelt-akslet bogie (en såkaldt KERF bogie). Bogien er speciel, idet den er styret gennem kurver af et mekanisk styresystem. Det er dynamikken af denne bogie, der er fokuseret på.

Til undersøgelse af forskellige modelleringstekniske forhold opstilles modeller alene af den enkelt-akslede bogie. Dynamikken af modellen af begge vogne undersøges for forskellige skinnekonfigurationer:

- et perfekt og retliniet spor
- en kurve
- et spor som er fleksibelt i lodret retning
- et spor med irregulariteter.

Disse undersøgelser viser blandt andet betydningen af stivheden i styresyste-

met. For sporet med irregulariteter sammenlignes simuleringerne med tilsvarende målinger.

Herudover beskrives to forskellige modeller af skinnelegemet:

- En simpel model, hvor hele sporet betragtes som en masse følgende med hvert hjulsæt.

- En elastisk model, hvor skinnerne beregnes som Euler-Bernoulli bjælker diskret understøttet af svellerne.

Den simple model benyttes til at studere indflydelsen af sporets fleksibilitet på dynamikken af den enkelt-akslet bogie, mens den elastiske model for eksempel kan bruges til at finde effekten af varierende fleksibilitet hen langs sporet.

Endelig beskrives et par målinger af et spors fleksibilitet.

Nomenclature

In the following a description of the notation of some of the parameters and the degrees of freedom in the modelling is given.

a	Longitudinal semiaxis of contact ellipse.
a_r, a_l	Absolut distance from the center of gravity of a wheelset to the right or left contact point.
α	Angle of attack in a curve.
b	Lateral semiaxis of contact ellipse.
β	Angle between the levels of the rails and the horizontal plane in a curve, $\beta = h/1.5$.
c	A stiffnees.
δ_r, δ_l	Contact angle between wheel-axle and right or left contact plane.
$\Delta p_{z,r}$, $\Delta p_{z,l}$	Penetration of the wheelset into right or left rail.
Δr	The relative displacement between two bodies.
E	Modulus of elasticity for steel, $E = 2.1 \cdot 10^{11}$ N/m^2.
F	A force.
g	The gravity, $g \approx 9.81$ m/s^2, or the track gauge.
h	Cant in a curve, positive when the left rail is raised compared with the right.
I_x	The moment of inertia of a body around its longitudinal main

	axis.
I_y	The moment of inertia of a body around its lateral main axis.
I_z	The moment of inertia of a body around its vertical main axis.
k	A damping.
λ_e	Equivalent conicity.
m	The mass of body.
M_z	The spin creep moment.
μ	Coefficient of adhesion, default value 0.3.
N	Normal force, or the number of degrees of freedom.
ξ_{sp}	Spin creepage.
ξ_x	Longitudinal creepage.
ξ_y	Lateral creepage.
r_r, r_l	Rolling radius of right or left contact point.
R	Radius of a curve, positive in a right hand curve.
$R_{rail,r}$, $R_{rail,l}$	Radius of curvature of right or left rail profile.
$R_{wheel,r}$, $R_{wheel,l}$	Radius of curvature of right or left wheel profile.
σ	Poissons ratio, $\sigma = 0.25$.
T_x	Longitudinal creep force.
T_y	Lateral creep force.

V	Vehicle speed. V_{linear} is the critical speed from a linear analysis and $V_{nonlinear}$ is the critical speed from a nonlinear analysis.
ϕ	Roll motion, rotation around longitudinal axis.
w	Displacement between a damper and a stiffness in series.
y	Lateral motion.
ψ	Yaw motion, rotaion around vertical axis.
z	Vertical motion.
z_r, z_l	Vertical coordinate of right or left contact point with respect to the rails.
Ω	The angular velocity of a wheelset around its lateral axis, $\Omega = \Omega_0 + \hat{\upsilon} = V/r_0 + \hat{\upsilon}$.
$\hat{\upsilon}$	Perturbation of the angular velocity of a wheelset around its lateral axis.

A dot above a degree of freedom denotes differentiation with respect to time.

Litterature

[Abarbanel,1992] H.D.I. Abarbanel, R. Brown, and L.S. Tsimring: *The Analysis of Observed Chaotic Data in Physical System*, 1992.

[Ahrens, 1994] R. Ahrens: S-bahn Kopenhagen Fahrzeugdynamik eines Gliederzuges mit kurvengesteuerten Einzelradsatz-Fahrwerken, *Proceedings of Systemdynamik der Eisenbahn*, Hennigsdorf, 1994, 109-118 (in German).

[Berg, 1994] M. Berg: A moving track model for vehicle dynamics analysis, *Proc of 4th Mini Conference on Vehicle System Dynamics, Identification and Anomalies*, Budapest, November 1994.

[DB-Minden, 1991] DB-Minden: *Lauftechniche Untersuchung DSB Triebzug IC3*, Deutsche Bundesbahn Versuchanstalt Minden, 1991 (in German).

[Devaney, 1989] R.L. Devaney: *An Introduction to Chaotic Dynamical Systems*, Addison-Wesley, 1989.

[DFVLR] DFVLR/B07: *Supplement, MEDYNA/WRSIM - Wheel-Rail Simulation*, DLR, Munich.

[Eickhoff, 1993] B. Eickhoff, G. Scott, R. Troup, P. Annable, T. Pearce, J. Evans and A. Minnis: *Vehicle Dynamics Training Cource, Part 1,2,3*. BR Research, 1993.

[Esveld, 1989] C. Esveld: *Modern Railway Track*, MRT-Productions, Duisburg 66, West Germany, 1989.

[Esveld, 1992] C. Esveld: MINIPROF - wheel and rail profile measuring system, *Rail Engineering International*

4, 1992, 6-9.

[Garg, 1986] V.K. Garg and R.V. Dukkipati: *Dynamics of Railway Vehicle Systems*, Benjamin Cummings, Menlo Park, 1986.

[Gimémez, 1991] J.G. Giménez, L.M. Martin, J.P. Pascal and J.L. Maupu: IAVSD railway benchmark≠2- SIDIVE and VOCO codes solutions, *Proc of 12th IAVSD-Symposium*, Lyon, August 1991, 172-184.

[Grassie, 1992] S.L. Grassie: Dynamic models of the track and their uses, *FRA/ERRI Conference*, Delft, June 1992.

[Guckenheimer, 1983] J. Guckenheimer and P. Holmes: *Nonlinear Oscillations, Dynamical Systems, and Bifurcations of Vectors Fields*, Springer Verlag, New York, 1983.

[Hammarlund, 1994] S. Hammarlund, A. Jahlenius and T. Dahlberg: Goose hill measurements confirm X2000's low dynamic track forces, *Railway Gazette International*, July 1994, 439-444.

[Jaschinski, 1990] A. Jaschinski: *On the Application of similarity laws to a scaled railway bogie model*, Ph.D. Thesis, Technical University Delft, 1990.

[Jensen, 1994] J.C. Jensen and E. Slivsgaard: Modelling of railway vehicle using elastic contact and moveable track, *Proc. Workshop on Railway Dynamics*, University of Rostock, May, 1994.

[Jensen, 1995] J.C. Jensen: *Teoretiske og eksperimentelle dynamiske undersøgelser af jernbanekøretøjer*, Ph. D. Thesis, Technical University of Denmark, IMM-PHD 1995-9, Lyngby, 1995 (in Danish).

[Jønsson, 1994] J. Jønsson, E. Svensson and J.T. Christensen: Strain gauge measuring of wheel-rail interaction forces, ES-Consult and DSB Consult, Denmark.

[Kaas-Petersen, 1986] C. Kaas-Petersen: Chaos in a railway bogie, *Acta Mechanica* **61**, 1986, 91-107.

[Kaas-Petersen, 1989] C. Kaas-Petersen: *PATH User's Guide*, Department of Mathematical Studies and Centre for Nonlinear Studies, University of Leeds, 1989.

[Kalker, 1990] J.J. Kalker: *Three-Dimensional Elastic Bodies in Rolling Contact*, Kluwer Academic Publishers, Dordrecht, 1990.

[Kerr, 1987] A.D. Kerr: On the vertical modulus in the standard railway track analysis, *Rail International*, November 1987, 37-44.

[Kik] W. Kik: *RSGEO,RSPROF - Programme zur simulation der Radsatz/Gleis oder Radsatz/Rollen kinematik*, Institut für Luft- und Raumfahrt, TU Berlin (in German).

[Knothe, 1993] K. Knothe and S.L. Grassie: Modelling of railway track and vehicle/track interaction at high frequencies, *Vehicle System Dynamics* **22**, 1993, 209-262.

[Knudsen, 1994] C. Knudsen, E. Slivsgaard, M. Rose, H. True and R. Feldberg: Dynamics of a model of a railway wheelset, *Nonlinear Dynamics* **6**, 1994, 215-236.

[Li, 1975] T.Y. Li and J.A. Yorke: Period three implies chaos, *American Mathematical Monthly* **82**, 1975, 985-992.

[Matsumoto, 1987] T. Matsumoto, L.O. Chua and R. Tokunaga: Chaos

via torus breakdown, *IEEE Transactions on Circuits and Systems* **34** no. 3, 1987, 240-253.

[Meijaard, 1989] J.P. Meijaard and A.D. De Pater: Railway vehicle systems dynamics and chaotic vibrations, *Int. Journal Non-Linear Mechanics* **24**, 1989, 1-17.

[Måleteknik, M007/94] Måleteknik: *Måleteknisk gennemgang af måledræsine, Matissa MPV8 litra MD 584*. Internal DSB report, 1994 (in Danish).

[Nielsen, 1993] J.C.O. Nielsen: *Train/Track Interaction*, Doctor thesis, Division of Solid Mechanics, Chalmers Tekniska Högskola, Sweden, 1993.

[Ostermeyer] G.P. Ostermeyer: On the influence of elastic rails on the hunting motion of bogies, *Polish - German Workshop on Dynamical Problems in Mechanical Systems*.

[Parker, 1989] T.S. Parker and L.O. Chua: *Practical Numerical Algoritms for Chaotic Systems*, Springer Verlag, New York, 1989.

[Pascal, 1991] J.P. Pascal and G. Sauvage: New method for reducing the multicontact wheel/rail problem to one equivalent rigid contact patch, *Proc of 12th IAVSD-Symposium*, Lyon, August 1991, 475-489.

[Pascal, 1994] J.P. Pascal: Oscillations and chaotic behaviour of unstable railway wagons over large distances, 1994, to appear in *Chaos, Solitons and Fractals*.

[Press, 1992] W.H. Press, S.A. Teukolsky, W.T. Vetterling and B.P. Flannery: *Numerical Recipes in FORTRAN*, Cambridge University Press, 1992.

[Prud'homme, 1967] A. Prud'homme: Der Wiederstand des Gleises gegen die von den Fahrzeugen ausgehende seitliche Beanspruchung, *Monatsschrift der Internationalen Eisenbahn-Kongressvereinigung* **44**, nr 8/9, 1967, 297-303.

[Ripke, 1991] B. Ripke and K. Knothe: *Die unendlich lange Schiene auf diskreten Schwellen bei harmonischer Einzellasterregung*, Fortschritt-Berichte VDI, Dusseldorf, 1991 (in German).

[Rose, 1994] R.D. Rose: Die entwicklung und erprobung kurvengesteuerter Einzelradsatz-Fahrwerk "KERF", *Glasers Annalen* **118**, nr 6 juni, 1994, 297-304 (in German).

[Sauvage, 1990] G. Sauvage and J.P. Pascal: Solution of the multiple wheel and rail contact dynamic problem, *Vehicle System Dynamics* **19**, 1990, 257-272.

[Shen, 1983] Z.Y. Shen, J.K. Hedrick and J.A. Elkins: A comparison of alternative creep force models for rail vehicle dynamics analysis, *Proc. of 8th IAVSD-Symposion*, Cambridge, August, 1983, 591-605.

[SIDIVE] *SIDIVE, Manual del usuario*, Contrucciones y Auxiliar de Ferrocarriles, CAF, Spain 1994 (in Spanish).

[Slivsgaard, 1992] E. Slivsgaard: *Bifurkationer og kaos i en ikke-lineær model af et enkelt jernbanehjulsæt*, Master's Thesis, Technical University of Denmark, 1992 (in Danish).

[Slivsgaard, 1993] E. Slivsgaard and C. Knudsen: Chaos in a model of a railway wheelset, in *Future Directions of Nonlinear Dynamics in Physical and Biological Systems*,

Proc. NATO ARW 1992, P.L. Christiansen, J.C. Eilbeck, and P.D. Parmentier (eds.), Plenum 1993, 165-169.

[Slivsgaard, 1994a] E. Slivsgaard and H. True: Chaos in railway vehicle dynamics, *Nonlinearity and Chaos in Engineering Dynamics*, J.M.T. Thompson and S.R. Bishop (eds.), Wiley 1994, 183-192.

[Slivsgaard, 1994b] E. Slivsgaard and J.C. Jensen: On the dynamics of a railway vehicle with a single-axle bogie, *Proc of 4th Mini Conference on Vehicle System Dynamics, Identification and Anomalies*, Budapest, November 1994.

[Smith, 1992] L.A. Smith: Nonlinear signal processing, Tutorial notes for *Mathematics in Signal Processing* from the University of Warwick, 1992.

[Takens, 1981] F. Takens: Detecting strange attractors in turbulence, in *Lecture Notes Mathematics* **898**, D.A. Rand and L.S. Young (eds.), Springer Verlag Berlin, 1981, 366.

[Tanifuji, 1995] K. Tanifuji: Chaotic Oscillation of a wheelset rolling on rail: Verification on roller rig, to appear in *Proc. of 14th IAVSD-Symposion*, Ann Arbor, August 1995.

[Thomson, 1995] D.J. Thompson and N. Vincent: Track dynamic behaviour at high frequencies. Part 1: Theoretical Models and Laboratory Measurements, *Vehicle System Dynamics Supplement* **24**, 1995, 86-99.

[True, 1992] H. True and J.C. Jensen: Chaos and asymmetry in railway vehicle dynamics, *Proc. 2. International Conference on Railway Bogies*, Budapest, Septem-

ber, 1992.

[True, 1993] H. True: Dynamics of a rolling wheelset, *Appl. Mech. Rev.* **46**, 1993, 438-444.

[Vermeulen, 1964] P.J. Vermeulen and K.L. Johnson: Contact of nonspherical bodies transmitting tangential forces, *Journal of Applied Mechanics* **34**, 1964, 338-340.

[Wickens,1965a] A.H. Wickens: The dynamic stability of railway vehicle wheelsets and bogies having profiled wheels, *Int J. Solids Structures* **1**, 1965, 319-341.

[Wickens,1965b] A.H. Wickens: The dynamic stability of a simplified four-wheeled railway vehicle having profiled wheels, *Int J. Solids Structures* **1**, 1965, 385-406.

[Wiggins, 1988] S. Wiggins: *Global Bifurcations and Chaos*, Springer Verlag, New York, 1988.

[Wolf, 1985] A. Wolf, J.B. Swift, H. Swinney and J.A. Vastano: Determining Lyapunov exponents from a time series, *Physica D* **16**, 1985, 285-317.

[Wrang, 1995] M. Wrang: *Single-axle running-gear (SARG)*, Ph.D. Thesis, Royal Institute of Technology, Stockholm, 1995.

[Zarembski, 1994] A.M. Zarembski: Track transitions: The effect of changes in track stiffness, *Railway Track & Structures*, June 1994, 9-10.

[Zhai, 1993] W. Zhai and X. Sun: A detailed model for investigating vertical interaction between railway vehicle and track, *Proc. of 13th IAVSD-Symposion*, Cengdu, August 1993, 603-615.